
Università degli Studi di Udine

Facoltà di Ingegneria

Laurea Specialistica in

Ingegneria Meccanica

Dipartimento di Energetica e Macchine


Tesi di Laurea

# Numerical analysis of phase-separating polymer blends with the Phase Field Model

**Analisi numerica della separazione di fase in miscele di polimeri mediante Modello di Fase**


Relatori:

Prof. Alfredo Soldati

Dott.ssa Dafne Molin

Candidato:

Luca Scarbolo



Anno Accademico 2008/2009

"*Bisogna rendere ogni cosa il più semplice possibile, ma non più semplice di ciò che sia possibile*"

A. Einstein

*Fine. ho scelto questa parola perchè descrive completamente lo stato d'animo che mi attraversa in questi ultimi giorni da tesista. Giunto quindi al capolinea di questa mia piccola avventura, desidero ringraziare tutte le persone che in qualche maniera mi sono state vicine e, volontariamente o meno, mi hanno aiutato a tagliare questo traguardo. Voglio innanzitutto ringraziare Serena, la persona che da quasi tre anni è al mio fianco, per aver sopportato le mie paturnie ed il mio ben noto caratteraccio, ma sopprattutto per essermi stata vicina nei momenti più difficili, quando veramente nulla era scontato. Ringrazio il Sime, Gombo, Vise, Gianni, Luca, Lucio, Enrico e Loris per tuti i bei momenti passati assieme in questi anni di università, un ulteriore abbraccio va a Loris, che mi ha sopportato nello svolgimento di questa tesi e senza il quale starei ancora lottando con le subroutine. Un grosso riconoscimento va a Dafne per essere riuscita a non essere convincente nello sconsigliarci questo progetto, ma sopprattutto per averci tratto d'impiccio molteplici volte ed averci letteralmente consentito di laurearci; ringrazio inoltre il Prof. Soldati e tutte le persone che lavorano nel suo gruppo di ricerca. Un grosso grazie va ai miei genitori, per avermi insegnato a tener duro anche di fronte alle difficoltà e per avermi permesso di compiere tutte le mie scelte in maniera indipendente e secondo la mia sola volontà, senza mai farmi pesare nulla. Infine un pensiero va al mio "fratellino" (al è un toc di lui..) Matteo, per la sua comprensione e disponibilità, augurandogli, quali che siano le sue decisioni, di ottenere altrettante soddisfazioni nei prossimi anni.*

*Udine, 23 Febbraio 2010*

# Contents

# List of Figures

# List of Tables

# Sommario

Lo scopo della presente tesi è la simulazione numerica della separazione di fase in miscele di polimeri, mediante l'implementazione di un Modello di Fase (PFM) su di un codice per la Simulazione Numerica Diretta (DNS) dei campi di moto fluido. L'approccio PFM consente l'analisi dell'evoluzione temporale della morfologia di sistemi multi-fase complessi, senza la necessitàdi introdurre modelli di tracciamento dell'interfaccia tipici dei Modelli classici di Gibbs. Il concetto di base dell'approccio PFM è quello di assumere un'interfaccia con spessore non nullo per l'interfaccia tra i vari componenti del sistema; in questo modo le leggi della termodinamica dei sistemi in condizioni di non equilibrio possono venir estese all'interfaccia stessa, ottenendo un evoluzione di quest'ultima guidata dai soli potenziali termodinamici. Nel presente lavoro è riportata l'implementazione numerica dell'equazione di Cahn-Hilliard (CH) assieme ai benchmarks effettuati per validare il codice. In questa analisi una forte riduzione dell'accuratezza dei risultati è stata notata lungo la direzione ortogonale alle pareti del canale; quindi si è preferito procedere con la validazione del codice semplificando la geometria del modello, trascurando la direzione normale alle pareti ed ottenendo così un modello bi-dimesionale. Sono state effettuate delle simulazioni bi-dimensionali di decomposizione spinoidale e di separazione di fase sotto Shear Flow al variare dei parametri caratteristici. Poichè i modelli PFM devono rappresentare delle interfacce a spessore non nullo, questi necessitano di elevate risoluzioni spaziali per poter valutare in maniera appropriata le dinamiche all'interfaccia. Sono quindi state effettuate una serie di simulazioni variando la spaziatura della griglia. Inoltre è stata provata la capacitàdel codice nel rappresentare correttamente l'interfaccia con al minimo tre punti griglia ed è stata provata anche l'accuratezza delle strutture morfologiche ottenute dalle simulazioni mediante

confronto con i dati disponibili in letteratura.

# Abstract

The purpose of this project is the numerical simulation of the phase separation of polymer blends, in a channel domain, with the Phase Field Model (PFM) implemented in an already existing Direct Numerical Simulation (DNS) code. The PFM approach allows to investigate the evolution in time of a complex multiphase systems morphology, without the introduction of the tracking methods that characterize the more classical approach, known as the Sharp Interface Approach. The basic idea underpinning the Phase Field Model, is the definition of a non-zero interface between the components of the system, in this way the non-equilibrium thermodynamic laws can be extended on to the interface region, obtaining a model where the interface dynamics is driven by the thermodynamical potentials. Through the present work the implementation of the Cahn-Hilliard (CH) equation is shown and the benchmarks used to validate the code are reported. Due to the high stiffness of the CH equation, the solution shown a detriment of accuracy along the wall-normal direction of the domain, thus the geometry has been simplified in to a bi-dimensional model, neglecting the wall-normal direction. The two-dimensional spinoidal decomposition has been simulated varying the characteristics parameters and also a phase separation under shear flow has been simulated. Because of the non-zero thickness of the interface, the PFM model needs high resolution to compute properly the interface dynamics, thus the simulations have been performed for different grid spacing. The capability of the algorithm to resolves the interface with at least three grid-points thickness has been proven and also the accuracy of the structures obtained from the simulations show a good agreement with the results available in literature.

# Chapter 1

# Introduction

> "*The important thing in science is not so much to obtain new facts as to discover new ways of thinking about them*"
>
> Sir W. Bragg

## 1.1 Motivations

Many engineering processes involve flows where different fluids and other substances are forced to share the same domain and hence to interact one with each others. These components usually show different physical properties, such as density, viscosity or chemical reactivity, thus their interactions are very complex and the prediction of the system behavior is non-trivial. Each component, divided from the others by a defined boundary and characterized by its own physical properties is called *phase*; whereas the surface between the two phases is called *interface*. Because of these definitions, the systems above are called *multi-phase systems* and they are object of study since the beginning of the last century (the first works, due to Young, Gauss and Laplace are dated 1805). Examples of these systems can be easily founded in many aspects of the every-day life. From the sand transported by the sea, where one of the two components is solid and the interface is represented by a discontinuity between the sand and the water, to a steam bubble rising in a pod of boiling water, where the two components, water and vapor, are divided by an interface which allows to distin-

guish the the bubbles. Now let consider a piece of ice melting in a glass of water, or a teaspoon of sugar solving in to a cup of coffee; they are still examples of two-phase system but in these cases the interface between the two components changes in time because of the melting and solving processes. Hence, if these two systems have to be studied in depth[1], also the dynamic of the interface has to be kept in account. Even if apparently there are no practical motivations to study how the sugar grains solve in to the coffee, the interface dynamics is an argument of paramount importance in many fields like in the material science and in biomedical applications, in chemical engineering and in environmental science. The study of the systems where the interface between the phases is not steady can be approached basically from two points of view: considering the interface as a sharp discontinuity and fitting its behavior with *tracking-model* obtained from various analysis, or considering the interface with non-zero thickness. The former approach is the so-called *sharp interface approach* and it forces the interface dynamics to follow a predictive model. The latter approach considers a non zero-thickness interface, where the properties of one phase change smoothly in to the properties of the other phase. Since the interface is "diffuse", this approach is known as the *diffuse interface approach*, and it is the object of the present work. Stating that the interface has a non-zero thickness, is possible to define the interfacial thermodynamical properties and potentials, thus the interface dynamics can be described using variational principles, avoiding the introduction of empirical tracking methods. Following the diffuse interface approach is possible to analyze processes where the interface evolution in time has an fundamental role, as the phase growing or the phase decomposition in the polymer blends [18] (two examples of polymer blends are reported in Figure 1.1). As shown by Anderson [2] the knowledge of the interactions between the polymer liquid phases, usually coupled with a flow field, permits to predict the micro-structures growing and then to characterize the material properties in relation to the flow and to the polymers physical parameters.

Also the dynamics of biological structures, as bio-membranes or cellular tumors, can be described by the application of the diffuse interface model. The

[1] If a macroscopical analysis is taken, the knowledge of the interface dynamics is not important.

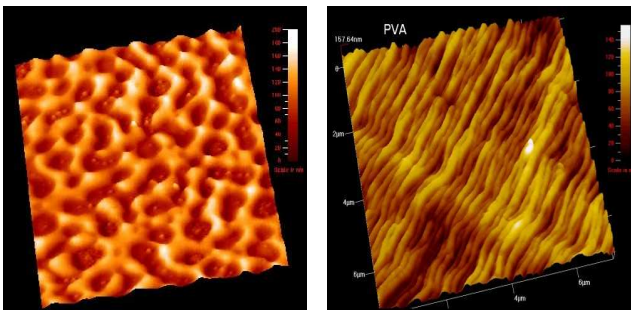


Figure 1.1: Polymer blend composed by a mixture of polystirene-polybutadine during the phase separation (left). Ppolyvinilacetate blend with orientate structure (right). Figures taken from *www.quesant.com*

former structures are high flexible interfaces which divide an internal biochemical environment from the surrounding fluid, creating little vesicles which have an active role in almost every process known in the human physiology [25]. For example they are involved in to the neuronal signal transport, in fact when they brake-up the internal fluid is leaved to flow out and to active the synapsis; thus understanding how the morphology of the vesicles depends on the fluid regimes and on the biological parameters, allow to predict their biological function. The vesicles formation and their morphological evolution in the proximity of the synapses are shown in Figure 1.2.

The application of the Diffuse Interface Model to the tumor growth, due to Wise *et al.*[37], is obtained defining some empirical based constitutive laws for the tissues which depend on several biological parameters, as the cell-cell and the cell-matrix adhesion and the nutritive fluxes. Introducing the constitutive laws in to the Diffuse Interface (DI) model, is possible to understand when the morphology of the cancer is unstable, allowing the cell proliferation and the tumor growth. Recently the biomedical application of the DI model has been investigate on a large number of works which are available in literature, for example the model has been applied by Saylor *et al.*[32] to analyze the drug releasing control into the human body. The Diffuse Interface models have been applied also to the development of industrial processes involving drops, such as

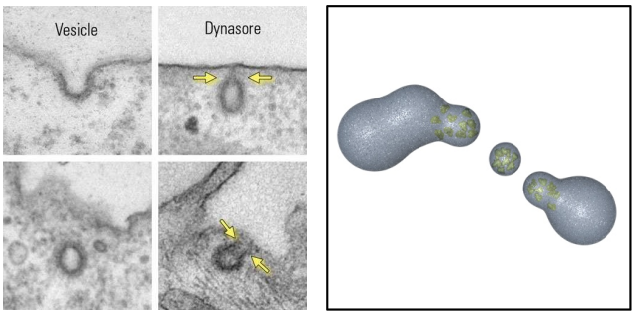


Figure 1.2: On the left the vesicle separation phases; on the right the vesicle creation. Figures taken from *http://labworks.hms.harvard.edu* (left) and *http://learn.genetics.utah.edu* (right)

the ink-jet technology, the spray coating and the spray cooling [19]. In this case the drop formation, its movement and finally its impact on to the solid wall can be studied in order to improve the efficiency of the devices and to reduce the environmental impact of such devices as well. The mixing processes is another class of problems which have been investigate using the DI models, examples can be founded in Lamorgese *et al.*[24] and Khatavkar *et al.*[20]. The former studied the mixing of a quiescent mixture which is instantaneously brought from the two to one-phase region of its phase diagram; whereas the latter studied the mixing of two immiscible fluids in a lid driven cavity flow. The DI model have also been introduced by Jancskar *et al.*[16], to understand the transition phase processes involved in film condensation which is widely involved in heat exchangers, condensation tubes, in the cooling of electronic devices and nuclear power plants or also in to the cavitation processes.

## 1.2 Thesis outline

Scope of the present work is the implementation of the Diffuse Interface model of two-phase fluid systems on a channel geometry, combining it with an already existing DNS (Direct Numerical Simulation) code. The targets of the work are the simulation of the phase separation of the polymer blends, coupled and de-

coupled with the flow-field and at different conditions. This thesis is organized in six chapters; in this first section the thermodynamical bases of the model are reported, whereas in the Chapter 2 the phase field and flow field governing equations are reported and in Chapter 3 the numerical scheme is shown. The Chapter 4 reports briefly the debugging work performed in order to benchmark the code, whereas in Chapter 5 the obtained results are shown. Finally in Chapter 6 the conclusions and some suggestions for further work are reported.

## 1.3 Literature survey

At the begin of the 19th century Young, Laplace and Gauss started to develop the theory of multi-phase systems assuming a zero-thickness interface between the different phases; in this way the physical properties of each phase may change in a discontinues way across the interface. This approach, known nowadays as the "sharp interface approach", was chosen because its simplicity, in fact it can be immediately derived applying the conservation principles on every phase of the system, yielding to a partial differential equations (PDE) system (for example the well-known Young-Laplace equation). The solution of the PDE's obtained from the mass, momentum and energy conservation, needs a set of boundary conditions, which have to be imposed also on to the boundary between the different phases, thus on to the interface. The classical boundary conditions at the interface, imposes the jump of the stress tensor equal to the product of the curvature and the surface tension and a zero velocity variation across the interface (Davis [11]). These conditions are following reported:

$$\Delta\tau|_{-}^{+} \cdot \mathbf{n} = k\sigma\mathbf{n}, \qquad \Delta\mathbf{u}|_{-}^{+} = 0. \tag{1.1}$$

Where $\mathbf{n}$ is the normal at the interface, $k$ is the interface curvature, $\tau$ is the gradient of the stress tensor across the interface and $\sigma$ is the surface tension. The model obtained is a free boundary problem [28], in fact no constraints have been introduced on the interface location, thus some tracking methods have to be coupled with the equations 1.1 to obtain the problem closure. Later the work of Young, Gauss and Laplace was generalized to the multi-phase thermodynamics and transport phenomena, introducing the interface thermodynamical

properties, as the surface energy and the surface entropy and the surface transport quantities, such as viscosity and heat conductivity. During all the 19th century almost all the multi-phase models were based on the sharp interface approach; only at the end of the '800 Rayleigh [31] and Van der Waals [35] (respectively 1892 and 1893)introduced the concept of non-zero interface between the phases. In his article Van der Waals used his equation of state to predict the interface thickness[2], showing that it becomes infinitely large when the critical point is reached. During 1901 Kortweg [22] proposed an expression for the capillary stresses, which are in general referred to as Kortweg stresses, in order to describe the forces acting on the different fluid-phases when they are driven in a non-equilibrium condition. Although the basic idea of the diffuse interfacd was introduced at the end of the 19th century, it was ignored by the scientific community until the middle of the '900. In 1958 Cahn and Hilliard [7] used this approach to describe the phase nucleation and the spinoidal decomposition and then it was used to describe the morphology of the polymer blends and metal alloys (see de Gennes [12]). The coupling of the DI model with the hydrodynamics equations was introduced by Kawasaky [17], Siggia [33] and Hohemberg [15] during the '70 referring to the "model H" and only later the name "Diffuse Interface Model" was introduced. From the end of the '70 to nowadays the rapid increase of the computing techniques has created the necessary conditions for the developing of the method, which needs high computational resources and efficient numerical schemes, because of the high resolution needed and high stiffness of the PDE's involved; thus several examples of applications can be founded in literature. The most important goal of the diffuse interface model, is the capability to investigate problems where the sharp interface model fails, in fact when the problems under analysis are of the same length scale of the interface, the classical models breaks down, even with the use of advanced tracking techniques. Some examples can be founded in the partially miscible mixtures, when the interface diverges up to the critical point, in the problems which involve liquid drops coalescence/breakup or all the class of problems where phase transition is introduced. In addition, because of the free boundary nature of the problem, the intersection of the interfaces is difficult to track and the sharp

[2]The Van der Waals approach is partially reported in Section 1.4

discontinuity between the phases can create some numerical troubles. Introducing the DI model these problems can be easily solved, because the interface dynamics is thermodynamically driven, and not governed by a stochastic tracking model. One of the most important characteristics of the DI model is the introduction of a phase field variable $\phi$; which is a continuous function which depends on the position vector $\mathbf{x}$ and time $t$ and it varies in a rapid but continuous fashion across the interfacial region, whereas it varies smoothly in the bulk phase regions. The order parameter is usually coincides with the phase density $\rho$ for single components systems, whereas it describes the molar or mass fraction of the components in the liquid mixtures. In general it does not need to be related with a physical variable, in fact the DI model can be obtained also from a pure mathematical approach [13]. Because of the introduction of the order parameter, the diffuse interface models are collected in the most general class of the *phase field models*, which give the title to this work.

## 1.4 Thermodynamics of single component system

The diffuse interface approach, as reported in the previous section, allows to describe the morphological evolution of a non equilibrium system without the use of tracking methods to define the interface position. To achieve this target, first of all the equilibrium thermodynamics of the system has to be studied, in order to define how the system can be characterized by macroscopic state variables and diagrams. The first step to derive the thermodynamical formulation of the diffuse interface model for a single component system is the definition of Helmholtz free energy which depends on the molecular forces acting on the system. For fluids in which the ideal gasses hypotheses do not hold, the intramolecular forces are a combination of strong and weak interactions. The formers are responsible to hold together protons and neutrons of the fluid atoms, whereas the latter act between two molecules resulting in a long-range interaction. Because the strong forces act between the particles of the same atomical nucleus, they do not exsert appreciably actions on to the surrounding fluid molecules, thus only the weak forces have to be kept in account for the free energy definition. To approximate the discrete effect of every molecule with a continuous medium, the mean field

hypothesis is introduced. Under this assumptions, the free energy of a system with constant temperature $T$ and variable density $\rho$ is the following:

$$f\left(\rho(\mathbf{x})\right) = f_{id} + \frac{1}{2}RTN_A \int \left(1 - e^{-}U(r)/kT\right)\rho(\mathbf{x}+\mathbf{r})\mathrm{d}^3\mathbf{r} \tag{1.2}$$

where $\mathbf{x}$ is the position vector, $R$ is the gas constant, $N_A$ is the Avogadro number and $r$ is the Boltzmann's constant. $U(r)$ is the molecular pair interaction potential and depends on the modulus of the molecules distance $r = |\mathbf{r}|$ while the $1/2$ factor is introduced because the interacting molecules are counted twice. The first term on the RHS of the equation 1.2 represents the ideal part of the free energy, that is the energy associated to molecules that do not interact, whereas the second one is a molecular pair potential. The former is represented in the following way:

$$f_{id} = RT\ln\rho(\mathbf{x}) \tag{1.3}$$

The long-range intermolecular pair potential is a Lennard-Jones potential, described by a $r^{-6}$ decaying term, whereas the short-range interactions are represented by hard core repulsion term. Stating this, the following formulation is obtained:

$$U(r) = \begin{cases} -U_0(r/l)^6 & \text{if} \quad (r > d) \\ \infty & \text{if} \quad (r \leq d) \end{cases} \tag{1.4}$$

Where $U_0$ is the non dimensional pair potential strength, $l$ is the length scale of the intermolecular interactions and $d$ is the nominal hard core length. For a constant density system, the thermodynamical free energy $f_{Th}$ yields to:

$$f_{Th}(\rho, T) = f_{id}(\rho, T) + f_{ex}(\rho, T) \tag{1.5}$$

Following the procedure used to obtain equation 1.2, the thermodynamical free energy is computed as the sum of two terms: the ideal part and the so called excess part $f_{ex}$. The latter refers to the component of thermodynamical free energy due to the molecules interaction and thus represents the deviation from the ideal gasses model; keeping the density constant, the following expression is obtained:

$$f_{ex}(\rho, T) = RT\rho\mathcal{F}(T) \tag{1.6}$$

Where $\mathcal{F}(T)$ is the virial coefficient, defined as follows:

$$\mathcal{F}(T) = \frac{1}{2}N_A \int_0^\infty \left(1 - e^{-U(r)/kT}\right) 4\pi r^2 \mathrm{d}r \tag{1.7}$$

Substituting in equation 1.7 the Lennard-Jones pair potential 1.4, the integral solution gives:

$$\mathcal{F}(T) = 2\pi N_A \int_0^d r^2 \mathrm{d}r + 2\pi N_A \int_d^\infty \left(1 - e^- \frac{U_0}{kT}(l/r)^6\right) r^2 \mathrm{d}r = b - \frac{a}{RT} \tag{1.8}$$

Where the last two terms in the RHS of equation 1.8 are:

$$b = \frac{2}{3}\pi \mathrm{d}^3 N_a, \qquad a = \frac{2}{3}\pi U_0 N_A^2 \frac{l^6}{d^3}. \tag{1.9}$$

They represent respectively the non-zero molecular volume effect via the hard-core repulsion, and the long-range interaction due to the molecular pair potential. Finally the thermodynamical free energy is rewritten in the following way:

$$f_{Th} = f_{id} + RTb\rho - a\rho \approx RT\ln\left(\frac{\rho}{1 - b\rho}\right) - a\rho \tag{1.10}$$

Substituting the specific volume $v = \rho^{-1}$ in to the equation above, it reads:

$$f_{Th} = RT\ln\left(\frac{1}{v - b}\right) - \frac{a}{v} \tag{1.11}$$

A way to describe the pressure terms of the thermodynamical free energy is obtained using the procedure purposed by Fermi [14]. Lets consider a reversible and infinitesimal isothermal transformation, where the system reaches an infinitesimal variation $\mathrm{d}v$ of its volume; the variation of the free energy, with respect to the volume variation, is described by the following:

$$\delta f_{Th} = \left(\frac{\partial f_{Th}}{\partial v}\right)_T \mathrm{d}v \tag{1.12}$$

Since the work of a reversible system is equal to the reduction of its free energy, the equation 1.12 yields to:

$$p\mathrm{d}v = -\left(\frac{\partial f_{Th}}{\partial v}\right)_T \mathrm{d}v \tag{1.13}$$

Where $p\mathrm{d}v$ is equal to the thermodynamical work, thus the following equality is obtained:

$$p = -\left(\frac{\partial f_{Th}}{\partial v}\right)_T \tag{1.14}$$

Substituting equation 1.14, in to the Van der Waals' equation, the non ideal gasses equation for a single component system is obtained:

$$\left(p + \frac{a}{v^2}\right)(v - b) = RT \tag{1.15}$$

The $a$ and $b$ constants, described by equations 1.9, are characteristics of the system component; when $a$ and $b = 0$, Van der Waals' equation reduces to ideal gasses equation $pv = RT$. From equation 1.15 is easy to understand the physical meaning of the two quantities $b$ and $a/v^2$; in fact the former represent a correction on the specific volume of the substance which keeps in account the non-zero volume of the molecules. The latter is a pressure correction term due to the long-range interactions between the molecules.

### 1.4.1 Critical point

Almost every kind of single component system can be described by means of equilibrium thermodynamical diagrams, where the properties of the substance are related to the the governing variables. The common point of this kind of representation is the equilibrium condition, which is mathematically described by a minimum in the thermodynamical potential (as the free energy described in the previous section). For a single component system, one of the most common thermodynamical planes is the pressure-temperature diagram (or $p - T$ diagram), which is divided in three zones, one fore each state of the substance: solid, liquid and vapor. This zones are separated by three curves which represents the combination of pressure and temperature necessary for the phase coexistence. The three phases coexisting state is described by an unique combination of pressure and temperature (in accordance with the Gibbs' phase rule) and it is called triple point. The curve which separates liquid and vapor zones

is the locus of all the diagram points where vapor and liquid coexist; it starts from the triple point and stops at the critical point, characterized by the critical pressure $p_c$ and the critical temperature $T_c$.

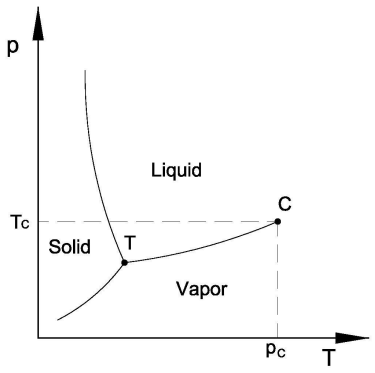


Figure 1.3: Pressure-temperature diagram ($p$-$T$) for a single component system

If temperature is higher than the critical temperature $T > T_c$ and pressure is lower than the critical pressure $p < p_c$ the differences between vapor and liquid vanish and the two phase coexistence cannot be reached. Furthermore moving along the vapor liquid curve from the triple point to the critical point, the difference of specific volume between the two phases reduces until it vanishes when the point is reached. According to this, the specific volume of the two phases near the critical point, with fixed temperature $T \to T_C$, can be represented in this way:

$$v_L = v, \qquad v_V = v + \delta v. \tag{1.16}$$

Where the suffix $L$ and $V$ refers respectively to the liquid and vapor phases, and $\delta v$ is an howbeit little difference of specific volume between the two phases. The Gibbs' phase rule assures that in a $n$ component system with $f$ coexisting phases, the number of degrees of freedom are $v = 2 + n - f$; thus, because of the fixed temperature and the coexistence of two phases, the pressure must be the same.

$$\begin{aligned} p_L(T,v) &= p_V(T,v+\delta v) \\ &= p(T,v) + \left(\frac{\partial p}{\partial v}\right)_T \delta v + \frac{1}{2}\left(\frac{\partial^2 p}{\partial v^2}\right)_T (\delta v)^2 + ... \end{aligned} \tag{1.17}$$

Where the specific volume of the liquid phase has been expanded in Taylor's series. Dividing all the terms by $v$ and letting $\delta v \to 0$ the equation 1.18 yields to the following condition at the critical point:

$$\left(\frac{\partial p}{\partial v}\right)_T = 0 \tag{1.18}$$

A system near an equilibrium condition can be described in in this way:

$$\delta f_{Th} + p\delta v \geq 0 \tag{1.19}$$

Expanding $\delta v$ in Taylor's series keeping $T$ constant it yields to:

$$\begin{aligned} \delta f_{Th} + p\delta v &= p\delta v + \left(\frac{\partial f_{Th}}{\partial v}\right)_T \delta v + \frac{1}{2}\left(\frac{\partial^2 f_{Th}}{\partial v^2}\right)_T (\delta v)^2 + \\ &+ \frac{1}{3!}\left(\frac{\partial^3 f_{Th}}{\partial v^3}\right)_T (\delta v)^3 + \frac{1}{4!}\left(\frac{\partial^4 f_{Th}}{\partial v^4}\right)_T (\delta v)^4 + ... \end{aligned} \tag{1.20}$$

Introducing again the equality 1.14 and substituting equation 1.18 the following inequality is obtained:

$$\frac{1}{3!}\left(\frac{\partial^3 f_{Th}}{\partial v^3}\right)_T (\delta v)^3 + \frac{1}{4!}\left(\frac{\partial^4 f_{Th}}{\partial v^4}\right)_T (\delta v)^4 + ... \leq 0 \tag{1.21}$$

To obey to the virtual work principle, equation 1.21 must be valid for every arbitrary and albeit small value of $\delta v$, thus the following conditions, rewritten in terms of pressure variable, are reached:

$$\frac{1}{3!}\left(\frac{\partial^2 p}{\partial v^2}\right)_{T_C} = 0, \qquad \frac{1}{4!}\left(\frac{\partial^3 p}{\partial v^3}\right)_{T_C} < 0. \tag{1.22}$$

From equation 1.18 is evident that the critical point corresponds to an horizontal inflection of the curve on pressure-temperature diagram; therefore equations 1.18 and 1.22 yields to the following conditions on the thermodynamical free energy:

$$\left(\frac{\partial^2 f_{Th}}{\partial v^2}\right)_{T_C} = 0, \qquad \left(\frac{\partial^3 f_{Th}}{\partial v^3}\right)_{T_C} = 0. \tag{1.23}$$

The Van der Waals' equation constants, $a$ and $b$, can be determined imposing the horizontal inflection condition at the critical point on $p - v$ diagram. The results are obtained in terms of critical temperature $T_C$ and critical pressure $p_C$:

$$a = \frac{9}{8} R T_C v_C = \frac{27}{64} \frac{(RT_C)^2}{p_C}, \qquad b = \frac{1}{3} v_C = \frac{1}{8} \frac{(RT_C)}{p_C}. \tag{1.24}$$

And then, known the two constants of the Van der Waals equation, the critical parameters can be determined:

$$p_C = \frac{1}{27} \frac{a}{b^2}, \qquad T_C = \frac{8}{27} \frac{a}{Rb}, \qquad v_C = 3b. \tag{1.25}$$

The Van der Waals equation can be written in non dimensional form using the following reduced variables:

$$p_r = \frac{p}{p_C}, \qquad T_r = \frac{T}{T_C}, \qquad v_r = \frac{v}{v_C}. \tag{1.26}$$

Thus equation 1.15 rewritten in non dimensional form yields to:

$$\left(p_r + \frac{3}{v_r^2}\right)(3v_r - 1) = 8T_r \tag{1.27}$$

Equation 1.27 represents a family of isothermal curves on a $p_r - v_r$ plane; they describe the state of a single component system for every couple of reduced variables $p_r$ and $v_r$, fixed the reduced temperature $T_C$. As shown in equation 1.4 if $T_r \geq 1$ the isotherms are monotonically decreasing, whereas when $T_r < 1$ the isotherms show a maximum $d$ and a minimum point $e$. The region comprised between the maximum and the minimum point of the subcritical isotherm is a non stable region, where two phases are founded.

### 1.4.2 Coexistence and phase separation

As shown in the previous section, a single component system can be driven out of equilibrium obtaining a phase separation; if the state variables are properly chosen, the system reaches a new equilibrium condition which is governed only by one state variable (according to the Gibbs' phase rule). Following Comini

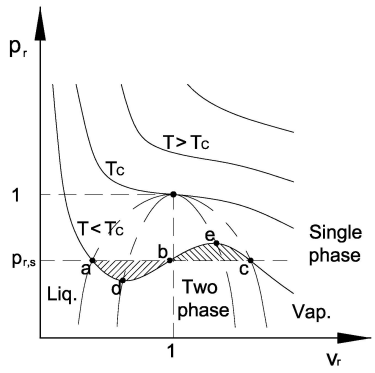


Figure 1.4: Isothermal curves on reduced pressure-volume diagram ($p_r$-$v_r$) for a single component system

[10], the Gibbs molar free energy for each phase $A$ and $B$, of a single component system, can be described as follows:

$$g_{Th}^{A} = f_{Th}^{A} + p^{A}v^{A}; \qquad g_{Th}^{B} = f_{Th}^{B} + p^{B}v^{B}. \tag{1.28}$$

Equation 1.28 can be rewritten in differential way, where the thermodynamical free energy is defined as the difference between the internal energy of the system $u$ and the product of the temperature and the system entropy $s$ [10]:

$$\begin{aligned} \mathrm{d}g_{Th} &= \mathrm{d}f_{Th} + v\mathrm{d}p + p\mathrm{d}v \\ &= \mathrm{d}u - T\mathrm{d}s - s\mathrm{d}T + v\mathrm{d}p + p\mathrm{d}v \\ &= -s\mathrm{d}T + v\mathrm{d}p \end{aligned} \tag{1.29}$$

Where the thermodynamical identity $\mathrm{d}u = T\mathrm{d}s - p\mathrm{d}v$ has been used. The saturation pressure of the two phase system $p_s$ at given temperature, that is the pressure where a vapor starts to generate liquid phase, can be obtained applying the equilibrium condition at the system where the two phases coexist. The equilibrium condition reads that the Gibbs free energy of each phase must be equal to the one of the other:

$$g_{Th}^{A} - g_{Th}^{B} = \int_{a}^{c} \mathrm{d}g_{Th} = 0 \rightarrow \int_{a}^{c} v\mathrm{d}p = \int_{a}^{c} v\left(\frac{\partial p}{\partial v}\right)_{T}\mathrm{d}v \tag{1.30}$$

Where $a$ and $c$ are the equilibrium or saturation points for the liquid and vapor phase respectively and $p = p(v)$ is an isotherm transformation; thus, since the temperature is fixed, the $sdT$ term has been canceled. The $p = p_s$ curve is crossed three times by the isothermal curve, respectively at $a$, $b$ and $c$ point, generating two area comprised between the $p_s$ curve and the isothermal curve. Stating this, is easy to find a geometrical meaning of the energy equality of equation 1.30, in fact the area between $a - b$ intersection points must be equal to the area between $b - c$ intersection points (shaded areas in Figure 1.4); this geometrical interpretation is also known as Maxwell's rule [14]. The thermodynamical free energy, in terms of reduced variables, can be derived starting from equation 1.11 an introducing the equalities of equation 1.24:

$$\frac{f_{Th}}{RT_C} = -T_r \ln(v_C) - T_r \left( v_r - \frac{1}{3} \right) - \frac{9}{8v_r} \tag{1.31}$$

For a fixed value of $T_r < 1$ the reduced free energy yields the curve reported in Figure 1.5. If the substance is at equilibrium and the two phases coexist, in accordance with the Gibbs' phase rule, the pressure of the two phases must be the same:

$$p^A = p^B \rightarrow \frac{\partial f_{Th}}{\partial v}^A_T = \frac{\partial f_{Th}}{\partial v}^B_T \tag{1.32}$$

As shown in Figure 1.5 the two equilibrium points lie on the same tangent tine of the $f_{Th} - v$ or $f_{Th,r} - v_r$ diagram.

The equilibrium value of $v_r^a$ and $v_r^c$ can be obtained in two different way: from equation 1.32 or minimizing the total free energy equation. In Figure 1.4 the locus of all the equilibrium points $a$ and $c$ have been represented with its classical bell shape; outside the curve all the states are stable and characterized by only one phase. For temperature $T_r < 1$ the stable liquid (outside the left branch of the bell) is commonly called undercooled liquid, whereas the stable vapor (outer the right branch of the bell) is called superheated vapor. Furthermore in Figure 1.4 have also been represented all the possible positions either of relative minimum $d$ and maximum $e$ of the under critical isotherms. It shows a bell shaped curve always contained in the equilibrium points bell. Inside the locus of $d$ and $e$ all the points are unstable and they will separate in two coexisting stable phases, whereas the area of the diagram comprised between

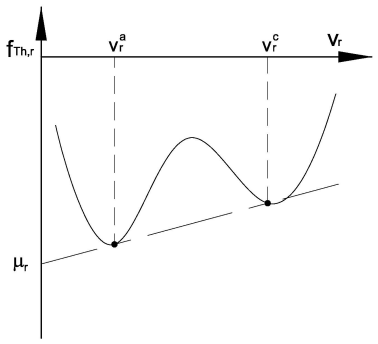


Figure 1.5: Typical shape of thermodynamical free energy on reduced energy-volume diagram ($f_{Th,r}$-$v_r$) for a single component system

the two bells represents all the metastable states. This states are in a nearly stable condition until their free energy remains the same; if a small perturbation is introduced, the system separates in two phases. The outer bell curve is the so called equilibrium curve, whereas the inner bell curve is the so called spinoidal curve; the latter can be determined using the following relation:

$$\left(\frac{\partial p}{\partial v}\right)_T = 0 \rightarrow \left(\frac{\partial^2 f_{Th}}{\partial v^2}\right)_T = 0 \tag{1.33}$$

### 1.4.3 Diffuse interface

In the previous sections the densities of the fluid phases $\rho^A$ and $\rho^B$ have been considered constant inside each phase and, when two phases coexist, the changing from the phase $A$ to the phase $B$ happen in a discontinuous way, according to the Sharp Interface theory. Another approach can be introduced considering the density of the system variable (non-constant) in every position of the domain; thus in the limit case of two coexisting phases, the density changes smoothly between the two limits $\rho^A$ to $\rho^B$, according to the diffuse interface approach. Following the diffuse interface approach the Helmholtz free energy $f(\mathbf{x})$ is rewritten in the following way:

$$f(\mathbf{x}) = f_{Th}(\mathbf{x}) + \Delta f_{NL}(\mathbf{x}) \tag{1.34}$$

Where $f_{Th}$ is the thermodynamical free energy as defined in equation 1.5 for a constant density system and an isothermal transformation and $\Delta f_{NL}(\mathbf{x})$ is a free energy contribution due to the diffuse interface approach.

$$\Delta f_{NL}(\mathbf{x}) = \frac{1}{2} N_A^2 \int_{r>d} U(r)[\rho(\mathbf{x}+\mathbf{r}) - \rho(\mathbf{x})]\mathrm{d}^3\mathbf{r} \tag{1.35}$$

The equation above keeps in account the non local free energy due to the density changes; the non local definition is used because the energy at any arbitrary point of the domain depends also from density of the neighboring points in the way described by the RHS of 1.35. Furthermore, since $\Delta f_{NL}$ keeps in account the effects of the diffuse interface, it tends to the interfacial energy in the limit of the existence of an interface between the two phases. As reported by Van der Waals in his work [35] the error committed considering the free energy as a local function, vanishes if at the equilibrium the system reaches an homogeneous condition. For this reason and assuming the isotropy hypothesis for the system [3], the density can be rewritten in the following way:

$$\rho(\mathbf{x}+\mathbf{r}) = \rho(\mathbf{x}) + \mathbf{r}\cdot\nabla\rho + \frac{1}{2}\mathbf{r}\cdot\mathbf{r}\cdot\nabla^2\rho + ... \tag{1.36}$$

The contribution of the linear term can be neglected and, considering only the leading orders, the local approximation of the non local free energy yields:

$$\Delta f_{NL}(\mathbf{x}) = -\frac{1}{2} RTK\nabla^2\rho(\mathbf{x}) \tag{1.37}$$

Where:

$$K = \frac{2\pi}{3}\frac{N_A U_0}{kT}\frac{l^6}{d} \tag{1.38}$$

The total free energy is calculated in the following way:

$$F = \int_V \rho f(\mathbf{x})\mathrm{d}V\mathrm{d}^3\mathbf{x} \tag{1.39}$$

Then, integrating by parts:

$$\int \rho(\mathbf{x})\nabla^2\rho(\mathbf{x})\mathrm{d}^3\mathbf{x} = -\int |\nabla\rho(\mathbf{x})|^2\mathrm{d}^3\mathbf{x} \tag{1.40}$$

[3] isotropic systems are characterized by uniform properties in every direction considered

Then the free energy per unit volume $\hat{f}$ is obtained:

$$\hat{f} = RT\left[\rho\tilde{f}_{Th}(\rho,T) + -\frac{1}{2}RTK\nabla^2\rho(\mathbf{x})\right] \tag{1.41}$$

Where $\tilde{f}_{Th} = f_{Th}/RT$. At the equilibrium the total free energy $F$, as shown in the previous section, is minimum; thus to calculate the equilibrium condition, $F$ has to be minimized with the constraint of constant number of molecules. The total free energy is minimized using the Lagrange multipliers [4], obtaining the following condition:

$$\delta\int(\rho f - RT\tilde{\mu}\rho)\,\mathrm{d}^3\mathbf{x} = 0 \tag{1.42}$$

Where $RT\tilde{\mu}$ is the Lagrange multiplier introduced for the minimization process

### 1.4.4 Generalized chemical potential

The Euler-Lagrange equation, corresponding to the minimization condition 1.42, leads to the following:

$$\tilde{\mu} = \frac{1}{RT}\frac{\delta(\rho\hat{f})}{\delta\rho} = \frac{\mathrm{d}(\rho\tilde{f}_{Th})}{\mathrm{d}\rho} - K\nabla^2\rho \tag{1.43}$$

By definition the Gibbs's free energy of a single component system, with uniform density coincides with the chemical potential $\tilde{\mu}_{Th}$:

$$\tilde{\mu}_{Th} = \frac{\mathrm{d}(\rho\tilde{f}_{Th})}{\mathrm{d}\rho} = \tilde{f}_{Th} + \frac{1}{v}\frac{\mathrm{d}(\tilde{f}_{Th})}{-\frac{1}{v^2}\mathrm{d}v} = \tilde{f}_{Th} + v\frac{\mathrm{d}(\tilde{f}_{Th})}{\mathrm{d}v} \tag{1.44}$$

The equation above represents the straight tangent line to both the minimum points of the free energy curve of Figure 1.5 even if the figure shows the $\mu_{Th,r} = \frac{T}{T_C}\tilde{\mu}_{Th}$ chemical potential in reduced variables. Equation 1.43 can be rewritten in the following way, substituting equation 1.44:

$$\tilde{\mu}(\rho,\nabla\rho) = \tilde{\mu}_{Th}(\rho) - K\nabla^2\rho \tag{1.45}$$

Equation 1.45 describes the generalized chemical potential in terms of the thermodynamical potential and the double gradient of the density of the fluid;

[4] An example of the application of the Lagrange multipliers principle is reported in Section 1.7

the thermodynamical chemical potential can be also determined from the diagram reported in Figure 1.5, in fact if $v = 0$ the equation 1.44 yields to $\tilde{\mu}_{Th} = \tilde{f}_{Th}$, hence it is represented by the intersection between the tangent line and the free energy axis. When two phases coexist at equilibrium, different zones of the domain are characterized by $\rho^A$ density, whereas the others zones show $\rho^B$ density; if the interface between phase $A$ and $B$ is planar and centered on $z = 0$ of the refereing frame, the equation 1.43 can be solved because the the equilibrium free energy is known. Imposing the density constant and equal to the equilibrium value in a region far from the interface zone, the generalized chemical potential in this zone is equal to its thermodynamical value. In the proximity of the critical point, the chemical potential vanishes and the free energy yields the following form:

$$\frac{\mathrm{d}^2\tilde{v}}{\mathrm{d}\tilde{z}^2} - 2a\tilde{t}\tilde{v} - 4\mathcal{F}\tilde{v}^3 = 0 \tag{1.46}$$

Where the dimensionless variables are:

$$\tilde{z} = \frac{z}{\xi}, \qquad \xi = \sqrt{\frac{K}{-v_C a\tilde{t}}}, \qquad \tilde{t} = T_r - 1, \qquad \tilde{v} = v_r - 1. \tag{1.47}$$

The equation 1.46 was solved first by Van der Waals, imposing the specific volume far from the interface equal to the equilibrium specific volume $\tilde{v}_e$.

$$\tilde{v}(\tilde{z} \to \infty) = \pm\tilde{v}_e = \pm\sqrt{\frac{-a\tilde{t}}{2\mathcal{F}}} \tag{1.48}$$

Finally the solution yields the following concentration profile:

$$\tilde{v}(\tilde{z}) = \tilde{v}_e \tanh \tilde{z} \tag{1.49}$$

Where $\xi$ represents the interface thickness, as reported in Figure 1.6.

### 1.4.5 Surface tension

As shown in Section 1.4.3, the total free energy for a single component system with non uniform density is composed of a thermodynamical and constant part and a non local contribution due to the density variations. Considering then a system where two phases coexist at equilibrium and are divided by a planar

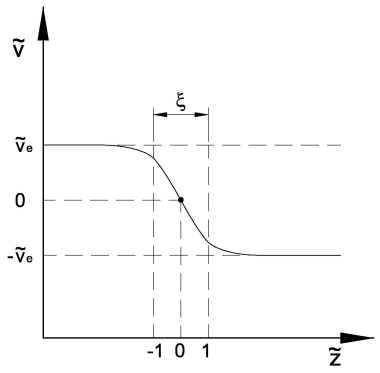


Figure 1.6: Analytical solution of the specific volume profile for a mono-dimensional single component system

interface, is possible to define the quantity of free energy $\sigma$ stored in the interfacial region. The energy stored in the interfacial volume corresponds to the interfacial tension, and can be calculated in the following way:

$$\sigma = -\frac{1}{2}RTK\int_{-\infty}^{\infty}\rho\frac{\mathrm{d}^2\rho}{\mathrm{d}\rho^2}\mathrm{d}z = \frac{1}{2}RTK\int_{-\infty}^{\infty}\left(\frac{\mathrm{d}\rho}{\mathrm{d}\rho}\right)^2\mathrm{d}z \tag{1.50}$$

Where the integral has been solved via parts rule and considering that outside the interfacial region the argument of the integral is null, because of the constant density. The detailed behavior of the surface tension was pointed out by Pismen *et al.*[29] who found that it decreases reaching the critical point.

## 1.5 Thermodynamics of binary systems

In the previous section the thermodynamics of a single component system have been analyzed in order to introduce the physics underpinning the diffuse interface model; in this section the thermodynamics of the binary mixtures will be introduced and focalized on the diffuse interface application, following almost the same procedure. The Van der Waals approach is thus extended to the simplified case of regular mixtures, that are binary solutions in which volume and entropy do not change during the mixing process, thus the mixing volume $v_{mix}$ and mixing entropy $s_{mix}$ are both equal to zero. Following the regular mixtures hypothesis, the system maintains its volume unaltered after a mixing process,

thus it can be considered incompressible; furthermore its entropy change due to the mixing process, is equal to that of an ideal mixture. The binary system is composed by two species, the first is called fluid 1 whereas the second specie is called fluid 2; this two fluids are mixed, thus every point of the domain is characterized by the concentration $c_1$ of the former fluid and the concentration $c_2$ of the latter fluid. To avoid the necessity of two parameters to describe the quantity of every component at each domain location, the order parameter $\phi$ havs been introduced; since the concentrations are usually defined to have unitary sum $c_1 + c_2 = 1$, they can be described in the following way by a unique variable:

$$\phi = c_1, \qquad (1 - \phi) = c_2. \tag{1.51}$$

The order parameter $\phi$ changes smoothly along the domain allowing to determine the concentration of the substances at each location of the domain itself.

### 1.5.1 Gibbs free energy

The Gibbs free energy is determined applying the procedure used in Section 1.4.2 to a binary mixture. Starting from the definition of Gibbs free energy $g_{Th} = f_{Th} + pv$ and applying it to an uniform mixture, the following equation is obtained:

$$g_{Th}(\phi) = g_{id}(\phi) + g_{ex}(\phi) \tag{1.52}$$

Where $g_{id}$ is the Gibbs free energy of an ideal mixture and the intermolecular potentials $U_{i,j}$ between the $i$ and $j$ molecules are the same; hence, for a pair molecules system, $U_{11} = U_{22} = U_{12}$. Furthermore for an ideal mixture the Gibbs free energy is equal to the free energy, thus, extending the free energy for a single component $f_{id} = RT\ln\rho$, the following relation is obtained:

$$\begin{aligned} g_{id} &= RT\left[c_1\ln(c_1\rho) + c_2\ln(c_2\rho)\right] \\ &= RT\ln\rho + RT\left[\phi\log\phi + (1-\phi)\log(1-\phi)\right] \end{aligned} \tag{1.53}$$

Where the mixture density is kept constant and the concentration of the species is variable. The $g_{ex}$ term of the RHS of equation 1.52 keeps in account the excess of Gibs free energy due to the non ideal part of the free energy and has a really convenient formulation for regular mixtures. The theory of regular mixtures was developed by Van Laar, who assumed that the two species composing the mixture have the same size and energy; he supposed also that the Van der Waals equation can be applied to the pure fluids and to the mixture as well. As reported in the previous section, the first result of these hypothesis is that regular mixtures have negligible entropy and volume excess, thus their volume and entropy is equal to those of an ideal gas mixture. Furthermore, since $s_{ex} = -(\partial g_{ex}/\partial T)_{P,c} = 0$, the excess of Gibbs free energy must be independent from the system temperature; therefore $v_{ex}$ and $s_{ex}$ are negligible and, remembering the definition of free energy, $g_{ex}$ is equal to excess of internal energy $u_{ex}$. Under these assumptions, it can be shown that the excess of Gibbs free energy for a regular mixture has the following form:

$$g_{ex} = c_1 \frac{a_1}{b} + c_2 \frac{a_2}{b} - \frac{a_{mix}}{b} \tag{1.54}$$

Where $a$ and $b$ represent the Van der Waals constants and the subscripts 1 and 2 refers respectively to the pure fluid 1 and the pure fluid 2 and, since the excess volume is similar for both the substances, $b_1 = b_2 = b_{mix}$. The $a_{mix}$ constant is described as follows:

$$a_{mix} = c_1^2 a_1 + c_2^2 a_2 + 2c_1 c_2 \sqrt{a_1 a_2} \tag{1.55}$$

Thus equation 1.54 yields to:

$$g_{ex} = \frac{1}{b} c_1 c_2 (a_1 + a_2 - 2\sqrt{a_1 a_2}) \tag{1.56}$$

The equation above remarks that the excess of free energy does not depend on the temperature $T$, thus $s_{ex} = 0$; similar considerations could be applied to the dependence of the free energy on the pressure, confirming the hypothesis of $v_{ex} = 0$. Considering than the Gibbs free energy definition, and applying it to the excess case, the following is obtained:

$$g_{ex} = f_{ex} + p v_{ex} \tag{1.57}$$

Applying equation 1.6 for a uniform density system and considering $v_{ex} =$, the equation above reads:

$$g_{ex} = f_{ex} = RT\rho\mathcal{F} \tag{1.58}$$

Where $\mathcal{F}$ is the virial coefficient and, for a binary mixture it shows the following formulation:

$$\mathcal{F} = c_1^2\mathcal{F}_{11} + c_2^2\mathcal{F}_{22} + 2c_1c_2\mathcal{F}_{12} \tag{1.59}$$

The $\mathcal{F}_{ij}$ term consider the attractive-repulsive effect between the $i$ and $j$ molecules, and is defined by a relation close to equation 1.7 for single fluid systems:

$$\mathcal{F}_{ij}(T) = \frac{1}{2}N_A\int_0^\infty \left(1 - e^{-U_{ij}(r)/kT}\right) 4\pi r^2 \mathrm{d}r \tag{1.60}$$

When non symmetric solutions are considered, the intramolecular potentials are one equal to each other, thus $U_{11} = U_{22} \neq U_{12}$ and then $\mathcal{F}_{11} = \mathcal{F}_{22} \neq \mathcal{F}_{12}$. The order parameter is then introduced:

$$g_{ex} = 2RT\rho\left(\mathcal{F}_{12} - \mathcal{F}_{11}\right)\phi(1-\phi) \tag{1.61}$$

Rewriting equation 1.61:

$$g_{ex}(T,p,\phi) = RT\Psi\phi(1-\phi) \tag{1.62}$$

Where $\Psi$ is the so called Margules coefficient:

$$\Psi(T,p) = 2\rho\left(\mathcal{F}_{12} - \mathcal{F}_{11}\right) \tag{1.63}$$

For an ideal mixture, since $\mathcal{F}_{11} = \mathcal{F}_{12}$ the equation above yields $\Psi = 0$. If the mixture is composed by two Van der Waals fluids at constant pressure, substituting equation 1.8 and assuming the Van Laar hypotesis on the regular mixtures, the Margules coefficient yields the following:

$$\Psi(T) = \frac{2\rho}{RT}\left(a_{11} - a_{12}\right) = \frac{4\pi}{3}\frac{\rho N_A^2 l^6}{RTd^3}\left(U_{0,12} - U_{0,11}\right) \tag{1.64}$$

Where $U_{0,11}$ and $U_{0,12}$ are the modulus of the intermolecular potential between molecules of the same species and different species, respectively; furthermore, introducing the Margules coefficient in to equation 1.61, the Gibbs free energy does not depend directly on the temperature; the physical meaning of the Margules coefficient is clear from Figure 2.2. Finally equation 1.52 yields to the following:

$$g_{Th} = RT\ln\rho + RT\left[\phi\ln\phi + (1-\phi)\ln(1-\phi) + \Psi\phi(1-\phi)\right] \tag{1.65}$$

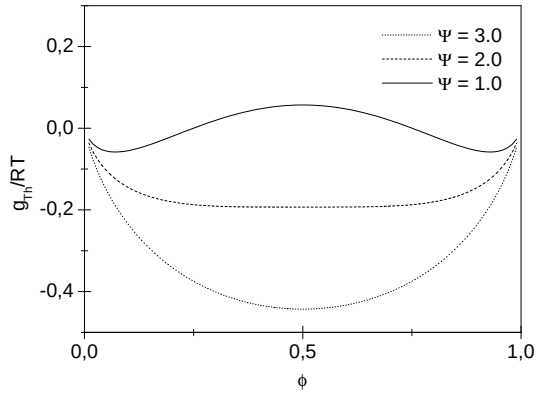


Figure 1.7: Evolution of the Gibbs thermodynamical free energy with the Margules parameter $\Psi$ on the energy-concentration ($\frac{g_{Th}}{RT} - \phi$) diagram whit unitary density

### 1.5.2 Coexistence and separation of binary mixtures

As reported in Section 1.4.1 the thermodynamical state of a single phase monocomponent system is completely defined when two state variables (i.e. $p$ and $T$) are defined, on the other hand when two phases coexist, the thermodynamical state of a single component system is determined just fixing one of the state variable. In the case of two component system, the Gibbs phase rule reads $v = 4 - f$, thus four state variables can be chosen to describe the system, but only two of them are independent from each other if the system shows two phases ($f = 2$). Usually the state variables chosen to study the thermodynamics of binary mixtures are the pressure $p$, the temperature $T$ and the concentration of

the two components $c_1$ and $c_2$. For each single phase component the generalized chemical potential is defined; since the two fluids are showing only one phase, the pressure cannot be considered equal between them and thus the chemical potential has the following definition:

$$RT\mu_{Th,i} = \left(\frac{\partial g_{Th}(c_i)}{\partial c_i}\right)_{i \neq j} \tag{1.66}$$

In the classical multiphase theory, the chemical potential must be the same in each phase $A$ and $B$ of the two fluids, thus $\mu_1^A = \mu_1^B$ and obviously $\mu_2^A = \mu_2^B$. Since, as shown at the beginning of section 1.5, the concentration of the two fluids are dependent one from each other and the thermodynamical chemical potential depends on the concentration of the two species, there must be a relation between $\mu_1$ and $\mu_2$. The relation is the so-called Gibbs-Duhem relation which can be rewritten in the following form [27]:

$$c_1 \nabla \mu_1 = c_2 \nabla \mu_2 \tag{1.67}$$

The definition of Gibbs free energy for a binary system:

$$g_{Th} = u - Ts + pv + RT\phi\mu_1 + RT\phi\mu_2 \tag{1.68}$$

And in differential form:

$$\mathrm{d}g_{Th} = -s\mathrm{d}T + v\mathrm{d}p + RT\mu\mathrm{d}\phi \tag{1.69}$$

Where $\mu = \mu_1 - \mu_2$ is the chemical potential difference; equation 1.45 shows that the chemical potential is the conjugate quantity of the concentration order parameter $\phi$. The chemical potential difference can be computed starting from the following identities:

$$RT\mu_1(T,p,\phi) = g_{Th}(T,p,\phi) + \left(\frac{\mathrm{d}g_{Th}}{\mathrm{d}\phi}\right)(1-\phi) = -s\mathrm{d}T + v\mathrm{d}p + RT\mu\mathrm{d}\phi \tag{1.70}$$

$$RT\mu_2(T,p,\phi) = g_{Th}(T,p,\phi) + \left(\frac{\mathrm{d}g_{Th}}{\mathrm{d}\phi}\right)\phi \tag{1.71}$$

Obtaining the following equation:

$$\mu = \mu_1 - \mu_2 = \frac{\mathrm{d}g_{Th}/RT}{\mathrm{d}\phi} = \ln\left(\frac{\phi}{1-\phi}\right) + \Psi(1-2\phi) \tag{1.72}$$

Where equation 1.65 has been substituted. The equation above shows the dependence of the the chemical potential on the order parameter $\phi$ when the pressure $p$ and temperature $T$ of the system are fixed; from equation 1.72 is clear that the chemical potential $\mu$ and the concentration order parameter $\phi$ play, for the binary mixtures, the same role of the pressure $p$ and specific volume $v$ for the single component systems. In the same way of the single component systems, $\mu$ represents the tangent line of Gibbs free energy curve, and it is the same for both phases $A$ and $B$ at equilibrium. Therefore, from equation 1.71 is possible to calculate the equilibrium concentrations $\phi_e^A$ and $\phi_e^B$ of the two phases knowing that $\phi_e^A = 1 - \phi_e^B$, accordingly to the order parameter definition. If symmetric mixtures are considered, the tangent to the Gibbs free energy curve is horizontal and $\mu = 0$. The same considerations made for the single component system can be extended to the binary systems, where $\mu$ and $\phi$ play the same role of $p$ and $v$. The chemical potential difference versus temperature diagram $(\mu - T)$ shows a liquid-liquid equilibrium curve which stops at the critical point, characterized by a critical temperature $T_C$ and a critical difference of chemical potential $\mu_C = 0$; for symmetric mixtures the difference of chemical potential is zero for every equilibrium point. At higher temperatures $T > T_C$ the system appears as a single phase, whereas below $T_C$ the system moves to a two phase stable configuration. Near the critical point the composition of the two phases $\phi_1 = \phi$ and $\phi_2 = \phi + \delta\phi$ tends to be equal, thus the critical difference of chemical potential $\Delta\mu_C$ is almost the same; expanding $\Delta\mu_C$ in Taylor series around the critical point, the following is obtained:

$$\begin{aligned} \mu_C(T,\phi) &= \mu_C(T,\phi+\delta\phi) \\ &= \mu_C(T,\phi) + \left(\frac{\partial\mu}{\partial\phi}\right)_{T_C,p_C}\delta\phi + \frac{1}{2}\left(\frac{\partial^2\mu}{\partial\phi^2}\right)_{T_C,p_C}(\delta\phi)^2 + \ldots \end{aligned} \tag{1.73}$$

Dividing then all the terms of equation 1.72 by $\phi$ and letting $\delta\phi \to 0$ the following relation for the critical point is obtained:

$$\left(\frac{\partial\mu}{\partial\phi}\right)_{T_C,p_C} = 0 \tag{1.74}$$

Where the equation above is only the limit case of the more general inequality $(\partial\mu/\partial\phi)_{T,p} \leq 0$, which represents the internal stability of the two phases. Expanding then $\delta g_{Th}$ in a power series of $\delta\phi$ with constant pressure and temperature:

$$\begin{aligned} \delta g_{Th} &= \left(\frac{\partial g_{Th}}{\partial \phi}\right)_{T,p} \delta\phi + \frac{1}{2}\left(\frac{\partial^2 g_{Th}}{\partial \phi^2}\right)_{T,p} (\delta\phi)^2 \\ &+ \frac{1}{3!}\left(\frac{\partial^3 g_{Th}}{\partial \phi^3}\right)_{T,p} (\delta\phi)^3 + \frac{1}{4!}\left(\frac{\partial^4 g_{Th}}{\partial \phi^4}\right)_{T,p} (\delta\phi)^4 + ... \end{aligned} \tag{1.75}$$

Near an equilibrium point the following relation must be satisfied:

$$\delta u - T\delta s + p\delta v - RT\mu\delta\phi > 0 \tag{1.76}$$

Thus, substituting equation 1.66 and equation 1.74, the following relation is reached:

$$\frac{1}{3!}\left(\frac{\partial^2 \mu}{\partial \phi^2}\right)_{T_C,p_C} (\delta\phi)^3 + \frac{1}{4!}\left(\frac{\partial^3 \mu}{\partial \phi^3}\right)_{T_C,p_C} (\delta\phi)^4 + ... > 0 \tag{1.77}$$

The inequality above must be satisfied for every arbitrary and howbeit small value of $\delta\phi$ leading the following solution:

$$\left(\frac{\partial^2 \mu}{\partial \phi^2}\right)_{T_C,p_C} = 0, \qquad \left(\frac{\partial^3 \mu}{\partial \phi^3}\right)_{T_C,p_C} > 0. \tag{1.78}$$

Equations 1.78 allow to impose an horizontal inflection on the chemical potential difference $\mu$ versus concentration $\phi$ diagram (reported in Figure 1.8.

Imposing the horizontal inflection of the $\mu-\phi$ curve at the critical point, from equation 1.72 $\phi_C^A = \phi_C^B = 1/2$ and the Margules coefficient becomes $\Psi = 2T_C/T$. If a liquid mixture is at equilibrium with chemical potential below the critical point, it shows two coexisting phase $A$ and $B$; following the Gibbs phase rule, since there are $n = 2$ components and $f = 2$ phases [5], the system shows two degrees of freedom, leading a phase transition at constant chemical potential when the concentrations are fixed. Defining the generalized chemical potential in the following way:

$$\Phi = g_{Th} - \mu\phi \tag{1.79}$$

[5] each fluid shows liquid and vapor phase

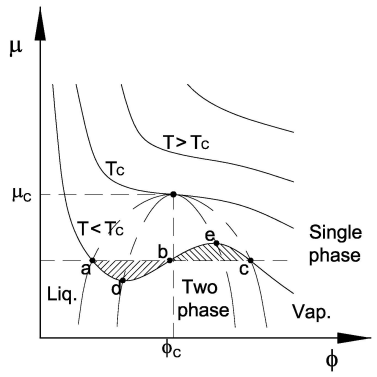


Figure 1.8: Isothermal isobaric curves on chemical potential difference-concentration diagram ($\mu$-$\phi$) for a binary component system

Where its differential form reads the following, where $(\partial\Phi/\partial\mu)_{T,p} = RT\phi$ has been evidenced:

$$\mathrm{d}\Phi = -s\mathrm{d}T + v\mathrm{d}P - RT\phi\mathrm{d}\mu \tag{1.80}$$

In this way $\Delta\mu$ can be calculated considering that, by definition, at equilibrium also the generalized chemical potentials of the two phases must be the same:

$$\Phi^A - \Phi^B = \int_a^c \mathrm{d}\Phi_{Th} = 0 \rightarrow \int_a^c \phi\mathrm{d}\mu = \int_a^c \phi \left(\frac{\partial\mu}{\partial\phi}\right)_{T,p} \mathrm{d}\phi \tag{1.81}$$

Where the phase transition temperature and pressure have been kept constant, and the $a$ and $c$ points are respectively the saturation (or equilibrium) points of the liquid and vapor phase and are reported in Figure 1.8. As for a single component mixture, a geometrical meaning of the equation 1.81 is founded in to the equivalence between the shaded areas comprised between points $a-b$ and $b-c$ of the $\mu-\phi$ diagram. The composition $\phi^A$ and $\phi^B$ of each of the two phases can be obtained from the Gibbs free energy of the system 1.65, imposing that at equilibrium the difference of chemical potential of both phases is equal to zero. The equation 1.81 express the the fact that at equilibrium the two phase binary system is isothermal, isobaric with zero difference of chemical potential;

imposing $\mu = (\partial g_{Th}/\partial\phi)_{T,p}$ the first two conditions are satisfied, thus as mentioned above, only the equality to zero of the chemical potential differences is needed.

$$\mu^A = \mu^B = 0 \rightarrow \left(\frac{\partial g_{Th}}{\partial \phi}\right)^A_{T,p} = \left(\frac{\partial g_{Th}}{\partial \phi}\right)^B_{T,p} \rightarrow \phi_e^A, \phi_e^B \tag{1.82}$$

A typical shape of the Gibbs thermodynamical free energy with respect to the concentration, for symmetric binary mixtures under their critical temperature ($T < T_C$) is reported in Figure 1.9; the equilibrium points $a$ and $c$ are also represented with their respective equilibrium concentration values.

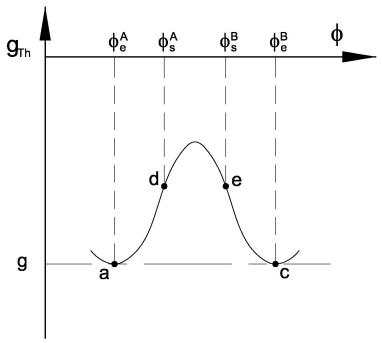


Figure 1.9: Typical Gibbs thermodynamical free energy for a binary symmetric mixture on free energy concentration ($g_{Th}$-$\phi$) diagram

If the mixture is not symmetric the typical $g_{Th} - \phi$ curve is reported in Figure 1.10, which is similar to the $f_{Th} - v$ curve of a single component system (reported in Figure 1.5). In this case it is still true that $\mu^A = \mu^B$ even if it is not always identical to zero, thus the tangent to the Gibbs thermodynamical free energy curve is in general, non-horizontal.

In Figure 1.8 inside the locus of the equilibrium points, the spinoidal curve have been reported and it represents the locus of all the points like $d$ and $e$ which satisfies $(\partial\mu/\partial\phi)_{T,p} = 0$ condition. The same considerations made above for the single component systems, can be extended to the binary mixtures; thus, all the points which lay out the region under the equilibrium bell curve represents homogeneous single phase mixtures in a state of stable equilibrium,

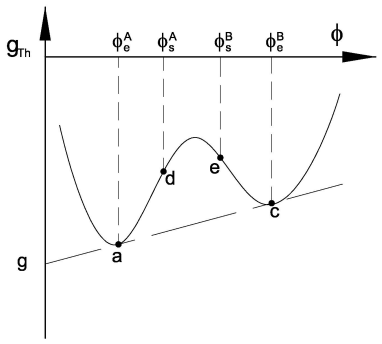


Figure 1.10: Typical Gibbs thermodynamical free energy for a binary non symmetric mixture on free energy concentration ($g_{Th}$-$\phi$) diagram

while the points laying inside the equilibrium bell curve represents states out of equilibrium. Furthermore the points comprised in the portion of the diagram between the two bells are in a condition of meta-stable equilibrium, thus they are stable until an howbeit amount of energy is introduced into the system (activation energy) and the system start to separate in two phases. The points lying inside the spinoidal curve are unstable equilibrium points, thus any infinitesimal perturbation leads the system to separate in two phases. The spinoidal points are determined imposing the following condition on the Gibbs thermodynamical free energy equation for a binary mixture (eq. 1.65):

$$\left(\frac{\partial \mu}{\partial \phi}\right)^{A}_{T,p} = \left(\frac{\partial \mu}{\partial \phi}\right)^{B}_{T,p} = 0 \rightarrow \left(\frac{\partial^2 g_{Th}}{\partial \phi^2}\right)^{A}_{T,p} = \left(\frac{\partial^2 g_{Th}}{\partial \phi^2}\right)^{B}_{T,p} = 0 \rightarrow \phi_s^A, \phi_s^B \tag{1.83}$$

### 1.5.3 Diffuse interface of binary systems

In the previous sections the concentration of the two components has been considered constant, in this way the interface between the two fluids has been implicitly supposed to be of zero thickness and the concentration parameter $\phi$ to change in a discontinuous way from $\phi_1 = \phi$ (for the fluid 1) to $\phi_2 = (1 - \phi)$ (for fluid 2), according to the Sharp Interface model. In this section the composition of the system is supposed to be non-constant and to change in a continuous way

across the domain; thus the Gibbs free energy can be rewritten as follows:

$$g(\mathbf{x}) = g_{Th}(\mathbf{x}) + \Delta g_{NL}(\mathbf{x}) \tag{1.84}$$

Where $g_{Th}(\mathbf{x})$ is the Gibbs thermodynamical free energy reported by equation 1.65 for a constant composition system, while $\Delta g_{NL}(\mathbf{x})$ is the non local effect due to the composition changes and typical of the diffuse interface approach. In fact if the two fluids at equilibrium are separated by an interface, the last term on the RHS of equation 1.84 represent the interfacial free energy. Following the procedure of Section 1.4.3, the expression of the interfacial free energy, originally due to Cahn and Hilliard [7], is obtained:

$$\Delta g_{NL}(\mathbf{x}) = \frac{1}{2} RTa^2 \left(\nabla\phi\right) \tag{1.85}$$

Thus equation 1.84 yields the following, where $\phi = \phi(\mathbf{x})$:

$$g(\phi, \nabla\phi) = g_{Th}(\phi) + \frac{1}{2} RTa^2 \left(\nabla\phi\right) \tag{1.86}$$

Where $a = \sqrt{\frac{9\pi T_C}{4T}} d$ can be considered as an interface characteristic length; in this way is easy to understand that the composition changes, or the presence of an interface, increases the system Gibbs free energy of a quantity dependent on the gradient of the composition. Following the procedure of Section 1.4.5 is possible to find an expression for the surface tension, which is defined as the integral Gibbs free energy on the surface volume:

$$\sigma = \int g_{\phi,\nabla\phi} = \frac{\rho l}{M} RT(\Delta\phi)^2 \frac{a^2}{l^2} \tag{1.87}$$

Where $(\Delta\phi)^2$ is the square of the $\phi$ changing magnitude across the interface, $M$ is the mobility of the mixture and $l \simeq a/\sqrt{(\Psi - 2)/2}$ is the length of the interface at equilibrium.

### 1.5.4 Generalized chemical potential of binary systems

To find the formulation of the generalized chemical potential for a binary system, the integral Gibbs free energy has to be minimized (following the same procedure used in Section 1.4.4):

$$\int_V g_{\phi,\nabla\phi} \mathrm{d}^3\mathbf{x} = min \tag{1.88}$$

Where the mass conservation constraint is introduced:

$$\int_V \phi(\mathbf{x}) \mathrm{d}^3\mathbf{x} = const \tag{1.89}$$

The solution of the minimum problem is obtained applying the Lagrange multipliers to the integral equation 1.88 and using the virtual works principle. Applying an arbitrary, compatible and howbeit small change in composition $\delta(\mathbf{x})$ on to the minimum problem, it yields to:

$$\int_V \left[g_{\phi,\nabla\phi} - RT\tilde{\mu}\phi\right] \mathrm{d}^3\mathbf{x} = 0 \tag{1.90}$$

Where $RT\tilde{\mu}$ is the Lagrangian multiplier of the system to be determined using the mass conservation constraint. Considering the virtual works principle applied to the free energy $g$, since $\delta\phi$ is arbitrary, the following equation is obtained:

$$\delta g = \frac{\partial g}{\partial \phi}\delta\phi + \frac{\partial g}{\partial(\nabla_i\phi)}\delta(\nabla_i\phi) \qquad \text{where} \qquad \delta(\nabla_i\phi) = \nabla_i\delta\phi \tag{1.91}$$

The last equality is possible because of the arbitrary of the virtual variation of concentration. The volume integral of the equation above yields to:

$$\int_V \left[\frac{\partial g}{\partial \phi}\delta\phi + \frac{\partial g}{\partial(\nabla_i\phi)}\delta(\nabla_i\phi)\right] \mathrm{d}^3\mathbf{x} = \int_V \frac{\partial g}{\partial \phi}\delta\phi \mathrm{d}^3\mathbf{x} + \int_V \frac{\partial g}{\partial(\nabla_i\phi)}\delta(\nabla_i\phi)\mathrm{d}^3\mathbf{x} \tag{1.92}$$

The second term in the RHS of the equation above can be rewritten via the Gauss' theorem:

$$\int_V \frac{\partial g}{\partial(\nabla_i\phi)}\delta(\nabla_i\phi)\mathrm{d}^3\mathbf{x} = \int_{\partial V} n_i \frac{\partial g}{\partial(\nabla_i\phi)}\delta(\phi)\mathrm{d}^2\mathbf{x} - \int_V \nabla_i\left(\frac{\partial g}{\partial(\nabla_i\phi)}\right)\delta(\phi)\mathrm{d}^3\mathbf{x} \tag{1.93}$$

The concentration, due to the boundary conditions, has zero gradient on the domain borders, thus, since the virtual changes of concentration must be compatible with the concentration field, $\delta\phi = 0$ on the borders of the domain.

for this reason the first integral on the RHS of the equation above is identically null, thus the equation 1.90 yields to the following form:

$$\int_V \left[\frac{\partial g}{\partial \phi} - \nabla_i \left(\frac{\partial g}{\partial(\nabla_i \phi)}\right) - RT\tilde{\mu}\right] \delta\phi \mathrm{d}^3\mathbf{x} \tag{1.94}$$

From equation 1.94, since the integral must be equal to zero for any arbitrary, compatible and howbeit small value of $\delta\phi$, the integrand function must be null and then the Euler-Lagrange equation is obtained.

$$\tilde{\mu} = \frac{1}{RT}\frac{\delta g}{\delta \phi} = \frac{1}{RT}\left[\frac{\partial g}{\partial \phi} - \nabla_i \frac{\partial g}{\partial(\nabla_i \phi)}\right] = \mu(\phi) - \frac{1}{RT}\nabla_i \frac{\partial g}{\partial(\nabla_i \phi)} \tag{1.95}$$

Substituting then the equation of the free energy $g$ in to the equation 1.94, the generalized chemical potential $\tilde{\mu}$ reads:

$$\begin{aligned} \tilde{\mu} &= \mu(\phi) - a^2\nabla^2\phi \\ &= \ln\left(\frac{\phi}{1-\phi}\right) + \Psi(1-2\phi) - a^2\nabla^2\phi \end{aligned} \tag{1.96}$$

Where in the equation above the expression of the thermodynamical chemical potential difference (eq. 1.72) has been substituted.

## 1.6 Generalized diffusion equation

In the diffuse interface approach, the order parameter $\phi$ is defined to change smoothly between two equilibrium values, generating a transition zone called interface. Since the order parameter is non constant across the interface, its dynamics can be described by a diffusion kind equation. The generalized diffusion equation is derived from the general form of the continuity equation following reported, where $\mathrm{D}/\mathrm{D}t$ is the material or Lagrangian derivative:

$$\frac{\mathrm{D}\phi}{\mathrm{D}t} + \nabla \cdot \mathbf{J}_\phi = r_\phi \tag{1.97}$$

Where the variation in time of the order parameter $\phi$ is equal to the difference between the gradient of the diffusive flux $\mathbf{J}_\phi$ and the chemical reaction generation term $r_\phi$. If the two components do not react when they are mixed

together, the generation term is equal to zero and equation 1.97 yields to the following:

$$\frac{\mathrm{D}\phi}{\mathrm{D}t} + \nabla \cdot \mathbf{J}_\phi = 0 \tag{1.98}$$

At first only the component 1 of the mixture is considered and the diffuse interface effects are neglected, thus the diffusive flux can considered as driven by the chemical potential of the substance and proportional to the substance concentration $c_1$ and to the diffusivity coefficient of the component. From these assumptions, the diffusive flux:

$$\mathbf{J}_1 = -Dc_1 \nabla \mu_1 \tag{1.99}$$

Where the chemical potential of the first component $\mu_1$ is obtained substituting equation 1.52 in to equation 1.71 and the $Dc_1$ term is introduced in order to obtain the classical Fick's law for non-critical conditions; the chemical potential has thus the following form:

$$\mathbf{J}_1 = -Dc_1 \left( \frac{\mathrm{d}\mu_1}{\mathrm{d}c_1} \nabla c_1 + \frac{\mathrm{d}\mu_1}{\mathrm{d}c_2} \nabla c_1 \right) \rightarrow \mathbf{J}_1 = -\tilde{D} \nabla c_1 \tag{1.100}$$

Where the modified diffusion coefficient $\tilde{D}$ is described by the following:

$$\tilde{D} = D\left(1 + 2\Psi c_1 c_2\right) \tag{1.101}$$

It can be shown that the diffusivity coefficient evidenced in the diffusive flux (eq. 1.99), do not depend on the concentration, thus it is equal for both components and the two fluxes have same modulus but opposite direction. From the Gibbs-Duhem relation (eq. 1.67), is possible to write the following equality:

$$\mathbf{J_1} = -\mathbf{J_2} \tag{1.102}$$

Furthermore, for ideal mixtures, which are far from their critical point and thus characterized by $\Psi \rightarrow 0$ or $c_i \rightarrow 0$, the modified diffusivity coefficient is equal to $D$ and then the equation 1.100 reduces to the original Ficks' law. Extending equation 1.99 to the case of the binary mixtures, the molar diffusivity flux yields the following formulation, where the concentrations of the two components have been expressed in terms of the order parameter $\phi$:

$$\mathbf{J}_\phi = -D\phi(1-\phi)\nabla\mu \tag{1.103}$$

Where $\mu = \mu_1 - \mu_2$. Introducing the Cahn-Hilliard term for the interface energy, the diffusive flux becomes:

$$\begin{aligned} \mathbf{J}_\phi &= -D\phi(1-\phi)\nabla\tilde{\mu} \\ &= -D\phi(1-\phi)\nabla\left[\ln\left(\frac{\phi}{1-\phi}\right) + \Psi(1-2\phi) - a^2\nabla^2\phi\right] \end{aligned} \tag{1.104}$$

The pure diffusive equation 1.98 can be rewritten in the following way:

$$\begin{aligned} \frac{\mathrm{D}\phi}{\mathrm{D}t} &= \nabla\cdot M_c(\phi)\nabla\tilde{\mu}(\phi) \\ &= \nabla\cdot M_c(\phi)\nabla\left[\ln\left(\frac{\phi}{1-\phi}\right) + \Psi(1-2\phi) - a^2\nabla^2\phi\right] \end{aligned} \tag{1.105}$$

Where $M_c(\phi)$ is the so called mobility and may assume many different forms, depending on the constitutive law chosen. Equation 1.105 is the so called Cahn-Hilliard equation [7] and its derivation was due first to Cahn and Hilliard in 1958. If the phase field equation is coupled with the fluid flow-field, a convective term must be added to equation 1.98, in this way the convective fluxes are kept in account. From the mathematical point of view, the convective-diffusive equation can be obtained from equation 1.98 just substituting the definition of the material derivative $\mathrm{D}/\mathrm{D}t$.

$$\frac{\partial\phi}{\partial t} + \nabla\cdot\mathbf{J}_\phi + \mathbf{u}\cdot\nabla\phi = 0 \tag{1.106}$$

Where $\mathbf{u}$ is the velocity field vector. Thus the most general form of the Cahn-Hilliard equation is following reported:

$$\frac{\partial\phi}{\partial t} = \nabla\cdot M_c(\phi)\nabla\tilde{\mu}(\phi) - \mathbf{u}\cdot\nabla\phi \tag{1.107}$$

## 1.7 Phase field and motion equation coupling term

When a phase transition phenomena occurs, the Gibbs free energy of the system changes, in fact, moving from an unstable or meta-stable condition to a stable

state, it reaches its own minimum. The free energy drives the concentration changing and the behavior of the interface through the chemical potential [13]; thus, if the interface moves, is easy to understand that some kind of local body forces are acted on the fluid. To study the behavior of a phase-field coupled with a flow-field, a stress term has to be introduced in to the fluid momentum conservation equations. In order to achieve this scope, a binary mixture with constant density and composed by two fluids with the same density $\rho$ is studied; with these hypothesis the problem is restricted to symmetric binary mixtures of non-compressible flows, extensions to single components systems or compressible and non-symmetric mixtures can be founded in Lowengrub *et al.*[26] and Anderson *et al.*[1], even if the results are not too different. The object of this study are the non-dissipative mixtures, where there is no diffusion and thus the concentration field can be derived from the initial conditions known the velocity field. In fact defining $\mathbf{x}(t, \mathbf{x}_0)$ as the position of the fluid particle at time $t$ (with initial position $\mathbf{x}_0$ at $t = 0$) and the fluid velocity $\mathbf{u}(\mathbf{x}, t) = \dot{\mathbf{x}}(\mathbf{x}, t)$, the composition at time $t$ and position $\mathbf{x}(\mathbf{x}, t)$ of the field, depends only on the composition of the fluid element located at that point. Thus the concentration field $\phi(\mathbf{x}, t) = \phi(\mathbf{x})$ do not depend explicitly on the time, since the fluids do not diffuse, and thus $\dot{\phi} = 0$. Furthermore, if the system is non-dissipative it is also conservative, thus its dynamic equations can be obtained via the Hamilton's minimum action principle; in fact the motion of any conservative system is determined by a variational problem of the Lagrangian functional of the system configuration defined by the following equation:

$$\begin{aligned} \mathcal{L} &= T - V \\ &= \mathcal{L}(\mathbf{u}, \phi, \nabla\phi) = \frac{1}{2}\rho|\mathbf{u}|^2 - \rho g \end{aligned} \tag{1.108}$$

Where $\mathcal{L}$ is defined as the difference between the kinetic energy $T$ and the potential energy $V$ of the system; the latter, neglecting the gravitational term[6], is represented by the volume density of Gibbs free energy $\rho g$, where $\rho$ is the mass density of the mixture (which is constant). The Lagrangian of the system is subjected to incompressibility constraint, which can be derived as follows from

[6] In fact the natural convection is not considered in this formulation

the continuity equation 1.97:

$$\frac{\partial \phi}{\partial t} + \nabla(\rho \mathbf{u}) = 0 \rightarrow \rho \nabla \cdot \mathbf{u} + \mathbf{u} \cdot \nabla \rho = 0 \rightarrow \nabla \cdot \mathbf{u} = 0 \tag{1.109}$$

Where the functional $\mathcal{S}$, which has to be minimized on the spatial and temporal domain, can be expressed as:

$$\mathcal{S} = \int_0^t \int_V \mathcal{L}(\mathbf{v}, \phi, \nabla \phi) \mathrm{d}^3\mathbf{x} \mathrm{d}t \tag{1.110}$$

Since the minimization process is obtained via the virtual works principle, an arbitrary and albeit small displacement $\delta x_i$, compatible with the system configuration, has to be applied to the system, corresponding to a virtual change in the flow field. Since the virtual displacements are arbitrary, they have been chosen in order satisfy the following equality:

$$\delta \phi = \nabla_i \cdot \delta x_i = 0 \tag{1.111}$$

Applying the virtual variation to the functional 1.110, it yields to:

$$\begin{aligned} \delta \mathcal{S} &= \int_0^t \int_V \rho v_i \delta v_i \mathrm{d}^3\mathbf{x} \mathrm{d}t - \int_0^t \int_V \frac{\rho}{M_W} \delta g \mathrm{d}^3\mathbf{x} \mathrm{d}t \\ &- \int_0^t \int_V q(\nabla_i v_i) \mathrm{d}^3\mathbf{x} \mathrm{d}t \end{aligned} \tag{1.112}$$

Where $q = q(\mathbf{x}, t)$ is a function to be determined from the incompressibility constraint (eq. 1.109). Following the cinematical definition of velocity, the first integral on the RHS of equation 1.112 gives:

$$\int_0^t \int_V \rho v_i \delta v_i \mathrm{d}^3\mathbf{x} \mathrm{d}t = \int_0^t \int_V \rho v_i \delta \frac{\mathrm{d}x_i}{\mathrm{d}t} \mathrm{d}^3\mathbf{x} \mathrm{d}t \tag{1.113}$$

Again, because the arbitrary of the virtual displacemnts, $\delta(\mathrm{d}x_i) = \mathrm{d}(\delta x_i)$ , thus the integral above is rewritten in the following way:

$$\begin{aligned} \int_0^t \int_V \rho v_i \frac{\mathrm{d}}{\mathrm{d}t}(\delta x_i) \mathrm{d}^3\mathbf{x} \mathrm{d}t &= \int_V (\rho v_i \delta x_i)_{t_1}^{t_2} \mathrm{d}^3\mathbf{x} \mathrm{d}t - \int_0^t \int_V \rho \frac{\mathrm{d}v_i}{\mathrm{d}t}(\delta x_i) \mathrm{d}^3\mathbf{x} \mathrm{d}t \\ &= -\int_0^t \int_V \rho \frac{\mathrm{d}v_i}{\mathrm{d}t}(\delta x_i) \mathrm{d}^3\mathbf{x} \mathrm{d}t \end{aligned} \tag{1.114}$$

Where the virtual displacements at the beginning and at the end of the temporal integration have been assumed to be equal to zero, hence $\delta x_i(t_2) = 0$ and $\delta x_i(t_1) = 0$. Considering that the Gibbs free energy is dependent on the concentration $g = g(\phi, \nabla\phi)$, the second integral on the RHS of equation 1.112 yields to:

$$\begin{aligned} \int_0^t \int_V \delta g \mathrm{d}^3\mathbf{x}\mathrm{d}t &= \int_0^t \int_V \frac{\partial g}{\partial \phi}\delta\phi \mathrm{d}^3\mathbf{x}\mathrm{d}t \\ &+ \int_0^t \int_V \frac{\partial g}{\partial \nabla_j \phi}\delta\left(\nabla_j\phi\right)\mathrm{d}^3\mathbf{x}\mathrm{d}t \end{aligned} \tag{1.115}$$

Since the virtual displacement has been chosen in order to satisfy equality reported in equation 1.111, the virtual variation of the concentration field $\delta\phi$ is identically equal to zero and thus the first term on the RHS of the equation above is equal to zero. Furthermore, the following equality is derived:

$$\begin{aligned} \delta\left(\nabla_j\phi\right) &= \frac{\partial \nabla_j \phi}{\partial x_i}\delta x_i = \left(\nabla_i\nabla_j\phi\right)\delta x_i \\ &= \nabla_j\left(\delta\phi\right) - \left(\nabla_i\delta\phi\right)\nabla_j\left(\delta x_i\right) \\ &= -\left(\nabla_i\phi\right)\nabla_j\left(\delta x_i\right) \end{aligned} \tag{1.116}$$

Thus equation 1.115 gives the following:

$$\begin{aligned} \int_0^t \int_V \delta g \mathrm{d}^3\mathbf{x}\mathrm{d}t &= -\int_0^t \int_V \frac{\partial g}{\partial \nabla_j \phi}\left(\nabla_i\phi\right)\left(\nabla_j\delta x_i\right)\mathrm{d}^3\mathbf{x}\mathrm{d}t \\ &= -\int_0^t \oint_s n_j \frac{\partial g}{\partial \nabla_j \phi}\nabla_i\phi\delta x_i \mathrm{d}S\mathrm{d}t \\ &\quad + \int_0^t \int_V \nabla_j\left(\frac{\partial g}{\partial \nabla_k \phi}\nabla_i\phi\right)\delta x_i \mathrm{d}^3\mathbf{x}\mathrm{d}t \end{aligned} \tag{1.117}$$

Where the integral above has been integrate by parts; since the virtual displacements are equal to zero on the boundaries of the domain, the surface integral of equation 1.117 is identically null and the following expression is obtained:

$$\int_0^t \int_V \delta g \mathrm{d}^3\mathbf{x}\mathrm{d}t = \int_0^t \int_V \nabla_j\left(\frac{\partial g}{\partial \nabla_k \phi}\nabla_i\phi\right)\delta x_i \mathrm{d}^3\mathbf{x}\mathrm{d}t \tag{1.118}$$

The last integral on the RHS of equation 1.112 is then rewritten:

$$\begin{aligned}\int_0^t \int_V q\delta\left(\nabla_i v_i\right) \mathrm{d}^3\mathbf{x}\mathrm{d}t &= \int_0^t \oint_S n_i q \delta v_i \mathrm{d}S\mathrm{d}t - \int_0^t \int_V \delta v_i \left(\nabla_i q\right) \mathrm{d}^3\mathbf{x}\mathrm{d}t \quad (1.119)\\ &= -\int_V \left[\left(\nabla_i q\right)\delta x_i\right]_0^t \mathrm{d}^3\mathbf{x} + \int_0^t \int_V \left(\nabla_i \frac{\partial q}{\partial t}\right)\delta x_i \mathrm{d}^3\mathbf{x}\mathrm{d}t\\ &= \int_0^t \int_V \left(\nabla_i p\right)\delta x_i \mathrm{d}^3\mathbf{x}\mathrm{d}t\end{aligned}$$

Where the virtual variation of displacements and velocity have been considered identically zero at the boundaries, the same value has been assigned at the starting and ending integration time and $p = \partial q/\partial t$. Substituting equation 1.119 and equation 1.118 in to equation 1.114, the following integral is obtained:

$$\int_0^t \int_V \left(\rho \frac{\mathrm{d}v_i}{\mathrm{d}t} + \nabla_i p - \nabla_j P_{ji}\right) \mathrm{d}^3\mathbf{x}\mathrm{d}t = 0 \quad (1.120)$$

Where $P_{i,j}$ is the Cauchy stress tensor component:

$$P_{ji} = -\frac{\rho}{M_W}\frac{\partial g}{\partial\left(\nabla_i \phi\right)}\nabla_j \phi \quad (1.121)$$

Again, because of the arbitrariness of the virtual displacements and collecting properly the terms, equation 1.120 reads:

$$\rho\frac{\mathrm{D}\mathbf{v}}{\mathrm{D}t} + \nabla p - \nabla\cdot\mathbf{P} \rightarrow \rho\frac{\mathrm{D}\mathbf{v}}{\mathrm{D}t} = \mathbf{F}_b + \mathbf{F}_s \quad (1.122)$$

Where $\mathbf{F}_b$ and $\mathbf{F}_s$ are the body force and the surface force respectively. The former is equal to the divergence of the Couchy stress tensor $\nabla\cdot\mathbf{P}$ and the latter is equal to the pressure term gradient $\nabla p$. The $i$ component of the body force $\mathbf{F}_b$ can be rewritten as follows:

$$\begin{aligned}F_b, i = \nabla_j P_{i,j} &= -\frac{\rho}{M_W}\left[\nabla_j\left(\frac{\partial g}{\partial \nabla_i \phi}\right)\nabla_i\phi\left(\frac{\partial g}{\partial \nabla_j \phi}\right)\nabla_i\nabla_j\phi - \frac{\partial g}{\partial \phi}\right]\\ &= \frac{\rho RT}{M_W}\tilde{\mu}\nabla_i\phi - \frac{\rho}{M_W}\nabla_i g \quad (1.123)\end{aligned}$$

After substitution of equation 1.123 in to equation 1.122, the momentum equation yields the following conservative formulation:

$$\rho\frac{\mathrm{d}\mathbf{v}}{\mathrm{d}t} + \nabla\mathcal{P} = \rho RT M_W \tilde{\mu}\nabla\phi \quad (1.124)$$

Where the modified pressure term includes also the Gibbs free energy contribution:

$$\mathcal{P} = p + \rho g \tag{1.125}$$

Finally the Cauchy non dissipative stress tensor is rewritten:

$$\mathbf{P} = \begin{pmatrix} P_{11} & P_{12} & P_{13} \\ P_{21} & P_{22} & P_{23} \\ P_{31} & P_{32} & P_{33} \end{pmatrix}$$

In this way is easy to understand that the dynamics of a conservative fluid system out of equilibrium is driven by the pressure forces and by the body forces which are proportional to the divergence of the Couchy stress tensor. Thus, considering zero the surface forces, the fluid is forced to move from zones of high chemical potential, toward zones with low chemical potential.

# Chapter 2

# Governing equations

In this chapter the phase field model equations are derived following a pure mathematical approach, whereas the classical derivation of the flow field continuity and momentum equations is reported. The approach introduced to obtain the phase field equations does not ensure the thermodynamical consistency; this apparently lack of physical meaning can be easily overcome reducing the mathematical approach equations to the physical equations derived in the previous chapter; in this way the thermodynamical consistency of the model is ensured. In Section 2.1 the phase field equations obtained from the mathematical approach are reported an the consistency with the equations shown in Chapter 1 is proven. In section 2.2 the flow field governing equations are derived starting from the classical conservation principles. Finally in Section 2.3 the dimensional analysis of the equations is reported and the scaling units are shown.

## 2.1 Phase field governing equations

The mathematical derivation of the phase field for the study of systems out of equilibrium involves several phase field variables, which are continuous fields depending on the position vector $\mathbf{x}$ and time $t$. The first variable introduced is the order parameter $\phi = \phi(\mathbf{x})$ which represents the magnitude of one of the field variables (such as density or concentration) at each point of the domain.

### 2.1.1 Free energy

The phase field equations can be derived following the variational principle, thus a potential functional has to be introduced. One of the most used formulation is similar to the Helmholtz free energy equation reported in Section 1.4, thus it is usually called free energy. Following Cahn and Hillard [7] the free energy $f$, for a non equilibrium system, is expressed in terms of the order parameter $\phi$ and the square of its gradient as follows:

$$f(\phi, \nabla\phi) = \frac{1}{2}k|\nabla\phi|^2 + f_0(\phi) \tag{2.1}$$

As reported in the introductory section, the diffuse interface model can describe the dynamics of the coexisting phases of a non equilibrium system; in the same way is possible to describe the dynamics of the non-zero interface between the phases. The interface can be considered as a transition volume where the order parameter changes in a continuous way from the bulk value of the first phase to the bulk value of the second phase. In this zone the two phases are mixed together, thus the mixing free energy is stored inside the interface volume. The term $\frac{1}{2}k|\nabla\phi|^2$ of equation 2.1 keeps in account this free energy (Yue *et al.*[39]), where the positive parameter $k$ is the magnitude of the mixing energy. The second term in the RHS of equation 2.1 is the bulk energy stored in the pure phase domains and it drives the phase nucleation or separation. The system behavior is completely described by the free energy functional, thus the stable conditions are reached when $f(\phi, \nabla\phi)$ is minimized. On the other hand if the system is driven out of equilibrium, its morphology changes until the free energy reaches its extremum. The total free energy, calculated on the system volume $V$ is the following:

$$F(\phi) = \int_V \left[\frac{1}{2}k|\nabla\phi|^2 + f_0(\phi)\right] \mathrm{d}\mathbf{x} \tag{2.2}$$

It represents the total free energy stored into the system, due to the pure phases coexistence and to the mixing energy stored into the interface volume.

### 2.1.2 Chemical potential

To define the stability conditions of the system, the total free energy has to be minimized, obtaining the following equation:

$$\mu(\phi) = \frac{\partial F(\phi)}{\partial \phi(\mathbf{x})} = f_0'[\phi(\mathbf{x})] - k\nabla^2\phi(\mathbf{x}) \tag{2.3}$$

Where $\mu$ is the so-called chemical potential, which depends on the second derivative of the order parameter and on the first derivative of the ideal free energy $f_0'$; the latter is a function of $\phi$ to be properly chosen. Following Badalassi *et al.*[4] for a binary mixture the free energy function is usually chosen to be a double well potential which is defined by the following equation:

$$f_0(\phi) = \frac{\alpha}{4}\left(\phi - \sqrt{\frac{\beta}{\alpha}}\right)^2\left(\phi + \sqrt{\frac{\beta}{\alpha}}\right)^2 \tag{2.4}$$

Where $\alpha$ and $\beta$ are two positive constants which depends on the mixture properties. Substituting equation 2.4 in to equation 2.3, the following equilibrium profile is obtained:

$$\mu(\phi) = \alpha\phi^3 - \beta\phi - k\nabla^2\phi = 0 \tag{2.5}$$

Equation 2.5 admit two stable uniform solutions $\phi_\pm = \sqrt{\frac{\beta}{\alpha}}$ which represents the coexisting bulk phases and a non uniform solution. Van der Waals derived the solution for a planar interface normal to the $z$-direction [35], obtaining the equation following reported, where the thickness of the interface between the two phases is described in terms of $\beta$, $k$ and capillary width $\xi$:

$$\phi_0 = \phi_+ \tanh\left(\frac{z}{\sqrt{2}\xi}\right) \tag{2.6}$$

The capillary width is described by the following:

$$\xi = \pm\sqrt{\frac{\beta}{\alpha}} \tag{2.7}$$

The formulation chosen to describe the bulk free energy shows the same shape of the ideal free energy of a system driven under its critical point (equation 1.65), but it has a simpler mathematical description. A different description of the bulk phase in terms of order parameter has to be adopted instead the

description used in Section 1.5, in fact the bulk free energy equation is symmetrical to $\phi = 0$ point. For the $A$ phase the order parameter leads $\phi^A = (1-\phi)/2$ whereas for the $B$ phase the order parameter yields $\phi^B = (1+\phi)/2$, in order to satisfy the equality $\phi^A + \phi^B = 1$.

### 2.1.3 Surface tension

The surface tension is defined as the integral of the free energy density across the surface thickness, this yields the following equation:

$$\sigma = k\rho \int_{-\infty}^{+\infty} \left( \frac{\mathrm{d}\phi_0}{\mathrm{d}z} \right)^2 \mathrm{d}z \tag{2.8}$$

Substituting the equation 2.6, the integral yields to the following equation:

$$\sigma = \rho \frac{\sqrt{2}}{3} \frac{k^{\frac{1}{2}} \beta^{\frac{3}{2}}}{\alpha} \tag{2.9}$$

From equations 2.7 and 2.9 can be observed that the interface thickness and the surface tension are defined and thus controlled by the physical parameters $\alpha$, $\beta$ and $k$. If the interface thickness is defined as the width of the domain where $\phi$ changes from $0.9\phi_A$ to $0.9\phi_B$, the equation 2.6 yields $2\sqrt{2}\xi \mathrm{arctanh}(0.9) = 4.164\xi$; this means almost the 98.5% of the integral surface tension, of a plane interface, is contained in a volume of $4.164\xi$ width and in that volume the parameter $\phi$ changes the 90% of its magnitude. From this definition, the interface thickness $l$ can be defined as $l \simeq 4.16\xi$.

### 2.1.4 Cahn Hilliard equation

The dynamics of the phase system is described by the Cahn-Hilliard equation, which is obtained from the generalized time dependent Fick's law. There the interfacial diffusion fluxes are considered proportional to the gradient of the chemical potential (equation 2.3) obtaining the following:

$$\frac{\partial \phi}{\partial t} + \mathbf{u} \cdot \nabla \phi = \nabla \cdot (M(\phi) \nabla \mu) \tag{2.10}$$

Where $\mathbf{u}$ is the velocity vector and $\mathbf{u} \cdot \nabla \phi$ is the convective term. The mobility (or Osanger coefficient) $M(\phi)$ is, in the most general formulation of the model, a function dependent on the order parameter, even if it can be kept constant in

order to obtain a simpler formulation (see Yue *et al.*[39]). Equation 2.10 can be used to simulate either processes of nucleation or phase separation in presence or even in absence of flow field.

## 2.2 Flow field governing equations

When the phase field is coupled with a flow field, the dynamics of the interface is driven either from the free energy of the two species and the forces acted by the flow field. Hence the evolution of the phase field can be obtained coupling the equations reported in the section above with the flow field governing equations, which are derived in the present section.

### 2.2.1 Continuity equation

Considering a fluid domain, the mass conservation or continuity equation can be expressed in the following way:

$$\frac{\partial \rho}{\partial t} + \nabla \cdot (\rho \mathbf{u}) = 0 \tag{2.11}$$

Equation 2.11 can be particularized for a non compressible flow field, in this case the density $\rho$ of the fluid is constant, so it can be considered uniform and steady.

$$\nabla \cdot \mathbf{u} = 0 \tag{2.12}$$

Equation 2.12 can be rewritten in the Eistein's scalar notation:

$$\frac{\partial u_i}{\partial x_i} = 0 \qquad \text{with} \qquad i = 1, 2, 3 \tag{2.13}$$

### 2.2.2 Navier-Stokes equations

The motion of a fluid can be described by a set of partial differential equations called Navier-Stokes momentum equations, which are derived from the application of the Newton's second law to a fluid system. Following Pope [30] these equations are derived on the continuity approximation, considering the fluid as a continuum media; this is possible because the spatial and temporal

scales of the molecular motion are of several orders lower in magnitude than the characteristic scales of the fluid motion. The dynamics of a fluid element can be described through Newton's second law keeping in account that its acceleration is proportional to the forces acting on the fluid element. These forces can be divided in two groups, the body forces and the surface forces. In the former group the gravitational effect is considered whereas in to the latter the molecular interactions are considered. The scalar component of the momentum vectorial equation yields to the following (where the Lagrangian derivative has been used):

$$\rho \frac{\mathrm{D}u_i}{\mathrm{D}t} = \frac{\partial \tau_{i,j}}{\partial x_j} - \rho \frac{\partial \psi}{\partial x_j} \tag{2.14}$$

Where $u_i$ is the velocity components, $\tau_{i,j}$ is the surface stress tensor and $\psi = gz$ is the gravitational potential in terms of gravitational acceleration $g$ and vertical coordinate $z$.

For fluids with constant viscosity $\eta$ the stress tensor can be written in this way:

$$\tau_{i,j} = \tau_{i,j}(\mathbf{x}, t) = -p\delta_{i,j} + \left( \eta \frac{\partial u_i}{\partial x_j} + \frac{\partial u_j}{\partial x_i} \right) \tag{2.15}$$

Equation 2.15 represents the stress tensor in terms of isotropic and deviatoric contributions; the former is due to the pressure term $p\delta_{i,j}$ where $\delta_{i,j}$ is the Kroneker's delta, the latter depends on the spatial variations of the velocity field and on the fluid viscosity. Substituting the 2.15 in to equation 2.14 and considering the continuity equation 2.12, the Navier-Stokes equation yields to:

$$\rho \frac{\mathrm{D}u_j}{\mathrm{D}t} = \eta \frac{\partial^2 {}_j}{\partial x_i \partial x_i} - \frac{\partial p}{\partial x_j} - \rho \frac{\partial \psi}{\partial x_j} \tag{2.16}$$

Thus, defining the pressure term as $\mathcal{P} = p + \rho\psi$ it yields to:

$$\rho \frac{\mathrm{D}\mathbf{u}}{\mathrm{D}t} = \eta \nabla^2 \cdot \mathbf{u} - \nabla \cdot \mathcal{P} \tag{2.17}$$

Then, substituting the substantial derivative in terms of Eulerian derivative, the Navier-Stokes equation in its vectorial form becomes:

$$\rho \frac{\partial \mathbf{u}}{\partial t} + \mathbf{u} \cdot \nabla \mathbf{u} = \eta \nabla^2 \cdot \mathbf{u} - \nabla \cdot \mathcal{P} \tag{2.18}$$

Using the Einstein's notation, the generical scalar component of the equation above yields to:

$$\rho\frac{\partial u_i}{\partial t} + u_i\frac{\partial u_j}{\partial x_j} = \eta\frac{\partial^2 u_i}{\partial x_i^2} - \frac{\partial p}{\partial x_i} \qquad \text{whith} \qquad i,j = 1,2,3 \tag{2.19}$$

### 2.2.3 Capillary stress

When a two phase system reaches an equilibrium state, no forces arise between the two fluids, thus the system morphology does not change. On the contrary when the two phases are not at equilibrium, a capillary force $\mathbf{F}_\phi$ arises at the interface of the two phases [23]. This force is described as the gradient of the conservative stress tensor $\mathbf{P}$.

$$\mathbf{F}_\phi = \nabla \cdot \mathbf{P} \tag{2.20}$$

Where $\mathbf{P}$ is also called Cauchy stress tensor and it is obtained minimizing the Lagrangian functional $\mathcal{L}$ (see Section 1.7) defined for the system. The capillary body force has the following formulation:

$$F_\phi = \mu\nabla \cdot \phi - \nabla f \tag{2.21}$$

Substituting in to the flow field momentum equation 2.16 and defining the modified pressure $\mathcal{P}' = p + \rho\psi - \nabla f$, the following equation is obtained:

$$\rho\frac{\partial \mathbf{u}}{\partial t} + \mathbf{u}\cdot\nabla\mathbf{u} = \eta\nabla\cdot\mathbf{u} - \nabla\cdot\mathcal{P}' + \mu\nabla\cdot\phi \tag{2.22}$$

Where the modified pressure term $\mathcal{P}'$ includes also the free energy contribution of equation 2.21.

## 2.3 Dimensional analysis

The phase field model of a binary partial miscible mixture is governed from the following set of partial differential equations:

$$\rho\frac{\partial u_i}{\partial t} + u_i\frac{\partial u_j}{\partial x_j} = \mu\frac{\partial^2 u_i}{\partial x_i^2} - \frac{\partial \mathcal{P}'}{\partial x_i} + \mu\frac{\partial \phi}{\partial x_i} \qquad \text{whith} \qquad i,j = 1,2,3 \tag{2.23}$$

$$\frac{\partial u_i}{\partial x_i} = 0 \qquad \text{with} \qquad i = 1, 2, 3 \tag{2.24}$$

$$\mu(\phi) = \alpha\phi^3 - \beta\phi - k\frac{\partial^2 \phi}{\partial x_i^2} = 0 \qquad \text{with} \qquad i = 1, 2, 3 \tag{2.25}$$

$$\frac{\partial \phi}{\partial t} + v_i \frac{\partial \phi}{\partial x_i} = \frac{\partial}{\partial x_j}\left(M\frac{\partial \mu}{\partial x_i}\right) \qquad \text{with} \qquad i, j = 1, 2, 3 \tag{2.26}$$

In order to avoid the dependence of the model to the domain dimensions and to the fluid properties, the equations above are rewritten in a non dimensional form; in this way the problem is controlled by a set of non dimensional parameters. The analysis reported through this work is based on a channel geometry characterized by two infinite walls, as reported in Figure 2.1, where $L_x = 4\pi H$, $L_y = 2\pi H$ and $L_z = 2H$. These three dimensions are reported respectively in the lengthwise, spanwise and wall-normal directions of the referring frame.

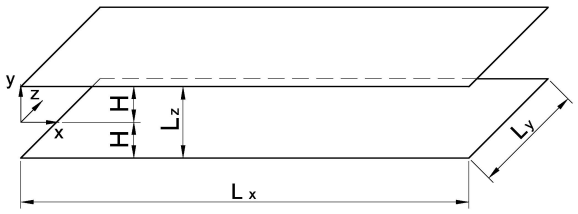


Figure 2.1: The channel geometry with reference frame

### 2.3.1 Dimensionless flow field equations

Equation 2.23 and equation 2.24 have been rewritten in a non-dimensional form using the so-called *outer-scaling units* (commonly indicated with the "-" apex). They involve the half $H$ height of the channel as the characteristic length-scale of the flow, the shear velocity $U_\tau$ as the flow field velocity-scale. The former

scaling quantity is reported in Figure 2.1, whereas the latter is defined in the following way:

$$U_\tau = \sqrt{\frac{\tau_w}{\rho}} \tag{2.27}$$

In the same way, the mean value of the friction stress at the wall $\tau_w$ can be defined from a macroscopical force balance along the channel in the lengthwise direction:

$$\tau_w = H\frac{\mathrm{d}\bar{p}}{\mathrm{d}x} \tag{2.28}$$

Where $\bar{p} = \bar{p}(x)$ is the pressure term averaged on the spanwise and wall normal directions; substituting it to equation 2.28, the following equation is obtained:

$$U_\tau = \sqrt{\frac{H}{\rho}\frac{\mathrm{d}\bar{p}}{\mathrm{d}x}} \tag{2.29}$$

Stating this, the non dimensional groups used for the dimensional analysis are the following:

$$x^- = \frac{x}{H}, \qquad u^- = \frac{u}{U_\tau}, \qquad t^- = \frac{tU_\tau}{H}, \qquad \mathcal{P}'^- = \frac{\mathcal{P}'H}{\rho U_\tau^2}. \tag{2.30}$$

The dimensionless continuity equation reads:

$$\frac{\partial u_i^-}{\partial x_i^-} = 0 \qquad \text{with} \qquad i = 1,2,3 \tag{2.31}$$

Whereas the dimensionless Navier-Stokes equation yields to the following:

$$\frac{\partial u_i^-}{\partial t^-} + u_i^-\frac{\partial u_j^-}{\partial x_j^-} = \frac{\eta}{\rho U_\tau H}\frac{\partial^2 u_i^-}{\partial x_i^{-2}} - \frac{\partial \mathcal{P}'^-}{\partial x_i^-} + \frac{\eta}{\rho U_\tau H}\mu\frac{\partial \phi}{\partial x_i} \qquad \text{whith} \qquad i,j = 1,2,3 \tag{2.32}$$

The non- dimensional groups have not been substituted yet, and the capillary stress is still in a partially dimensional form.

### 2.3.2 Dimensionless phase field equations

The phase field equations have been rewritten in a non-dimensional form using the equilibrium bulk concentration $\phi^*$ as the concentration-scale, the shear ve-

locity $U_\tau$ as the velocity-scale and the channel half height $H$ as the length-scale. The last two scaling parameters are reported in the previous section, whereas the concentration scale $\phi^*$ has been obtained from equation 2.5, and is following reported:

$$\phi^* = \sqrt{\frac{\beta}{\alpha}} \tag{2.33}$$

The dimensionless groups are similar to that used in Section 2.3.1 but the dimensionless order parameter has been added:

$$x^- = \frac{x}{H}, \qquad u^- = \frac{u}{U_\tau}, \qquad t^- = \frac{tU_\tau}{H}, \qquad \mathcal{P}'^- = \frac{\mathcal{P}'}{\frac{\rho U_\tau^2}{H}}, \qquad \phi^- = \frac{\phi}{\phi^*} \tag{2.34}$$

The non-dimensional groups above are substituted in to the chemical potential equation 2.25 and, remembering the definition of the mixing free energy magnitude reported in equation 2.7, the following equation is obtained, where the dimensionless parameters have not bee evidenced yet.

$$\frac{\mu}{\beta\left(\frac{\beta}{\alpha}\right)^{\frac{1}{2}}} = \phi^{-^3} - \phi^- - \frac{\xi^2}{H^2}\nabla^2\phi^- \tag{2.35}$$

Thus the chemical potential scale is obtained:

$$\mu^* = \beta\left(\frac{\beta}{\alpha}\right)^{\frac{1}{2}} \tag{2.36}$$

The shape of the dimensionless double well potential $f_0/\mu^*$ is shown in Figure 2.2 where also the dimensionless chemical potential $\mu/\mu^*$ is reported. The non dimensional Cahn Hilliard equation is obtained substituting equation 2.36 and the non dimensional variables in to equation 2.26, obtaining:

$$\frac{\partial\phi^-}{\partial t^-} + v_i^- \frac{\partial\phi^-}{\partial x_i^-} = \frac{M_c\beta}{U_\tau H}\frac{\partial}{\partial x_j^-}\left(\lambda\frac{\partial\mu^-}{\partial x_i^-}\right) \qquad \text{with} \qquad i,j = 1,2,3 \tag{2.37}$$

Where $\lambda$ is the dimensionless mobility; if the mobility is kept constant $\lambda = 1$, otherwise a constitutive law has to be introduced; to achieve this scope Badalassi *et al.*[4] suggested following dependance on to the order parameter, which is reported in Figure 2.3:

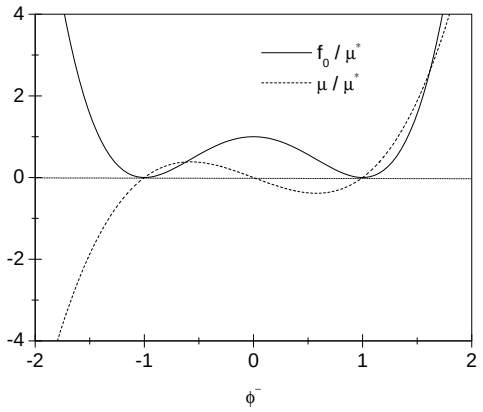


Figure 2.2: Non dimensional double well potential on the energy-concentration ($\frac{f_0}{\mu^*} - \phi^-$) diagram

$$M(\phi) = M_c\left(1-\gamma\phi^{-^2}\right) \rightarrow \lambda = \frac{M}{M_c} = \left(1-\gamma\phi^{-^2}\right) \tag{2.38}$$

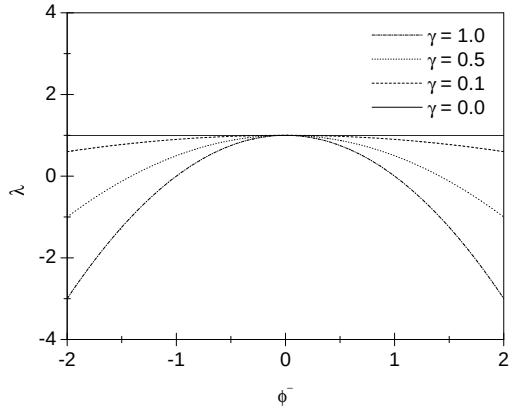


Figure 2.3: Dimensionless mobility on the mobility-concentration diagram ($\lambda - phi^-$) at different values of the diffusion parameter $\gamma$

A diffusion parameter $0 \leq \gamma \leq 1$ has been introduced in order to control the process dynamics, in fact if $\gamma \rightarrow 0$ the process is driven by the bulk diffusion (constant mobility), otherwise for $\gamma \rightarrow 1$ the dynamics is controlled by the interface diffusion. Introducing then the non-dimensional order parameter and the non-dimensional chemical potential in to equation 2.32, the dimensionless Navier-Stokes equation is obtained:

$$\frac{\partial u_i^-}{\partial t^-} + u_i^- \frac{\partial u_j^-}{\partial x_j^-} = \frac{\eta}{\rho U_\tau H} \frac{\partial^2 u_i^-}{\partial x_i^{-2}} - \frac{\partial \mathcal{P}'^-}{\partial x_i^-} + \frac{\beta}{\alpha} \frac{\eta\beta}{\rho U_\tau H} \mu^- \frac{\partial \phi^-}{\partial x_i^-} \tag{2.39}$$

### 2.3.3 Dimensionless parameters

To complete the scaling procedure, the Reynolds number, the Cahn number, the Capillary number and the Peclet number have to be introduced. These quantities are respectively written in the following way:

$$Re = \frac{\rho U_\tau H}{\eta}, \qquad Ch = \frac{\xi}{H}, \qquad Ca = \frac{\eta U_\tau}{\sigma}, \qquad Pe = \frac{H U_\tau}{M_c \beta}. \tag{2.40}$$

The Reynolds number is the ratio between the inertial forces, $\rho U_\tau H$ and the viscous forces $\eta$. High Reynolds number means the viscous effects are negligible with respect to the inertial effects, as in the turbulent flows; instead for low Reynolds number the flow is dominated by viscous effects as in the laminar flows. The Cahn number is the ration between the interface thickness parameter $\xi$ and the half hight of the channel $H$; it controls the surface thickness in relation to the channel characteristic length; for a plane interface, containing the 90% of the variation of the order parameter the surface thickness is $l = 4.164ChH$. The Capillary number is defined as the ratio between viscous forces at the interface, $\eta U_\tau$ and the surface tension at the interface, $\sigma$; high Capillary numbers means that the viscous stresses on the fluid are larger than interface stresses, hence the morphology of the system is modified by the flow field, on the other hand low Capillary number yields a system where the viscous stresses are negligible, thus the system morphology is almost independent from the flow field. The Peclet number is the ratio between the diffusive time-scale $H^2/M_c\beta$ and the convective time-scale $H/U_\tau$; high Peclet numbers are related to diffusion dominated phenomenon, on the other hand low Peclet numbers are related to systems were the dynamics are controlled by the convection.

### 2.3.4 Collection of non-dimensional equations

Substituting the non-dimensional parameters to the dimensionless equations reported above, the following formulation, in vectorial notation, is obtained:

$$\frac{\partial \mathbf{u}^-}{\partial t^-} = -\mathbf{u}^- \cdot \nabla \mathbf{u}^- - \nabla \cdot \mathcal{P}'^- + \frac{1}{Re}\nabla^2 \cdot \mathbf{u}^- + \frac{3}{2\sqrt{2}}\frac{1}{Ca}\frac{1}{Ch}\frac{1}{Re}\mu^- \nabla \cdot \phi^- \quad (2.41)$$

$$\nabla \cdot \mathbf{u}^- = 0 \quad (2.42)$$

$$\mu^- = \phi^{-^3} - \phi^- - Ch^2 \nabla^2 \phi^- \quad (2.43)$$

$$\frac{\partial \phi^-}{\partial t^-} = -\mathbf{u}^- \cdot \nabla \phi^- + \frac{1}{Pe}\nabla \cdot (\lambda \nabla \phi^-) \quad (2.44)$$

The concentration profile of a planar interface reported by equation 2.6, can be rewritten in the following way:

$$\phi^- = \tanh\left(\frac{z-}{\sqrt{2}Ch}\right) \quad (2.45)$$

The dependence of the interface thickness on the Cahn number is shown in Figure 2.4

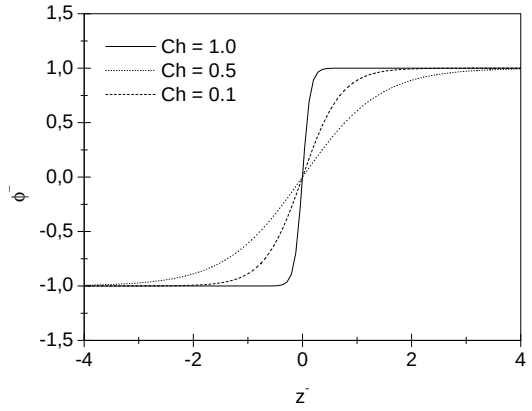


Figure 2.4: Non dimensional concentration profile across the planar interface ($\phi^- - z^-$) at different values of Cahn number $C_h$

### 2.3.5 The wall units

In fluid mechanics the non-dimensional results are usually reported using the so-called *wall-units* (which are indicated by a "+" apex), which refers to the

shear velocity $U_\tau$ as the velocity-scale, and to the cinematic viscosity $\nu$ of the fluid. In this way the scaling groups have the following form:

$$x^+ = \frac{xU_\tau}{\nu}, \qquad u^+ = \frac{u}{U_\tau}, \qquad t^+ = \frac{tU_\tau^2}{\nu}. \tag{2.46}$$

Substituting the definition of the outer-scaling variables (reported in the equations 2.30) in the wall-units scaling variables, the following transformation between the two systems is obtained:

$$\begin{aligned} x^- &= \frac{x}{H} = \frac{\nu}{U_\tau H} x^+ = \frac{x^+}{Re_\tau}, \\ u^+ &= \frac{u}{U_\tau} = u^-, \\ t^+ &= \frac{tU_\tau}{H} = \frac{\nu}{U_\tau^2 \frac{H}{U_\tau}} = \frac{t^+}{Re_\tau}. \end{aligned} \tag{2.47}$$

The concentration-scale variable do not depend on the fluid scaling variables, thus the dimensionless concentration parameter remains the same even if it is reported in a wall-units system:

$$\phi^- = \frac{\phi}{\phi^*} = \phi^+ \tag{2.48}$$

# Chapter 3

# Numerical model

Scope of this work is the implementation of the phase field model equations in an already existing Direct Numerical Simulation (DNS) code, which was developed for the solution of the incompressible Navier Stokes equations on a channel geometry; stating this, the diffuse interface equations have been reformulated to allow the use of the flow field solution scheme. In this chapter the numerical schemes which have been used are shown and applied on the equations reported in Chapter 2; in Section 3.1 the flow field spatial and temporal discretization is reported, giving some briefly notions on the solution procedure. In Section 3.2 the numerical implementation of the convective Cahn-Hilliard equation is reported, whereas in Section 3.3 the solution scheme of the diffiusion-advection equation is shown.

## 3.1 Solution of the equations of motion

The dimensionless momentum equation 2.41 is rewritten the following way, in which the "-" apex have been removed for brevity:

$$\frac{\partial \mathbf{u}}{\partial t} = \mathbf{S} + \frac{1}{Re_\tau}\nabla^2\mathbf{u} - \nabla p' \tag{3.1}$$

In the formulation above the corrected pressure term $\mathcal{P}'$ has been decomposed [1] in to the mean component $\bar{\mathcal{P}}'$ and the fluctuating component $p'$, where

[1] It was obtained imposing the well known Reynolds decomposition.

the latter yields to the $\partial p'/\partial x_i$ operator reported in the equation above. The mean pressure components, imposed to be 1 in the flow direction and zero in to the others, are collected in to the **S** vector which contains also the non-linear convective terms and the capillary stresses. Imposing the values above for the pressure terms, the flow is forced to move in the $x$ direction obtaining, with no-slip condition at the walls, the well known Poiselle flow. The scalar components of the **S** vector are following reported:

$$\begin{aligned} S_x &= -\frac{\partial(u_x u_j)}{\partial x_j} + \frac{3}{\sqrt{8}}\frac{1}{CaChRe_\tau}\cdot\mu\frac{\partial\phi}{\partial x} + 1 \\ S_y &= -\frac{\partial(u_y u_j)}{\partial x_j} + \frac{3}{\sqrt{8}}\frac{1}{CaChRe_\tau}\cdot\mu\frac{\partial\phi}{\partial y} \\ S_z &= -\frac{\partial(u_z u_j)}{\partial x_j} + \frac{3}{\sqrt{8}}\frac{1}{CaChRe_\tau}\cdot\mu\frac{\partial\phi}{\partial z} \end{aligned} \tag{3.2}$$

The solution of the equation system composed by the Navier-Stokes and continuity equations requires the imposition of the pressure boundary conditions which are difficult to determine; furthermore the pressure term is shown only in to the N-S equations and not in to the continuity equation, making the solution of the system non-trivial. For this reasons is convenient to rewrite the equation 3.1 without keeping explicitly in account the pressure term; this can be obtained taking the curl of the Navier-Stokes equation, as follows:

$$\nabla\times\frac{\partial\mathbf{u}}{\partial t} = \nabla\times\mathbf{S} + \frac{1}{Re_\tau}\nabla\times\nabla^2\cdot\mathbf{u} - \nabla\times\nabla p' \tag{3.3}$$

Substituting the vectorial identity $\nabla\times\nabla\cdot p' = 0$ and the vorticity vector definition $\bar{\omega} = \nabla\times\mathbf{u}$ in to the above equation, the following vorticity transport equation is obtained:

$$\frac{\partial\bar{\omega}}{\partial t} = \nabla\times\mathbf{S} + \frac{1}{Re_\tau}\nabla^2\bar{\omega} \tag{3.4}$$

Taking again the curl of equation 3.4:

$$\nabla\times\frac{\partial\bar{\omega}}{\partial t} = \nabla\times\nabla\times\mathbf{S} + \frac{1}{Re_\tau}\nabla\times\nabla^2\bar{\omega} \tag{3.5}$$

Substituting in to the equation above the vectorial identity $\nabla\times\nabla\times\mathbf{c} = \nabla(\nabla\cdot\mathbf{c}) - \nabla^2\mathbf{c}$ and the continuity equation for incompressible flows (eq. 2.42), the final formulation of the transport equation is obtained:

$$\frac{\partial \nabla \mathbf{u}}{\partial t} = \nabla^2 \mathbf{S} - \nabla(\nabla \cdot \mathbf{S}) + \frac{1}{Re_\tau}\nabla^4 \mathbf{u} \tag{3.6}$$

The solution algorithm implemented in the DNS code was the so called *normal-velocity normal vorticity* algorithm developed by Kim *et al.*[21]where equation 3.4 and equation 3.6 are projected on to the wall-direction and solved in order to obtain the normal component of the vorticity $\omega_z$ and velocity $u_z$; From the continuity equation and the vorticity definition, the other two velocity components are obtained. Hence the numerical aproximation of the Navier-Stokes equation require the solution of the following system of equations:

$$\begin{cases} \frac{\partial \bar{\omega}_z}{\partial t} = \frac{\partial S_y}{\partial x} - \frac{\partial S_x}{\partial y} + \frac{1}{Re_\tau}\nabla^2 \bar{\omega}_z \\ \frac{\partial (\nabla^2 u_z)}{\partial t} = \nabla^2 S_z - \frac{\partial}{\partial z}\frac{\partial S_j}{\partial x_j} + \frac{1}{Re_\tau}\nabla^4 u_z \\ \frac{\partial u_z}{\partial z} = -\frac{\partial u_x}{\partial x} - \frac{\partial u_y}{\partial y} \\ \bar{\omega}_z = \frac{\partial u_y}{\partial x} + \frac{\partial u_x}{\partial y} \end{cases} \tag{3.7}$$

The set of partial differential equations 3.7 are numerically solved by a code which uses a Chebyshev-Tau solution algorithm along the $z$ direction. The DNS code allows to simulate unsteady turbulent or laminar flows as well, without the introduction of sub-grid flows models, thus it gives the most precise approximation of the N-S equations solution.

### 3.1.1 Temporal discretization

To solve numerically in time the unsteady equations 3.7, a temporal discretization has to be introduced in order to approximate the time derivatives; to reach this target with high efficiency [6], an hybrid temporal discretization scheme, which computes explicitly the non-linear terms and implicitly the linear terms, was introduced. Because of the different treatment of the operators, it refers to the IMEX (IMplicit-EXplicit) class of temporal schemes (following the classification of Ascher *et al.*[3]) which are widely used for the solution of non-linear unsteady problems. The non-linear terms are computed explicitly by a second order Adams-Bashfort scheme, whereas the linear terms are treated implicitly by a Crank-Nicolson scheme. The former aproximate the variation in time of the variable $u$ known the value of $f(u)$ at time-steps $n$ and $n-1$, whereas the

latter, for the same calculation [2], needs the steps $n$ and $n+1$. Imposing a time step $\Delta t$, the IMEX scheme yields the following:

$$\frac{\phi^{n+1} - \phi^n}{\Delta t} = \frac{1}{2}\left(3S^n - S^{n-1}\right) + \frac{1}{2}\left(\psi^{n+1} + \psi^n\right) \tag{3.8}$$

Where $S$ are the non-linear terms and $\psi$ are the linear terms. Furthermore the first term on the RHS is given by the Adams-Bashfort scheme, whereas the second term is due to the Crank-Nicolson scheme.

### 3.1.2 Spatial discretization

The equations system 3.7 is solved via a pseudo spectral spatial discretization, which uses a Fourier collocation method along the two periodic directions of the channel and a Chebyshev collocation method on the wall direction. This different approach between the wall-normal direction and the spanwise and lengthwise directions is due to the absence of periodicity on the former, which is characterized by non-slip conditions at the walls [3]. The two periodic directions are treated with a Fast Fourier Transform algorithm considering their periodicity length of $L_x = 4\pi$ and $L_y = 2\pi$ and projecting the velocity vector on to $N_x$ and $N_y$ Fourier modes. This means that in the physical space the spatial discretization has an uniform grid along these directions and the spacing between two nodes is given by:

$$\Delta x = \frac{L_x}{N_x}, \qquad \Delta_y = \frac{L_y}{N_y}. \tag{3.9}$$

When a Fourier transformation is applied to a signal (i.e. the fluid velocity) it is decomposed in a sum of $N$ periodical functions characterized by their own wavenumber and amplitude; the former represents the frequency of the corresponding harmonic, whereas the latter is the magnitude of such harmonic. For each mode $n_x$ or $n_y$ in the $x$ and $y$ directions the wave-numbers can be written as:

[2] The apex $n$ and $n+1$ refer to the time step at which the function is calculated, with respect to the time step $n$ at which the derivative is approximated

[3] If the shear flow is simulated, the normal-wall direction is still non periodic because of the imposed velocity at the walls.

$$k_x = \frac{2\pi n_x}{L_x}, \qquad k_y = \frac{2\pi n_y}{L_y}. \tag{3.10}$$

A generical signal, projected in to the Fourier space along $x$ and $y$, can be represented by the following sum of harmonics:

$$u_i(\mathbf{x}, t) = \sum_{n_x=-\frac{N_x}{2}+1}^{\frac{1}{2}N_x} \sum_{n_y=-\frac{N_y}{2}+1}^{\frac{1}{2}N_y} \hat{u}_i(k_x, k_y, z, t) e^{j(k_x x + k_y y)} \tag{3.11}$$

Where $j$ represent the imaginary unit of the complex representation and $\hat{u}_i$ is the Fourier coefficient of the velocity in the modal coordinates $(n_x, n_y)$ that still depends on the $z$ physical coordinate. The velocity signal, reported by equation 3.11, is then projected on the Chebyshev polynoms space along the $z$ direction using the following definition:

$$T_{n,z}(z) = \cos\left[n_z \arccos(z)\right] \tag{3.12}$$

Where $n_z$ is one of the $N_z$ Chebyshev modes and $z = z^-$ is the dimensionless length variable which is comprised in $-1 \leq z \leq 1$ interval. Stating the definition above, the grid points coordinates are given by the following mapping definition:

$$z = \cos\left(\frac{n_z \pi}{N_z}\right) \tag{3.13}$$

The Chebychev collocation method is characterized by an high spatial resolution near the walls ($z = \pm 1$), where the velocity gradients are expectyed to be higher than in the other points of the domain. Substituting the equation 3.12 in to equation 3.11, the following expression for the $i$ velocity component projected on the $(k_x, k_y, n_z)$ modal space is obtained:

$$u_i(\mathbf{x}, t) = \sum_{n_x=-\frac{N_x}{2}+1}^{\frac{1}{2}N_x} \sum_{n_y=-\frac{N_y}{2}+1}^{\frac{1}{2}N_y} \sum_{n_z=0}^{N_z} \hat{u}_i(k_x, k_y, n_z, t) T_{n,z}(z) e^{j(k_x x + k_y y)} \tag{3.14}$$

The modal projection method described above is applied not only to the velocity components, but also to the other variables treated by the code. One of the most important properties of the Fourier space, is that the spatial derivative of a variable transformed in to the modal space, can be taken by a wavenumber multiplication. From the discrete Fourier series theory, the following identities

can be obtained (where, as reported in equation 3.14, the "hat" indicates a variable in the Fourier space):

$$\begin{aligned} \widehat{\frac{\partial u_i(\mathbf{x},t)}{\partial x_k}} &= jk_k\hat{u}_i(k_x,k_y,n_z,t), \\ \widehat{\frac{\partial^2 u_i(\mathbf{x},t)}{\partial x_k^2}} &= (jk_k)(jk_k)\hat{u}_i(k_x,k_y,n_z,t) \\ &= -k_k^2\hat{u}_i(k_x,k_y,n_z,t). \end{aligned} \tag{3.15}$$

Where in to the equation above the $j \cdot j = -$ identity has been substituted. The identities reported in equation 3.15 hold only for the two fourier directions $k = x$, $k = y$ and not for the Chebyshev directions $k = z$, where a recursive formula is applied to calculate the derivative. The procedure shown in Section 3.1 can be applied on to the spatial discretized equations, starting from equation 3.1 expanded in its scalar components and rewritten in the modal space $(k_x, k_y, n_z)$:

$$\begin{aligned} \frac{\partial \hat{u}_x}{\partial t} &= \hat{S}_x + \frac{1}{Re_\tau}\left(\frac{\partial^2}{\partial z^2} - \mathbf{k}\right)\hat{u}_x - jk_x\hat{p'} \\ \frac{\partial \hat{u}_y}{\partial t} &= \hat{S}_y + \frac{1}{Re_\tau}\left(\frac{\partial^2}{\partial z^2} - \mathbf{k}\right)\hat{u}_y - jk_y\hat{p'} \\ \frac{\partial \hat{u}_z}{\partial t} &= \hat{S}_z + \frac{1}{Re_\tau}\left(\frac{\partial^2}{\partial z^2} - \mathbf{k}\right)\hat{u}_z - \frac{\partial}{\partial z}\hat{p'} \end{aligned} \tag{3.16}$$

Where $\mathbf{k} = k_x^2 + k_y^2$. The equation above stresses that the $z$ derivatives are taken in a different way, due to the Chebyshev collocation method. Applying the temporal discretization described in Section 3.1.1, the scalar components read:

$$\begin{aligned} \frac{\hat{u}_x^{n+1} - \hat{u}_x^n}{\Delta t} &= \frac{1}{2}\left(3\hat{S}_x^n - \hat{S}_x^{n-1}\right) + \frac{1}{2Re_\tau}\left(3\hat{\psi}_x^n + \hat{\psi}_x^{n+1}\right) \\ \frac{\hat{u}_y^{n+1} - \hat{u}_y^n}{\Delta t} &= \frac{1}{2}\left(3\hat{S}_y^n - \hat{S}_y^{n-1}\right) + \frac{1}{2Re_\tau}\left(3\hat{\psi}_y^n + \hat{\psi}_y^{n+1}\right) \\ \frac{\hat{u}_x^{n+1} - \hat{u}_x^n}{\Delta t} &= \frac{1}{2}\left(3\hat{S}_z^n - \hat{S}_z^{n-1}\right) + \frac{1}{2Re_\tau}\left(3\hat{\psi}_z^n + \hat{\psi}_z^{n+1}\right) \end{aligned} \tag{3.17}$$

Where:

$$\begin{aligned}
\hat{\psi}_x &= \left(\frac{\partial^2}{\partial z^2} - \mathbf{k}\right)\hat{u}_x - jk_x\hat{p}' \\
\hat{\psi}_y &= \left(\frac{\partial^2}{\partial z^2} - \mathbf{k}\right)\hat{u}_y - jk_y\hat{p}' \\
\hat{\psi}_z &= \left(\frac{\partial^2}{\partial z^2} - \mathbf{k}\right)\hat{u}_z - \frac{\partial}{\partial z}\hat{p}'
\end{aligned} \tag{3.18}$$

The equations above can be rewritten in the following way:

$$\begin{aligned}
\left(\frac{\partial^2}{\partial z^2} - \frac{1+\gamma\mathbf{k}}{\gamma}\right)\hat{u}_x^{n+1} &= \frac{\left(jk_x\Delta t\hat{p}'^{n+1} - \hat{H}_x\right)}{\gamma} \\
\left(\frac{\partial^2}{\partial z^2} - \frac{1+\gamma\mathbf{k}}{\gamma}\right)\hat{u}_y^{n+1} &= \frac{\left(jk_y\Delta t\hat{p}'^{n+1} - \hat{H}_y\right)}{\gamma} \\
\left(\frac{\partial^2}{\partial z^2} - \frac{1+\gamma\mathbf{k}}{\gamma}\right)\hat{u}_x^{n+1} &= \frac{\left(\frac{\partial}{\partial x}\Delta t\hat{p}'^{n+1} - \hat{H}_z\right)}{\gamma}
\end{aligned} \tag{3.19}$$

Where $\gamma = \frac{\Delta t}{2Re_\tau}$ an the $\hat{H}_i$ terms are described by the following:

$$\begin{aligned}
\hat{H}_x &= \Delta t\tilde{S}x + \left(\gamma\frac{\partial^2}{\partial z^2} + 1 - \gamma\mathbf{k}\right)\hat{u}_x^n \\
\hat{H}_y &= \Delta t\tilde{S}y + \left(\gamma\frac{\partial^2}{\partial z^2} + 1 - \gamma\mathbf{k}\right)\hat{u}_y^n \\
\hat{H}_z &= \Delta t\tilde{S}z + \left(\gamma\frac{\partial^2}{\partial z^2} + 1 - \gamma\mathbf{k}\right)\hat{u}_z^n
\end{aligned} \tag{3.20}$$

The $\tilde{S}_i$ terms are the non-linear parts calculated with the Adams-Bashfort algorithm and, defining $\beta^2 = \frac{1+\gamma\mathbf{k}}{\gamma}$, the following formulation is obtained:

$$\begin{aligned}
\left(\frac{\partial^2}{\partial z^2} - \beta^2\right)\hat{u}_x^{n+1} &= \frac{\left(jk_x\Delta t\hat{p}'^{n+1} - \hat{H}_x\right)}{\gamma} \\
\left(\frac{\partial^2}{\partial z^2} - \beta^2\right)\hat{u}_y^{n+1} &= \frac{\left(jk_y\Delta t\hat{p}'^{n+1} - \hat{H}_y\right)}{\gamma} \\
\left(\frac{\partial^2}{\partial z^2} - \beta^2\right)\hat{u}_x^{n+1} &= \frac{\left(\frac{\partial}{\partial x}\Delta t\hat{p}'^{n+1} - \hat{H}_z\right)}{\gamma}
\end{aligned} \tag{3.21}$$

Following the procedure shown in Section 3.1, the curl of equation 3.21 is taken twice, obtaining first the vorticity transport equation and then the final formulation of the velocity transport equation:

$$\begin{cases} \left(\frac{\partial^2}{\partial z^2} - \beta^2\right)\hat{\omega}_z^{n+1} = -\frac{\left(jk_x H_y - jk_y \hat{H}_x\right)}{\gamma} \\ \left(\frac{\partial^2}{\partial z^2} - \beta^2\right)\left(\frac{\partial^2}{\partial z^2} - \mathbf{k}\right)\hat{u}_z^{n+1} = \frac{1}{\gamma}\left[\frac{\partial}{\partial z}\left(jk_x\hat{H}_x + jk_y\hat{H}_y\right) + \mathbf{k}\hat{H}_z\right] \\ \frac{\partial}{\partial z}\hat{u}_z^{n+1} = -jk_x\hat{u}_x^{n+1} - jk_y\hat{u}_y^{n+1} \\ \hat{\omega}_z^{n+1} = -jk_y\hat{u}_x^{n+1} + jk_x\hat{u}_y^{n+1} \end{cases} \tag{3.22}$$

Where the last two equations are respectively the discretized continuity equation and the discretized vorticity definition.

### 3.1.3 Equations solution

The first two equations of the system 3.22 are non-linear because of the presence of the $z$ direction derivative, hence the system obtained is non-linear and cannot be solved directly. Stating this both the equations have been rewritten in the form of an Helmholtz equation which has a known approximate solution; after the solution the equations system becomes linear and is possible to solve it directly. The Helmholtz equation general form is the following:

$$\frac{\mathrm{d}^2\xi}{\mathrm{d}z^2} - \alpha^2\xi = \varsigma \tag{3.23}$$

Where $\xi = \xi(z)$ is a scalar function of $z$ and $\alpha$ and $\varsigma$ are constants. The first equation of the system 3.22 has already the form of the Helmholtz equation and it is solved imposing the following boundary conditions:

$$\begin{cases} \hat{\omega}_z(-1) = 0 \\ \hat{\omega}_z(1) = 0 \end{cases} \tag{3.24}$$

The second equation of the system 3.22 can be rewritten as a system of two Helmholtz equations:

$$\begin{cases} \left(\frac{\partial^2}{\partial z^2} - \mathbf{k}\right)\hat{u}_z^{n+1} = \hat{\theta} \\ \left(\frac{\partial^2}{\partial z^2} - \beta^2\right)\hat{\theta} = \frac{1}{\gamma}\left[\frac{\partial}{\partial z}\left(jk_x\hat{H}_x + jk_y\hat{H}_y\right) + \mathbf{k}\hat{H}_z\right] \end{cases} \tag{3.25}$$

The system is solved imposing the following boundary conditions on at the walls:

$$\begin{cases} P_1\hat{u}_z(\pm 1) + Q_1\frac{\mathrm{d}\hat{u}_z(\pm 1)}{\mathrm{d}z} = R_1 \\ \hat{\theta}(\pm 1) = \hat{\theta}_1 + \hat{A}\hat{\theta}_2 + \hat{B}\theta_3 \end{cases} \tag{3.26}$$

The $\hat{\theta}$ boundary conditions are not immediately given by the problem, hence they have to be determined imposing the following conditions at the walls:

$$\begin{cases} \hat{\theta}_1(\pm 1) = 0 \\ \theta_2(1) = \theta_3(-1) = 0 \\ \theta_2(-1) = \theta_3 1 = 0 \end{cases} \tag{3.27}$$

## 3.2 Solution of the phase field equations

Since the solution scheme for the phase field equations has been chosen to be similar to the flow field solution algorithm, also the Cahn-Hilliard equation has to be discretized in space and time, and then rewritten in the Helmholtz equation form. The phase field equation 2.44 (where the "-" apex have been omitted for sake of brevity) is following reported:

$$\frac{\partial \phi}{\partial t} = -\mathbf{u} \cdot \nabla \phi + \frac{1}{Pe} \nabla \cdot (\lambda \nabla \mu) \tag{3.28}$$

Expanding the gradient terms, the following equation is obtained:

$$\frac{\partial \phi}{\partial t} = -\mathbf{u} \cdot \nabla \phi + \frac{1}{Pe} \nabla \left(1 - \gamma \phi^2\right) \left(\nabla \phi^3 - \nabla \phi - Ch^2 \nabla \cdot \nabla^2 \phi\right) \tag{3.29}$$

Applying the composite derivative rule to the concentration dependent mobility $\lambda = \lambda(\phi)$, the equation above yields to:

$$\begin{aligned} \frac{\partial \phi}{\partial t} = & - \mathbf{u} \cdot \nabla \phi + \frac{1}{Pe} \left(\nabla \lambda \cdot \nabla \phi^3 + \lambda \nabla^2 \phi^3 - \nabla \lambda \cdot \nabla \phi + \lambda \nabla^2 \phi\right) \\ & - \frac{Ch^2}{Pe} \left(\nabla \lambda \cdot \left(\nabla \cdot \nabla^2 \phi\right) + \lambda \nabla^2 \cdot \nabla^2 \phi\right) \end{aligned} \tag{3.30}$$

Where, as reported in Section 2.3.2:

$$\lambda = 1 - \gamma \phi^2 \tag{3.31}$$

The equation above can be rewritten collecting the linear diffusive terms in to $S_c$ and the non linear convective terms in to $\psi_c$, in this way is possible to apply a IMEX temporal scheme:

$$\frac{\partial \phi}{\partial t} = S_c + \psi_c \tag{3.32}$$

The application of a IMEX scheme to a PDE (Partial Differential Equation) with fourth order derivative terms, require to compute the higher order terms explicitly (see Lamorgese *et al.*[23]) in order to apply two set of boundary conditions; in this way the problem is mathematically well posed. To achieve this with the solution algorithm used for the flow field equations, the equation 3.32 has to been be split in two Helmholtz equations. Following Baldalassi *et al.*[4], Yue *et al.*[39] and Lamorgese *et al.*[23] the Helmholtz formulation is obtained expanding diffusive $\nabla^2\phi$ and hyper-diffusive $\nabla^2 \cdot \nabla^2\phi$ operators in the following way:

$$\begin{aligned} \nabla^2\phi &= 2\nabla^2\phi - 2\nabla^2\phi + \lambda\nabla^2\phi \\ \lambda\nabla^2 \cdot \nabla^2\phi &= \left(\frac{\Delta t}{2Pe} + \lambda - \frac{\Delta t}{2Pe}\right)\nabla^2 \cdot \nabla^2\phi \end{aligned} \tag{3.33}$$

The non linear operator $S_c$ yields the following:

$$\begin{aligned} S_C = &- \mathbf{u}\cdot\nabla\phi + \frac{1}{Pe}\left[\nabla\lambda\cdot\nabla\phi^3 + \lambda\nabla^2\phi^3 - \nabla\lambda\cdot\nabla\phi - (\lambda+2)\nabla^2\phi\right] \\ &- \frac{Ch^2}{Pe}\left[\nabla\lambda\left(\nabla\cdot\nabla^2\phi\right) + \left(\frac{\Delta t}{2Pe} - \lambda\right)\lambda\nabla^2\cdot\nabla^2\phi\right] \end{aligned} \tag{3.34}$$

Whereas the linear operator $\psi_c$ reads:

$$\psi_C = -\frac{2}{Pe}\nabla^2\phi + \frac{\Delta t}{2Pe^2}\nabla^2\cdot\nabla^2\phi \tag{3.35}$$

In this way the formulation will allow to split the single PDE in a system of two Helmhotz equations.

### 3.2.1 Temporal discretization

The same IMEX numerical scheme reported in Section 3.1.1 for the flow field equations, is now applied to the Cahn-Hilliard equation:

$$\frac{\phi^{n+1} - \phi^n}{\Delta t} = \frac{1}{2}\left(3S_c^n - S_c^{n-1}\right) + \frac{1}{2}\left(\psi_c^{n+1} + \psi_c^n\right) \tag{3.36}$$

Where first term on the RHS is obtained from the second order Adams-Bashfort scheme whereas the second terme is due to the application of the Cranck-Nichols temporal advancement scheme.

### 3.2.2 Spatial discretization

In accordance with the spatial discretization of the flow field equations, also the Cahn-Hilliard equation is discretized using a pseudo-spectral algorithm. Thus the equation 3.36, projected on the $(k_x, k_y, n_z)$ modal space assumes the following form:

$$\frac{\hat{\phi}^{n+1} - \hat{\phi}^n}{\Delta t} = \frac{1}{2}\left(3\hat{S}_c^n - \hat{S}_c^{n-1}\right) + \frac{1}{2}\left(\hat{\psi}_c^{n+1} + \hat{\psi}_c^n\right) \tag{3.37}$$

Where:

$$\hat{\psi}^{n+1} + \hat{\psi}^n = \frac{1}{Pe}\left[2\left(\frac{\partial^2}{\partial z^2} - \mathbf{k}\right) - \frac{\Delta t}{2Pe}\left(\frac{\partial^2}{\partial z^2} - \mathbf{k}\right)\left(\frac{\partial^2}{\partial z^2} - \mathbf{k}\right)\right]\left(\hat{\phi}^{n+1} + \hat{\phi}^n\right) \tag{3.38}$$

All the terms at time $n+1$ are collected on the LHS of the equation:

$$\left[1 - \frac{\Delta t}{Pe}\left(\frac{\partial^2}{\partial z^2} - \mathbf{k}\right) + \frac{\Delta t^2}{4Pe^2}\left(\frac{\partial^2}{\partial z^2} - \mathbf{k}\right)\left(\frac{\partial^2}{\partial z^2} - \mathbf{k}\right)\right]\hat{\phi}^{n+1} = \hat{H}_c \tag{3.39}$$

The $H_c$ term, which collects all the terms calculated explicitly at time $n$, is described by the following:

$$\hat{H}_c = \frac{\Delta}{2}\left(3\hat{S}_c^n - \hat{S}_c^{n-1}\right) + \frac{\Delta t}{2Pe}\left[\left(\frac{\partial^2}{\partial z^2} - \mathbf{k}\right) - \frac{\Delta t}{2Pe}\left(\frac{\partial^2}{\partial z^2} - \mathbf{k}\right)^2\right] \tag{3.40}$$

Defining $\gamma = \frac{\Delta t}{2Pe}$, equation 3.41 yields:

$$\left[\frac{1}{\gamma} - \left(\frac{\partial^2}{\partial z^2} - \mathbf{k}\right) + \left(\frac{\partial^2}{\partial z^2} - \mathbf{k}\right) + \gamma\left(\frac{\partial^2}{\partial z^2} - \mathbf{k}\right)\left(\frac{\partial^2}{\partial z^2} - \mathbf{k}\right)\right]\hat{\phi}^{n+1} = \frac{\hat{H}_c}{\gamma} \tag{3.41}$$

The following quantity is evidenced in to the equation above:

$$\hat{\theta} = \left(\frac{\partial^2}{\partial z^2} - \mathbf{k} - \frac{1}{\gamma}\right)\hat{\phi}^{n+1} \tag{3.42}$$

Hence it yields the following:

$$\begin{aligned} \frac{\hat{H}_c}{\gamma} &= \left[\frac{1}{\gamma} - \left(\frac{\partial^2}{\partial z^2} - \mathbf{k}\right) + \gamma\left(\frac{\partial^2}{\partial z^2} - \mathbf{k}\right)\hat{\theta}\right]\hat{\phi}^{n+1} \\ &= \left[-\hat{\theta} + \gamma\left(\frac{\partial^2}{\partial z^2} - \mathbf{k}\right)\hat{\theta}\right]\hat{\phi}^{n+1} \end{aligned} \tag{3.43}$$

Defining $\beta^2 = \frac{\gamma \mathbf{k}+1}{\gamma}$, the following system of two Helmhotz equations is obtained:

$$\begin{cases} \left(\frac{\partial^2}{\partial z^2} - \beta^2\right)\hat{\theta} = \frac{\hat{H}_c}{\gamma^2} \\ \left(\frac{\partial^2}{\partial z^2} - \beta^2\right)\hat{\phi}^{n+1} = \hat{\theta} \end{cases} \tag{3.44}$$

Following Lamorgese *et al.*[23], Yue *et al.*[39] the equation system above has been solved imposing a couple of boundary conditions for the concentration flux $\mathbf{n} \cdot \nabla\hat{\phi}$ and for the flux of the concentration laplacian $\mathbf{n} \cdot \nabla \cdot \nabla^2\hat{\phi}$ at the walls (where $\mathbf{n}$ denotes the normal vector to the wall). For simplicity only the zero-normal flux has been superposed and, stating that in $z$ direction $\hat{\theta} = \mathrm{d}\hat{\phi}/\mathrm{d}z$, the second boundary condition is equivalent to impose $\mathrm{d}\hat{\theta}/\mathrm{d}z = 0$; hence the following equations are obtained:

$$\begin{cases} \frac{\mathrm{d}\hat{\phi}(\pm 1)}{\mathrm{d}z} = 0 \\ \frac{\mathrm{d}\hat{\theta}(\pm 1)}{\mathrm{d}z} = 0 \end{cases} \tag{3.45}$$

## 3.3 Solution of the diffusion-advection equation

In order to ensure that the Helmholtz equation solver, rewritten to solve the scalar phase field, gives the expected results, a simple implementation of the unsteady diffusion-advection has been made. This equation can be solved analytically and computationally in several cases which can be easily used as benchmarks, furthermore it has the form of a simplified Cahn-hilliard equation, thus its implementation does not need a deep modification of the phase field code. The pure diffusion-advection equation reads:

$$\frac{\partial \phi}{\partial t} = -\mathbf{u} \cdot \nabla\phi + \frac{1}{Pe}\nabla^2\phi \tag{3.46}$$

Where the non linear $S_c$ terms and the linear $\psi_c$ operators have the following form:

$$S_c = -\mathbf{u} \cdot \nabla\phi, \qquad \psi_c = \frac{1}{Pe}\nabla^2\phi \tag{3.47}$$

In this case the equation has only a diffusive term $\nabla^2\phi$, hence it does not need to be split in two Helmhotz equations and thus the single solver can be

tested. The equation is discretized in time and space following the procedure reported in Section 3.2.1 and Section 3.2.2, obtaining the following formulation:

$$\frac{\hat{\phi}^{n+1}-\hat{\phi}^{n}}{\Delta t}=\frac{1}{2}\left(3\hat{S}_c^{n}-\hat{S}_c^{n-1}\right)+\frac{1}{2}\left(\hat{\psi}_c^{n+1}+\hat{\psi}_c^{n}\right) \tag{3.48}$$

Collecting all the terms calculated at time $n+1$ in the LHS, the following equation is obtained:

$$\left[1-\gamma\left(\frac{\partial^2}{\partial z^2}-\mathbf{k}\right)\right]=\hat{H} \tag{3.49}$$

Where $\gamma=\frac{\Delta t}{2Pe}$ and all the operators computed a time $n$ are collected in the $\hat{H}$ term which reads:

$$\hat{H}=\hat{\phi}^{n}+\frac{\Delta t}{2}\left(3\hat{S}_c^{n}-\hat{S}_c^{n-1}\right)+\gamma\left(\frac{\partial^2}{\partial z^2}-\mathbf{k}\right)\hat{\phi}^{n} \tag{3.50}$$

Thus the associated Helmholtz equation is the following:

$$\left(\frac{\partial^2}{\partial z^2}-\beta^2\right)\hat{\phi}^{n+1}=\hat{\theta} \tag{3.51}$$

Where $\beta^2=\frac{\gamma\mathbf{k}+1}{\gamma}$. Equation 3.51 can be solved either with Dirichlet or Neumann boundary conditions.

## 3.4 The computational algorithm

The numerical scheme shown above has been implemented in an already existing DNS code; the algorithm flow diagram is reported in Figure 3.1 where the links between flow field and phase field, in order to obtain the two way coupling, are reported. As reported in Section 3.1 the code uses a pseudo-spectral spatial discretization, this means that the multiplications between the velocity (or concentration) components are taken in the physical space. Hence a backward transformation is first applied on to the components, then the products are formed and finally the result is transformed in to the modal space. This apparently complicate procedure allows to reduce the number of calculations from $N^6$ required from the modal space convolution to $N^3\ln N$ operations (see Pope [30]), where $N$ is the number of Fourier modes. Due to the presence of products

taken in to the physical space, the computational algorithm needs some de-aliasing filters, both on the Fourier and the Chebyshev modes; following Boyd [6] a well compromise was founded on the application of the "2/3 rule" which suggests to keep only the first two thirds of the modes after the application of the pseudo-spectral procedure.

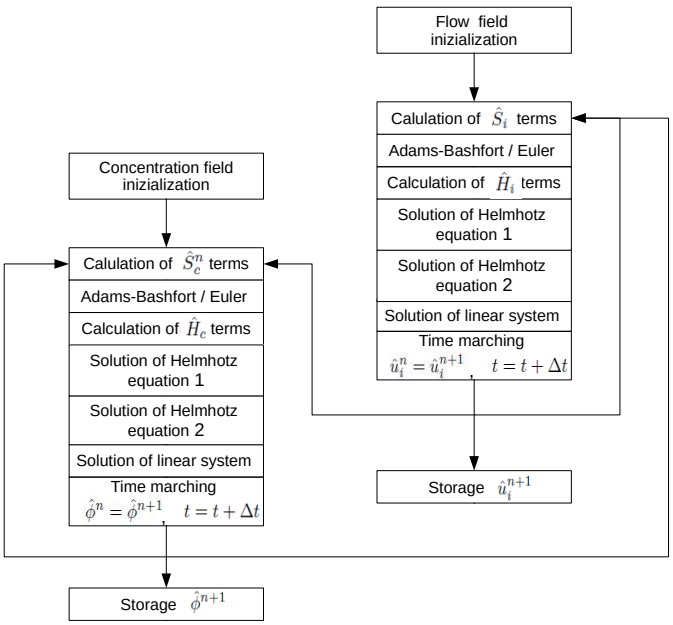


Figure 3.1: Flux diagram of the phase field-flow field solution algorithm

# Chapter 4

# Benchmarks

The governing equation of the phase-field model, due to the presence of an hyper-diffusive term, has a non trivial numerical solution, thus it required several benchmarks to validate the numerical implementation. A briefly report of the benchmarks results and also the numerical limitations founded is shown in the present chapter; particularly in Section 4.1 the solution of the pure diffusion equation is reported, in order to check the Helmholtz equation solver with several boundary conditions and initial fields. In Section 4.2 the Cahn-hilliard equation is modified in order to obtain a "fourth order" diffusion equation, to test the double-Helmholtz equation. All the simulations reported in this section have been performed fixing $Re_\tau = 10$ which generates a domain of $0 \leq z^+ \leq 20$ in the wall direction, $0 \leq y^+ \leq 60$ and $0 \leq x^+ \leq 120$ in the spanwise and lengthwise directions respectively.

## 4.1 Diffusion equation

The Cahn-Hilliard equation has been simplified in order to obtain the pure diffusion equation which is described, in dimensionless[1] variables, by the following:

$$\frac{\partial \phi}{\partial t} = \frac{1}{Pe} \nabla^2 \phi \tag{4.1}$$

[1] Through this chapter all the quatities considered are expressed in wall units, thus, for sake of brevity, the "+" apex has been neglected.

It describes the pure diffusion of a chemical specie in to another where the process is driven by the concentration gradients. The analytical solution of the equation above is well-known for simple geometries with different boundary conditions and initial concentration fields. To test the accurancy of the single-Helmholtz solver, a set of different initial concentration fields and BC have been used, in order to reproduce the results available in literature. In this case the equation is purely diffusive because the convective terms have been neglected; in spite of it the Reynolds number has to be chosen in order to define the domain dimensions. The equation 4.1 has been implemented with the numerical algorithm reported in Section 3.3, where the linear and non-linear terms are the following:

$$\begin{aligned} S_c &= 0, \\ \psi_c &= \frac{1}{Pe}\nabla^2\phi. \end{aligned} \tag{4.2}$$

The solution scheme obtained is a pure Crank-Nicolson implicit scheme.

### 4.1.1 Dirichlet boundary conditions

For the case under investigation, the concentration at the walls is kept constant obtaining the Dirichlet boundary conditions, which read:

$$\begin{cases} \phi\,(z=0) &= \phi_1 \\ \phi\,(z=20) &= \phi_2 \end{cases} \tag{4.3}$$

The initial value of the concentration field has been chosen to be $\phi_0 = 0$, whereas the fixed values at the walls are respectively $\phi_1 = 1$ and $\phi_2 = 0$. Applying the boundary conditions of equation 4.3 and a zero initial field, the pure diffusion equation 4.1 yields to the following analytical solution, which is the solution of the well-known Blasius problem (see Soldati [34]):

$$\phi = \phi_1 \left[1 - \mathrm{erf}\left(\frac{z}{2\sqrt{tRe}}Pe\right)\right] \tag{4.4}$$

Where $\mathrm{erf}(z,t)$ is the error function. In Table 4.1, the simulation parameters are collected:

| **Grid nodes** | **Pe** | $\Delta t$ |
|---|---|---|
| $64 \times 64 \times 65$ | 0.01 | $10^{-3}$ |
| $64 \times 64 \times 65$ | 0.10 | $10^{-3}$ |
| $64 \times 64 \times 65$ | 1.00 | $10^{-3}$ |
| $64 \times 64 \times 65$ | 10.0 | $10^{-3}$ |
| $64 \times 64 \times 65$ | 100 | $10^{-3}$ |
| $64 \times 64 \times 65$ | 1000 | $10^{-3}$ |

Table 4.1: Diffusion equation simulation parameters: Dirichlet boundary conditions

The numerical results, at different Peclet numbers are reported in Figure 4.2, whereas the comparison with the the analytical solution of equation 4.3 is reported in Figure 4.3. From the latter figure is possible to observe that the numerical results match the analytical results, and no detriment of the solution accuracy is founded varying the Peclet number. Since the Cahn-Hilliard equation requires no-flux BC to be solved, no other testes have been performed imposing the Dirichlet boundary conditions.

### 4.1.2 Neumann boundary conditions

A condition on the concentration flux at the walls have been imposed obtaining the Neumann boundary conditions; in particular a constant normal flux at the wall has been imposed:

$$\mathbf{n} \cdot \nabla \phi = 0 \rightarrow \frac{\partial \phi}{\partial z} = 0 \tag{4.5}$$

Following Young *et al.*[38], the mono-dimensional diffusion equation admit an analytical solution for the analytical initial concentration profile reported below:

$$\phi = \phi_0 \cos(\pi z) \tag{4.6}$$

Where $\phi_0 = 1$. The analytical solution of equation 4.5, reads:

$$\phi(z) = \phi_0 \cos(\pi z) \exp\left[-\frac{\pi^2}{PeRe} t\right] \tag{4.7}$$

Then the mono-dimensional diffusion equation has been solved imposing a ribbed-like initial concentration field along $z$:

$$\begin{cases} \phi = \phi_1 & \text{if} \quad 0 \leq z < 9 \quad \text{and} \quad 11 < z \leq 20 \\ \phi = \phi_2 & \text{if} \quad 9 \leq z \leq 11 \end{cases} \tag{4.8}$$

Where $\phi_1 = 0$ and $\phi_2 = 1$. In order to check the implementation of the equation also along the two periodic directions, the bi-dimensional diffusion equation have been solved on the $x - y$ planes. Following Young *et al.*[38], the two dimensional diffusion equation, coupled with the BC reported in to equation 4.5, admits an analytical solution if the initial concentration field reported below is imposed:

$$\phi = \phi_0 \left[ \sin\left(\pi \frac{x}{2}\right) + \sin(\pi y) \right] \tag{4.9}$$

Where $\phi_0 = 1$. For sake of simplicity in to the field initialization, the argument of the sinusoidal function along the $x$ direction (which as a periodicity length double with respect to the $y$ direction) has been divided by 2, thus the analytical solution yields to the following:

$$\phi(x, y) = \phi_0 \left[ \sin\left(\pi \frac{x}{2}\right) + \sin(\pi y) \right] \exp\left[ -\frac{\pi^2}{PeRe} t \right] \tag{4.10}$$

Since the directions are periodic, the BC conditions are already included by the espatial discretization, hence the results are expected to not completely match the analytical results. Finally the solution of the diffusion equation has been tested introducing a pseudo-random noise along all the directions, in order to check if the algorithm is sensitive to this kind of peturbations. This test has been retained necessary because the starting condition of the phase-separation simulations is usually a random noise superposed to a constant field in a meta-stable region. Again, as reported above, for simplicity the random noise have been introduced with the same periodicity along the two periodic directions. In Table 4.2 the simulation parameters have been summarized, whereas in Figure 4.4 the comparison between the numerical results and the analytical solution (eq. 4.7) has been reported. In Figure 4.5 the results given by the ribbed-like initial field (eq. 4.8) are reported, whereas Figure 4.6 shows the confrontation between the analytical and the numerical solution of the bi-dimensional diffusion

equation. At the end in Figure 4.7 the numerical results obtained from the solution of the three dimensional diffusion equation with initial random field are reported.

| **Grid nodes** | **Pe** | $\Delta t$ |
|---|---|---|
| $64 \times 64 \times 65$ | 0.01 | $10^{-4}$ |
| $64 \times 64 \times 65$ | 0.10 | $10^{-4}$ |
| $64 \times 64 \times 65$ | 1.00 | $10^{-3}$ |
| $64 \times 64 \times 65$ | 10.0 | $10^{-3}$ |
| $64 \times 64 \times 65$ | 100 | $10^{-3}$ |
| $64 \times 64 \times 65$ | 1000 | $10^{-3}$ |

Table 4.2: Diffusion equation simulation parameters: Neumann boundary conditions

From Figure 4.4 is possible to appreciate that also in this case the numerical solution matches the analytical solution, but the time step $\Delta t$ has to be reduced in order to obtain the properly accuracy for the lowest Peclet number ($Pe = 0.01$). The solution of the ribbed-like initial profile, reported in Figure 4.5, shows the expected behavior, that is a more rapid smooth of the rib the lower is the Peclet number. Also in this case the $\Delta t$ has to be reduced in order to obtain the expected accuracy for the most rapid diffusion processes ($Pe = 0.01$ and $Pe = 0.1$), whereas the initial oscillations due to the spectral representation of a sharp profile are rapidly damped. Some oscillations are also obtained at the proximity of the walls, where the boundary conditions ar imposed; this is due to the imposition of only the flux and not of the boundary value too, thus the algorithm has to fit by itself the properly value. The tests performed on the two dimensional diffusion equation (Figure 4.6) show a good agreement between the analytical solution (contour lines) and the numerical results (contour flood), even if the boundary conditions are not namely the same. Also the results of the solution of the three dimensional diffusion equation (Figure 4.7) show the expected results that are a diffusion of the high concentration zones. In this figure, for sake of brevity, only the evolution in time for $Pe = 1$ is reported, but also the simulations performed at different Peclet numbers (with the same initial field), show the same behavior. The last two figures show only the first

half of the channel, because the same results are founded in to the other; this is due to the periodic initialization alon $x$ which has been mentioned above.

## 4.2 Simplified Cahn - Hilliard equation

In this section the solution of the double-Helmholtz equation system is tested; for this purpose the Cahn-Hilliard equation 3.32 has been first simplified in its non-linear terms $S_c$, in order to obtain a "fourth order" formulation of the diffusion equation. In this way, even if the problem does not have a physical meaning, the coupled Helmholtz solver can be tested. Then the neglected terms are then re-introduced in to the non linear term $S_c$ and the complete Cahn-Hilliard equation is tested. Since from this analysis a detriment of accuracy has been observed along the $z$ direction, also some different temporal IMEX schemes have been tested.

### 4.2.1 Rewritten diffusion equation

To test the double-Helmholtz equation solver, the Cahn-Hilliard equation have been rewritten in the following way using the operator splitting technique shown in Section 3.2. In this way the equation obtained is equal to the equation 4.1 where, for sake of brevity, the "$\pm$" symbol has been used with the meaning of sum and difference of the operator.

$$\frac{\partial \phi}{\partial t} = \frac{1}{Pe}\nabla^2\phi \pm \frac{2}{Pe}\nabla^2\phi \pm \frac{\Delta t}{2Pe}\nabla^2 \cdot \nabla^2\phi \tag{4.11}$$

Applying the IMEX temporal discretization, the $S_C$ and the $\psi_C$ terms yield to the following:

$$\begin{aligned} S_C &= \frac{1}{Pe} - \left(\nabla^2\phi + \frac{\Delta t}{2Pe}\nabla^2 \cdot \nabla^2\phi\right) \\ \psi_C &= \frac{2}{Pe}\nabla^2\phi - \frac{\Delta t}{2Pe^2}\nabla^2 \cdot \nabla^2\phi \end{aligned} \tag{4.12}$$

In this way, the equation 4.1 is not modified in its differential form and this can be proven substituting the operators above in to equation 3.34:

$$\begin{aligned} \frac{\partial \phi}{\partial t} &= S_C + \phi_C \\ &= -\frac{1}{Pe}\nabla^2\phi + \frac{\Delta t}{2Pe^2}\nabla^2 \cdot \nabla^2\phi + \frac{2}{Pe}\nabla^2\phi - \frac{\Delta t}{2Pe^2}\nabla^2 \cdot \nabla^2\phi \\ &= \frac{1}{Pe}\nabla^2\phi \end{aligned} \tag{4.13}$$

The system of Helmholtz equations obtained is similar to the equations system in equation 3.44, where the only difference is due to the non-linear terms. As reported in Section 4.1.1, because the phase field simulations are ran imposing no-flux at the walls, only this BC is tested. Furthermore, because the formulation along the periodic directions $x$ and $y$ does not vary significatively from the formulation of equation 4.1 to the "fourth order" formulation of equation 4.11, only the solution along the wall-normal direction is tested. First the mono-dimensional analytical field reported by equation 4.6 has been imposed; the numerical results have been compared with the analytical results obtained from the equation 4.7 obtaining the results collected in Figure 4.8. Then a double ribbed concentration profile has been imposed and solved, obtaining the results reported in Figure 4.9, whereas the simulation parameters are summarized in Table 4.3.

| **Grid nodes** | **Pe** | $\Delta t$ |
|---|---|---|
| $64 \times 64 \times 65$ | 0.01 | $10^{-4}$ |
| $64 \times 64 \times 65$ | 0.10 | $10^{-4}$ |
| $64 \times 64 \times 65$ | 1.00 | $10^{-3}$ |
| $64 \times 64 \times 65$ | 10.0 | $10^{-3}$ |
| $64 \times 64 \times 65$ | 100 | $10^{-3}$ |
| $64 \times 64 \times 65$ | 1000 | $10^{-3}$ |

Table 4.3: Modified diffusion equation simulation parameters: Neumann boundary conditions

From the comparison between the analytical and the numerical solution reported in Figure 4.8, a complete matching is observed; also the solution of the double-ribbed initial field (Figure 4.9) gives the expected results, that are a faster smooth of the concentration profile the lower is the Peclet number. From

this results the Chebyshev-Tau solution seems to be properly implemented, thus the non linear operator $S_C$ is rewritten in its complete form an tested in the following section.

### 4.2.2 Cahn - Hilliard equation

The non linear term reported in to equation 4.11 has been completed in order to obtain the Cahn-Hilliard equation, where the mobility has been kept constant (setting $\lambda = 0$). In this way the number of non-linear operators is reduced and the benchmark procedure is simplified. Stating this the equation 3.30 reads the following form:

$$\begin{aligned} S_C &= \frac{1}{Pe}\left[-3\nabla^2\phi + \nabla^2\phi^3 + \left(\frac{\Delta t}{2Pe}\nabla^2\cdot\nabla^2\phi - \frac{Ch^2}{\nabla}^2\cdot\nabla^2\phi\right)\right] \\ \psi_C &= \frac{2}{Pe}\nabla^2\phi - \frac{\Delta t}{2Pe^2}\nabla^2\cdot\nabla^2\phi \end{aligned} \tag{4.14}$$

First the equation has been solved without the flow field imposing the following step initial concentration field:

$$\begin{cases} \phi = \phi_1 & \text{if} \quad 0 \le z < 7 \\ \phi = \phi_2 & \text{if} \quad 14 < z \le 20 \\ \phi = \phi_1 \cos\left(\pi\frac{z-7}{7}\right) & \text{if} \quad 7 \le z \le 14 \end{cases} \tag{4.15}$$

Where $\phi_1 = 1$ and $\phi_2 = -1$. The initial field described above allow to make a comparison with the planar theoretical profile, described by the following equation:

$$\phi = \tanh\left(\frac{zRe}{\sqrt{2}Ch}\right) \tag{4.16}$$

The solution has been performed imposing $\Delta t = 0.8\cdot 10^{-7}$ in order to respect the stability condition suggested by Christov *et al.*[9] and an example of the confrontation between the analytical and the numerical results is reported in Figure 4.1. The interface is not correctly reproduced and some high oscillations can be observed at the walls. Furthermore these instabilities are not damped by the code during the next time-steps, thus the solution diverges.

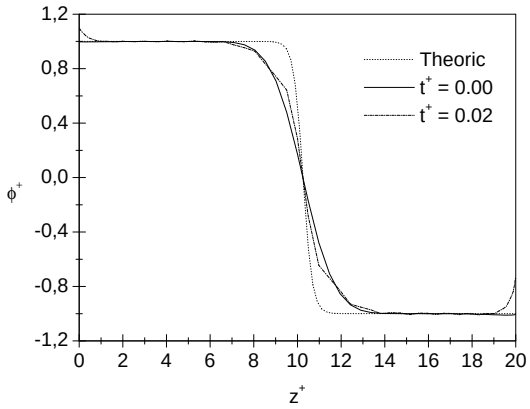


Figure 4.1: Solution of the Cahn - Hilliard equation: comparison of planar interface analytical and numerical profiles, along the wall-normal direction for $Pe = 1$, on $x^+ = 60$ and $y^+ = 30$ plane. Neumann boundary conditions and step initial field.

Several authors, as Badalassi *et al.*[4] and Ascher *et al.*[3], pointed out that the Crank-Nicolson scheme, applied on to high order PDE's, can show instabilities even if it is used in its dissipative regime ($\Delta t < Ch^2$). Hence, in order to prove if the instabilities encountered at the walls are independent on the temporal discretization algorithm, different IMEX schemes of different orders have been tested, changing both the implicit and the explicit discretization. Based on Canuto *et al.*[8] the following combinations of explicit schemes with the Crank-Nicolson implicit scheme have been tested: third order Adams-Bashfort (CN-AB3), second order Runge-Kutta (CN-RK2) and backward Euler (CN-E) (Yue *et al.*[39]). Following Badalassi *et al.*[4], the so-called Gear temporal scheme has been tested; it is based on the *second-order backwards difference scheme* and is usually known as SBDF scheme. As reported by Canuto *et al.*[8], the CN based schemes and the SBDF scheme show opposite stability regions, thus a quite complete analysis is performed. The numerical algorithms have been tested on a smoothed ribbed-like initial field, which reduces the initial oscillations with respect to a sharp ribbed initial field. The initial concentration field is described by the following equations system, whereas the CH equation discretized in time with the schemes above, is briefly reported in Appendix A:

$$\begin{cases} \phi = \phi_1 & \text{if} \quad 0 \leq z < 4 \quad \text{and} \quad 17 < z \leq 20 \\ \phi = \phi_2 & \text{if} \quad 9 < z < 12 \\ \phi = \phi_1 \cos\left(\pi \frac{z-4}{5}\right) & \text{if} \quad 4 \leq z \leq 9 \\ \phi = \phi_2 \cos\left(\pi \frac{z-12}{5}\right) & \text{if} \quad 12 \leq z \leq 17 \end{cases} \tag{4.17}$$

Where $\phi_1 = -1$ and $\phi_2 = 1$. The simulation parameters are collected in Table 4.4, where the time step $\Delta t$ has been chosen in order to drive the CN scheme in its stable region ($\Delta t < Ch^2$) and also in order to respect the condition suggested by Christov *et al.*[9] for the numerical solutions of equations where some fourth order schemes are treated explicitly. The authors suggested $\Delta t \leq 1/(4 \cdot \min(\Delta z)^4)$ as the stability constraint for this class of problems, thus, for Chebyshev collocation method, it yields to the value reported in Table 4.4.

| **Grid nodes** | **min**$(\Delta z)$ | **Pe** | **Ch** | $\Delta t$ |
|---|---|---|---|---|
| $64 \times 64 \times 65$ | 0.1205 | 1.0 | 0.1 | $0.8 \cdot 10^{-}6$ |

Table 4.4: Simulation parameters of the numerical scheme test

The results of the simulations are reported in Figure 4.10, where for sake of clarity only the wall zones have been reported and also the concentration axes have been braked. From these figures is possible to appreciate that the solution is not accurate for every kind of scheme, even if differences in magnitude are registered. These oscillations are not damped in the next calculations, thus they drive rapidly the solution to diverge, even if the most stiff time-step constraint has been respected and no gradients have been introduced at the walls. To simplify the problem a two dimensional approach has been chosen, in this way the $z$ direction can be neglected avoiding the problems reported above. To prove the ability of the code to create the interface, a sharp profile has been imposed on the $x - y$ plane, and the simulation has been performed imposing the parameters reported in Table 4.5, where the Cahn number has been chosen in order to obtain a value suitable for an interface thickness of three grid points.

The results of the simulation are reported in Figure 4.11, where the interface creation can be easily observed. The time-step used for the simulation is higher than the $\Delta t$ introduced in to the tests performed along the $z$ direction, because

| **Grid nodes** | **Pe** | **Ch** | $\Delta t$ |
|---|---|---|---|
| $64 \times 64 \times 65$ | 0.01 | 0.1 | $10^{-3}$ |

Table 4.5: Simulation parameters of Cahn-Hilliard equation: Interface creation test

of the uniform grid spacing. Hence, introducing initial fields constant along the wall-direction the problems evidenced in this section are not encountered, allowing to obtain the two-dimensional results reported in the following section.

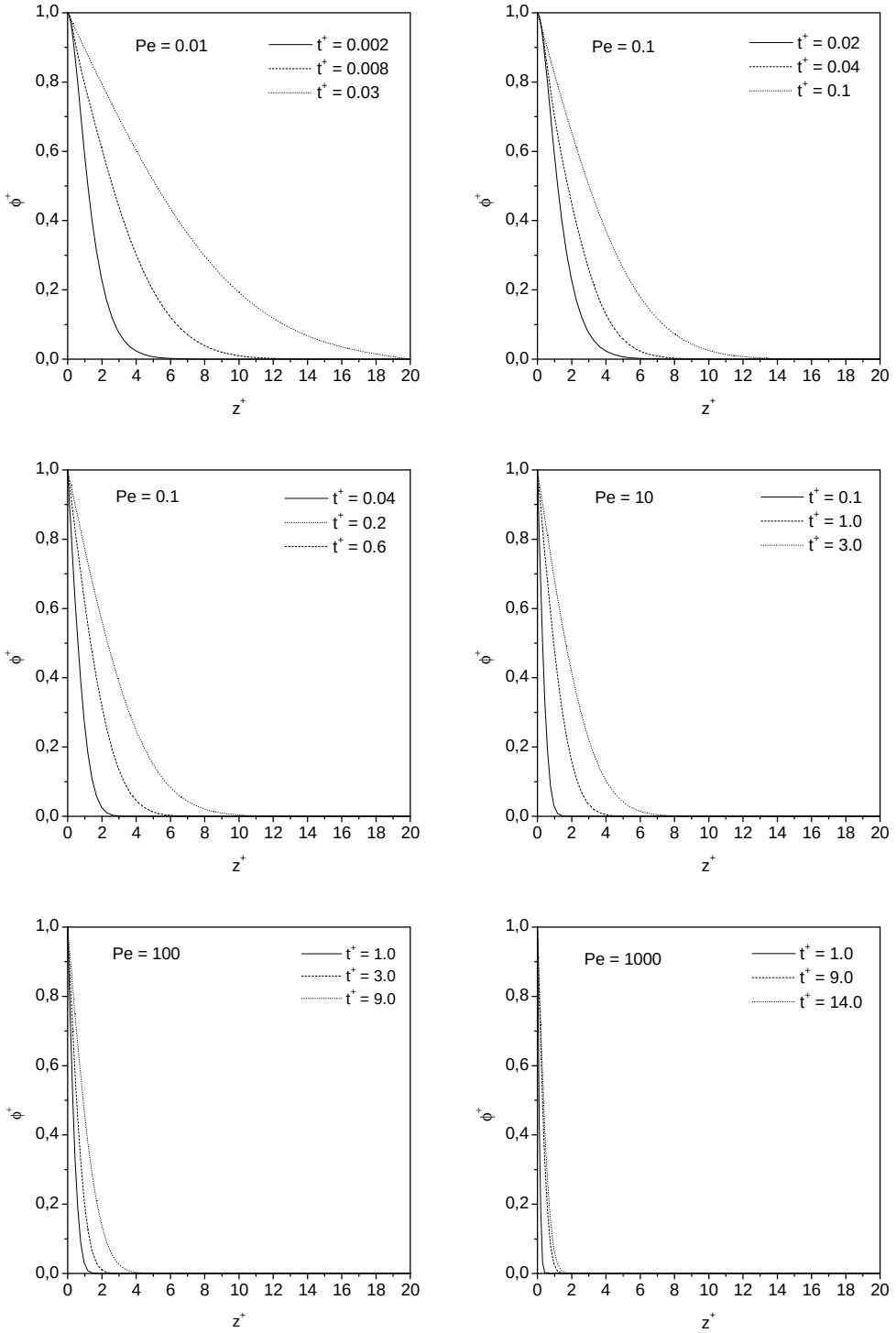


Figure 4.2: Solution of the diffusion equation: concentration profiles along the wall-normal direction for different Peclet numbers on $x^+ = 60$ and $y^+ = 30$ planes. Dirichlet boundary conditions and constant initial field.

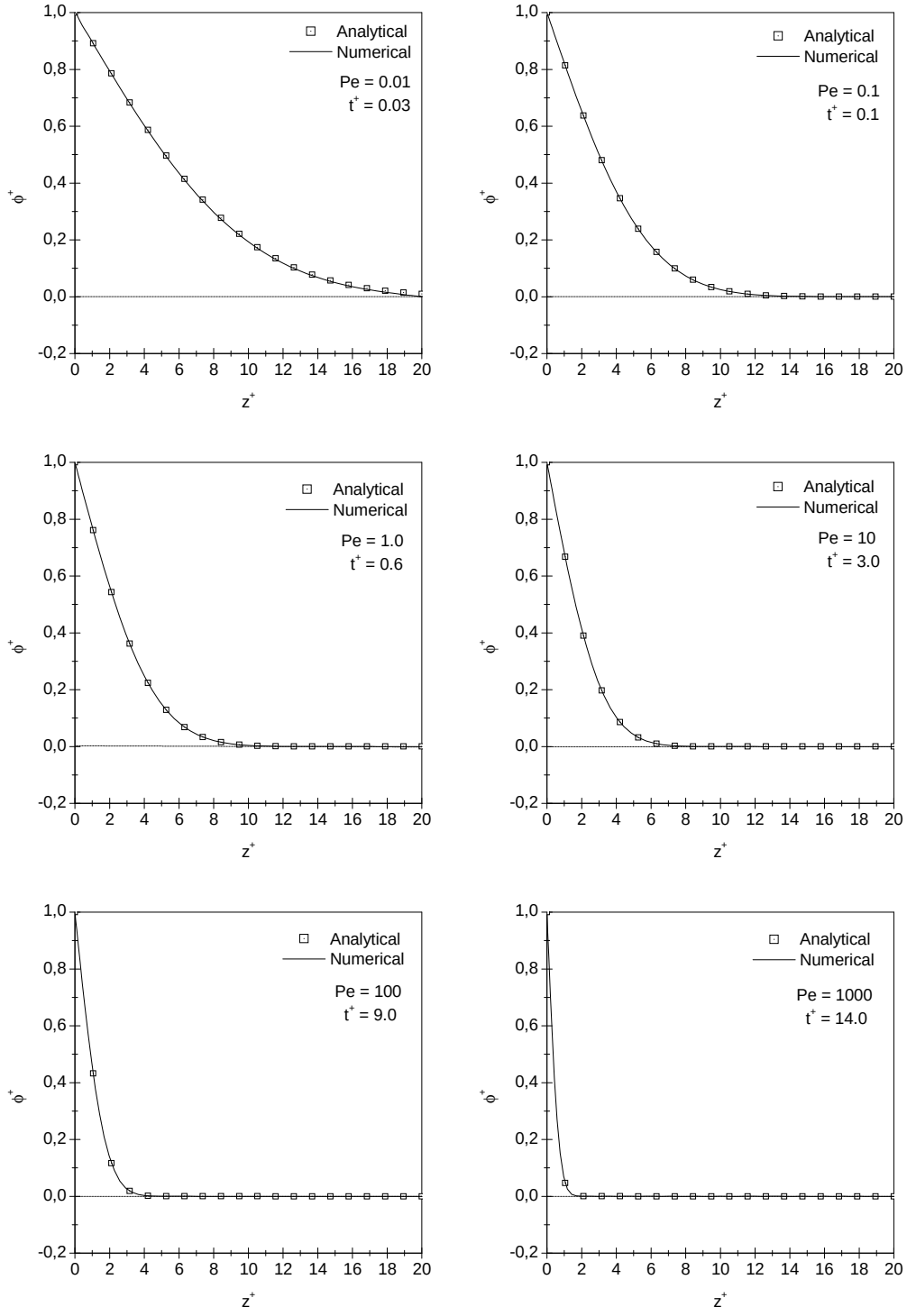


Figure 4.3: Solution of the diffusion equation: comparison between the analytical and numerical concentration profiles, along the wall-normal direction, for different Peclet numbers on $x^+ = 60$ and $y^+ = 30$ planes. Dirichlet boundary conditions and constant initial field.

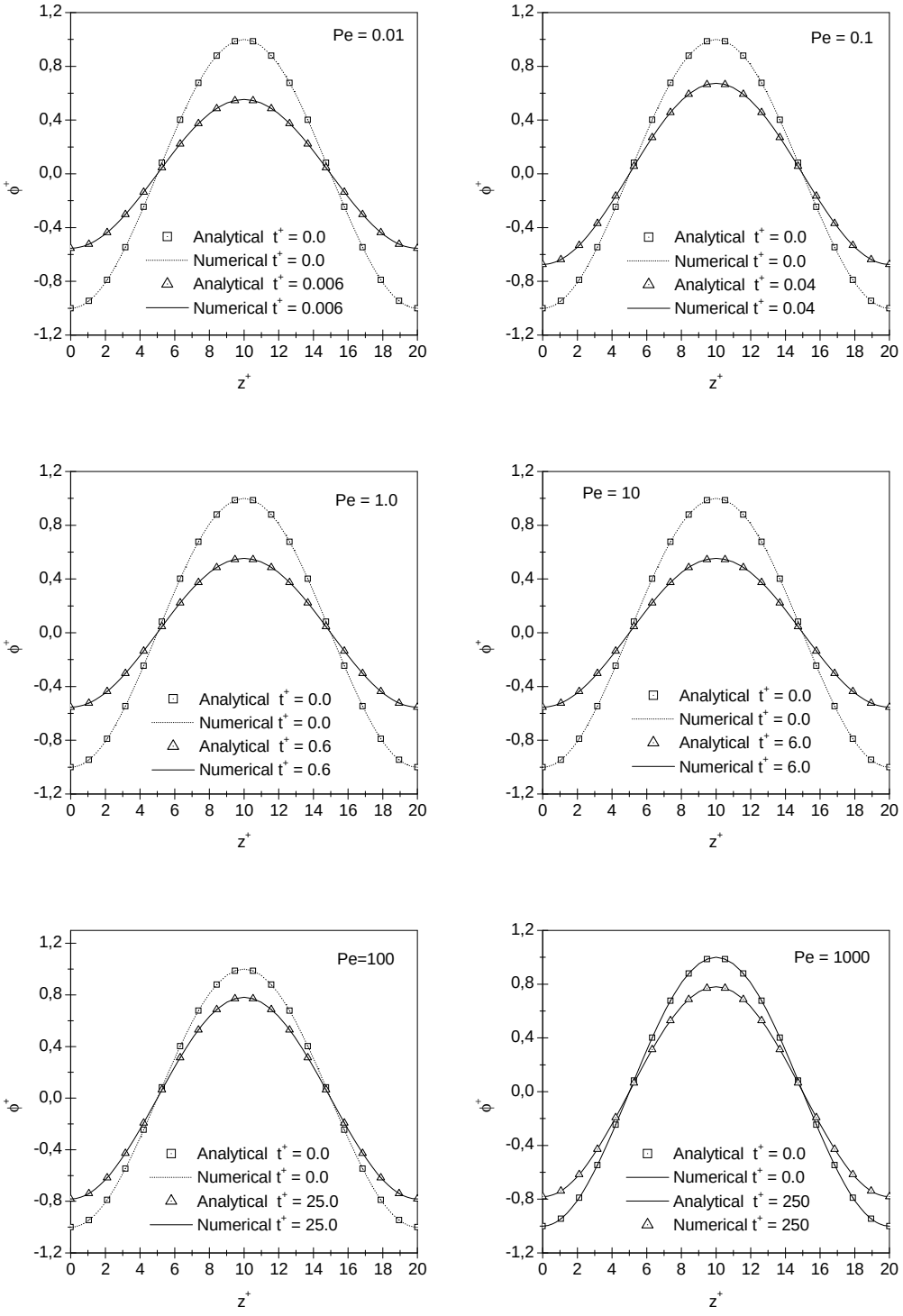


Figure 4.4: Solution of the diffusion equation: comparison between the analytical and numerical concentration profiles along the wall-normal direction for different Peclet numbers on $x^+ = 60$ and $y^+ = 30$ planes. Neumann boundary conditions and analytical initial field.

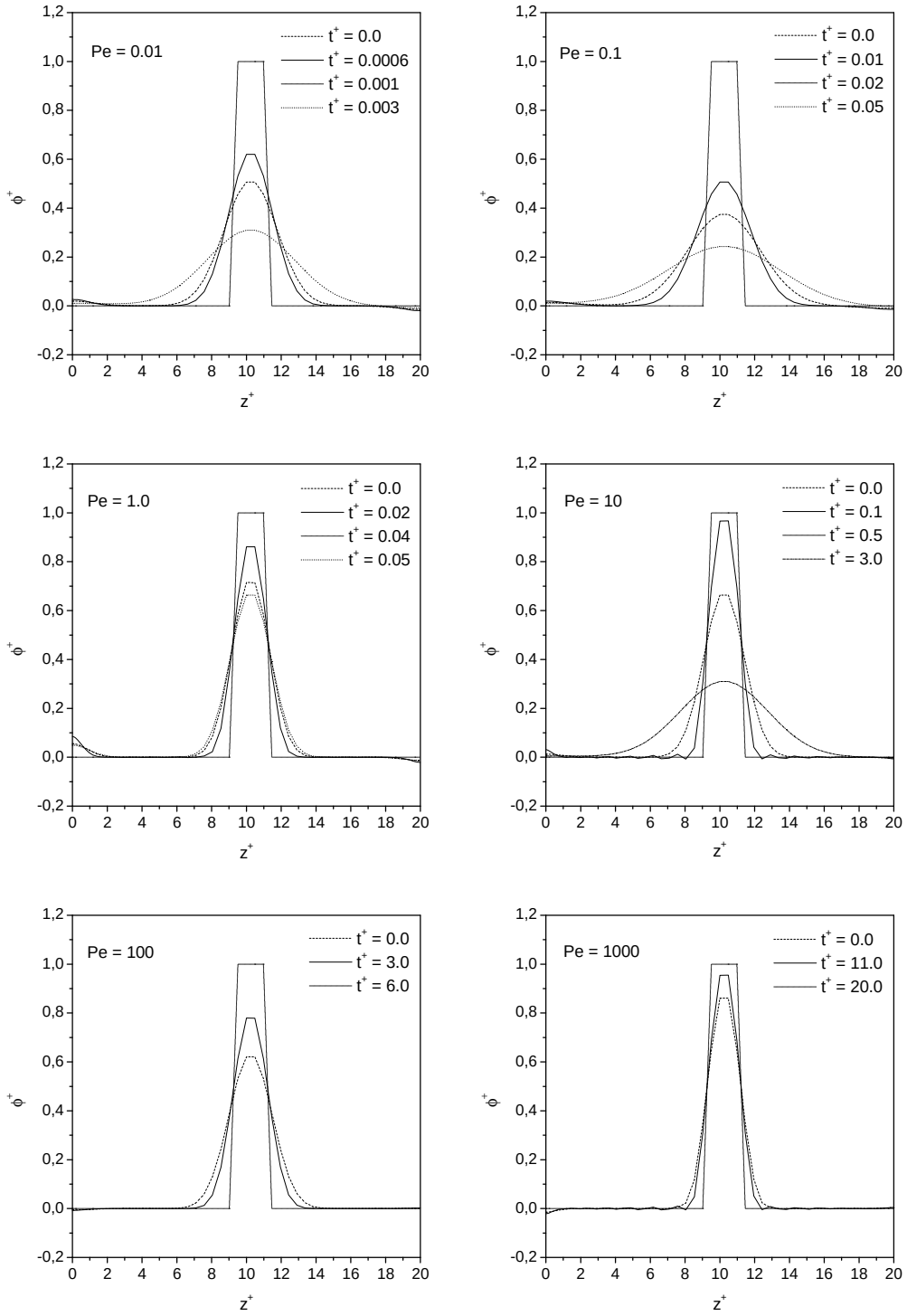


Figure 4.5: Solution of the diffusion equation: concentration profiles along the wall-normal direction for different Peclet numbers on $x^+ = 60$ and $y^+ = 30$ planes. Neumann boundary conditions and ribbed-like initial field.

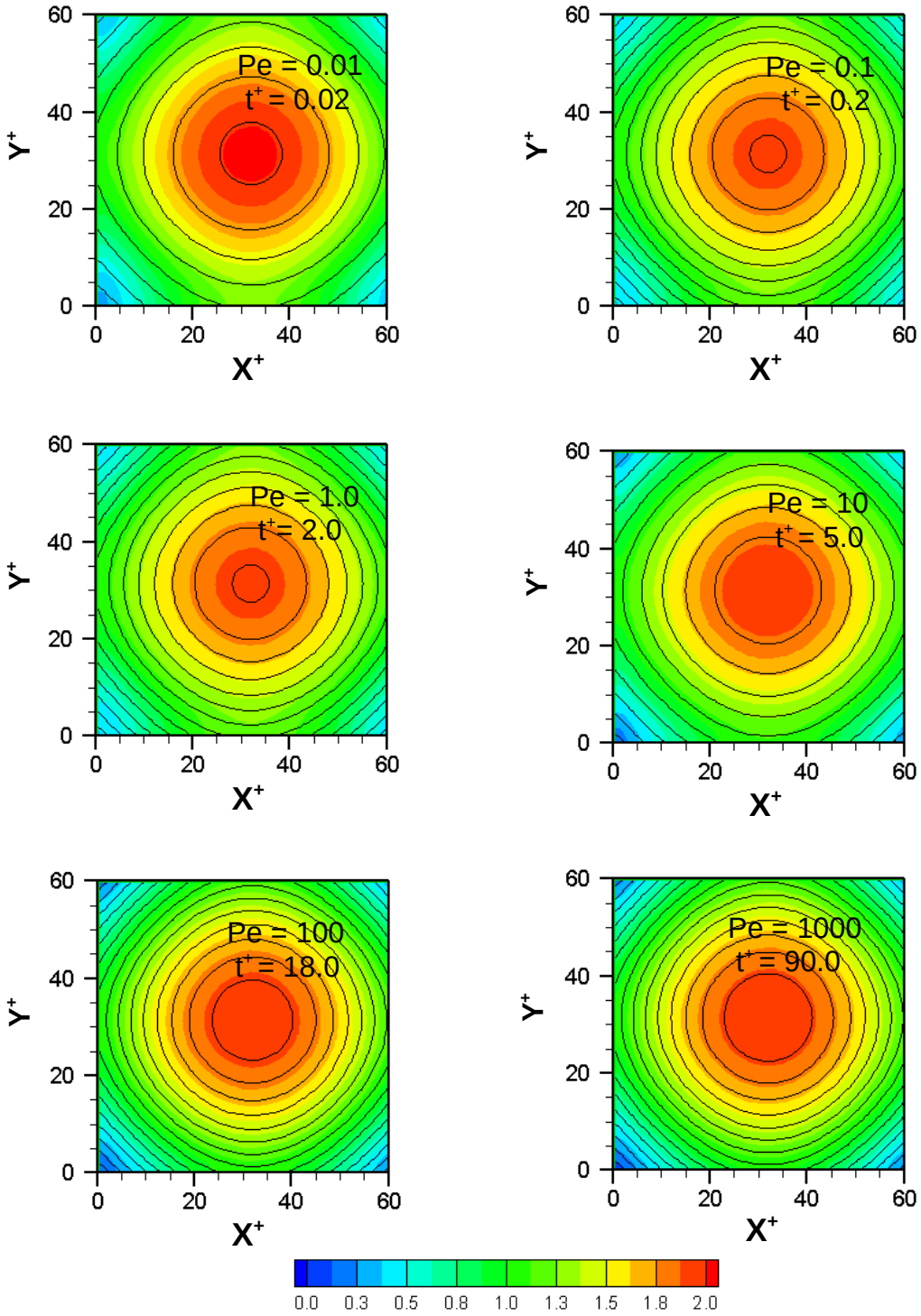


Figure 4.6: Solution of the diffusion equation: comparison between the analytical (line) and numerical (flood) concentration contours at $Pe = 1.0$ on $z^+ = 20$ plane. Fixed flux $\mathbf{n}\nabla\phi^+ = 0$ at the walls and analytical initial field.

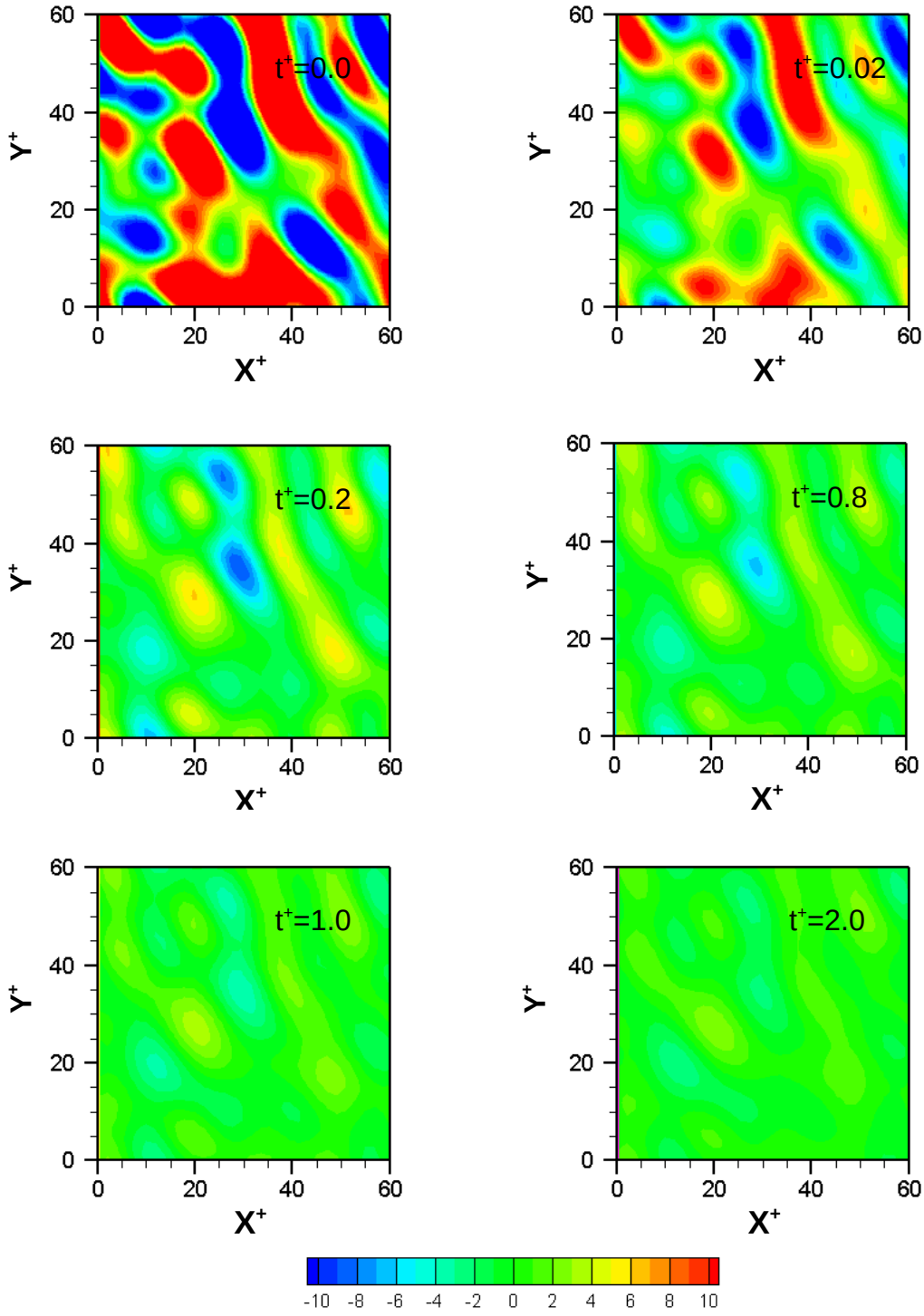


Figure 4.7: Solution of the diffusion equation: contour plots of the temporal evolution of the concentration field for $Pe = 1.0$ on $z^+ = 20$ plane. Neumann boundary conditions and random initial field.

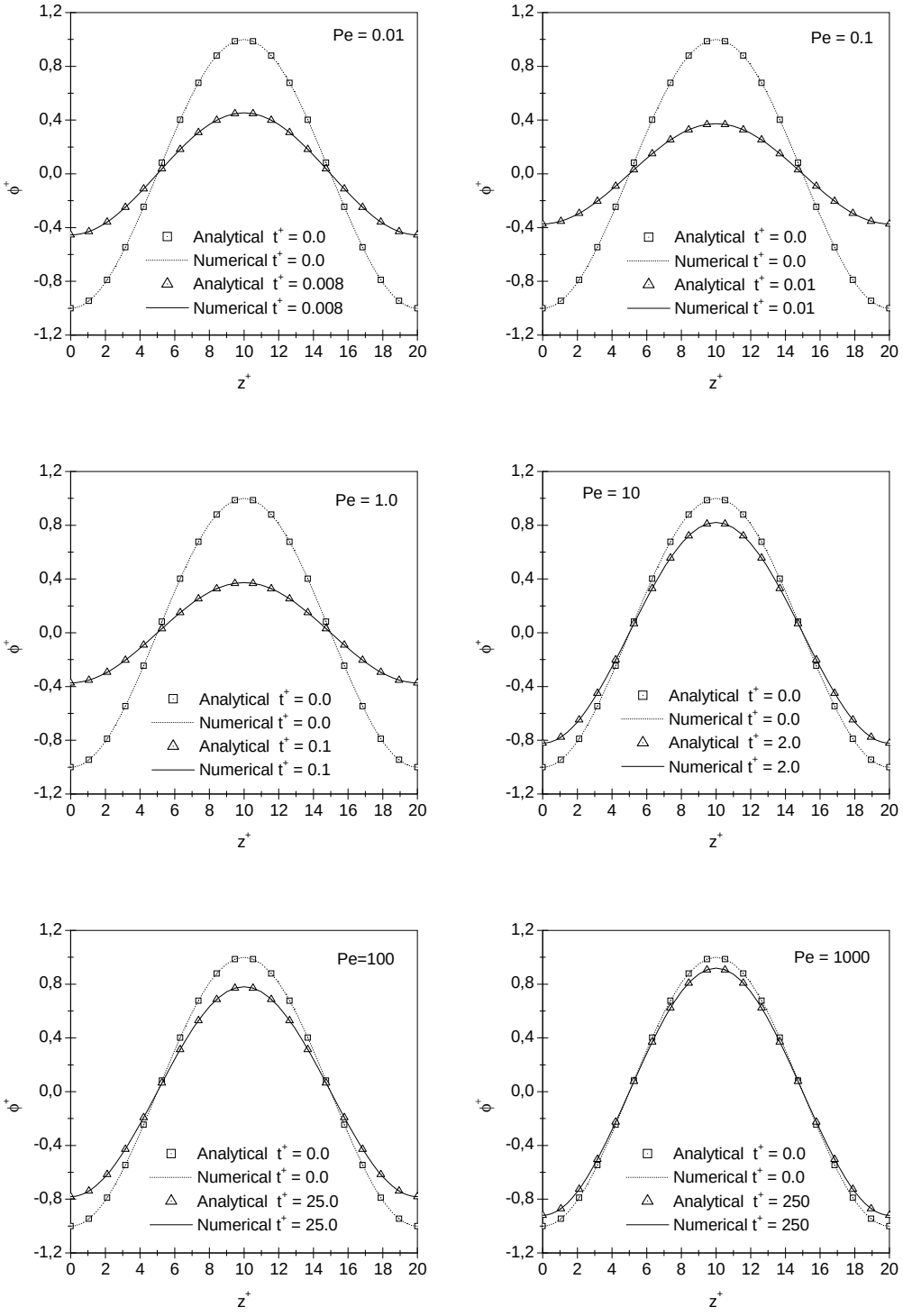


Figure 4.8: Solution of the rewritten diffusion equation: comparison between the analytical and numerical concentration profiles along the wall-normal direction for different Peclet numbers on $x^+ = 60$ and $y^+ = 30$ planes. Neumann boundary conditions and analytical initial field.

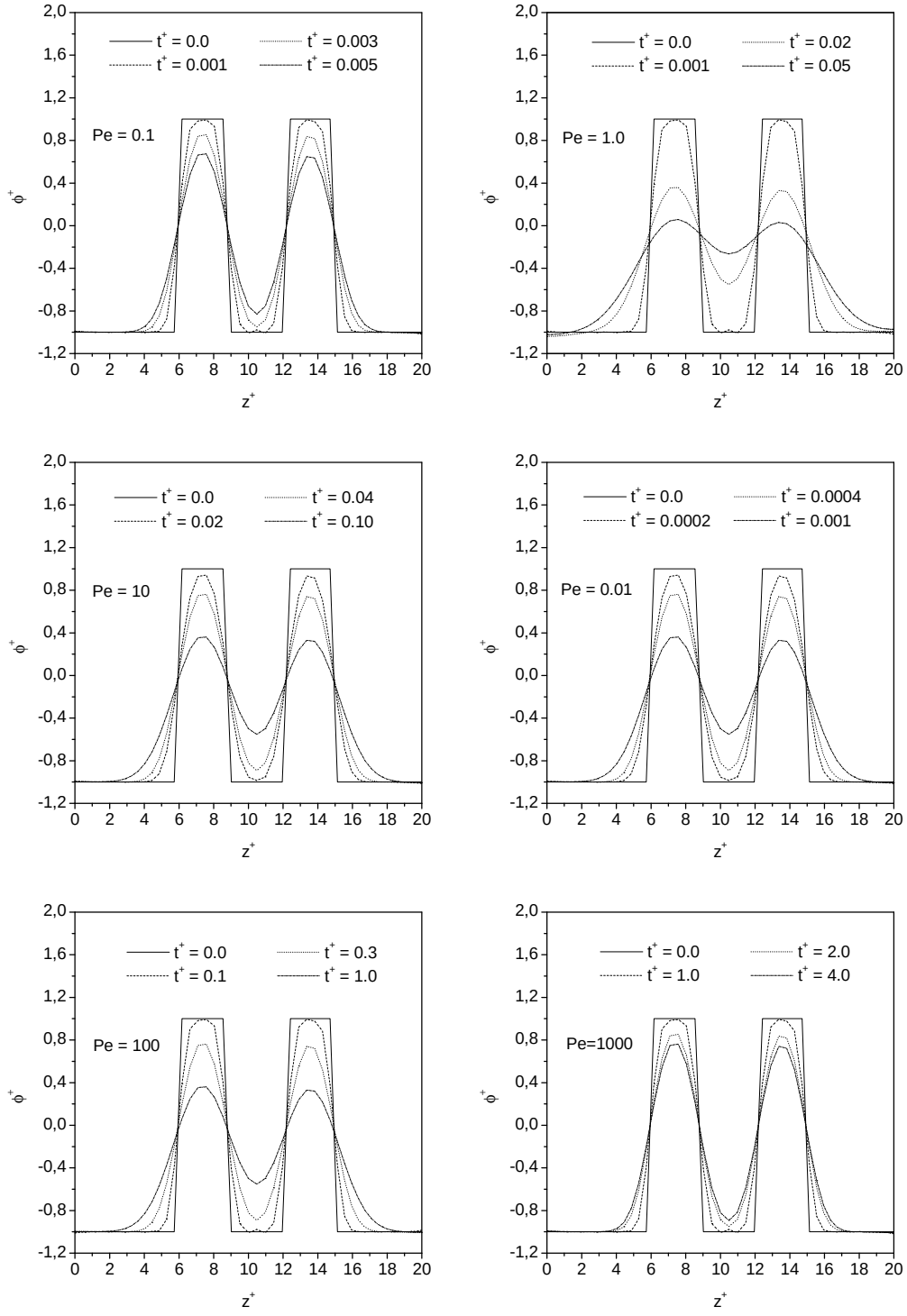


Figure 4.9: Solution of the rewritten diffusion equation: concentration profiles along the wall-normal direction for different Peclet numbers, on $x^+ = 60$ and $y^+ = 30$ planes. Neumann boundary conditions and double ribbed-like initial field.

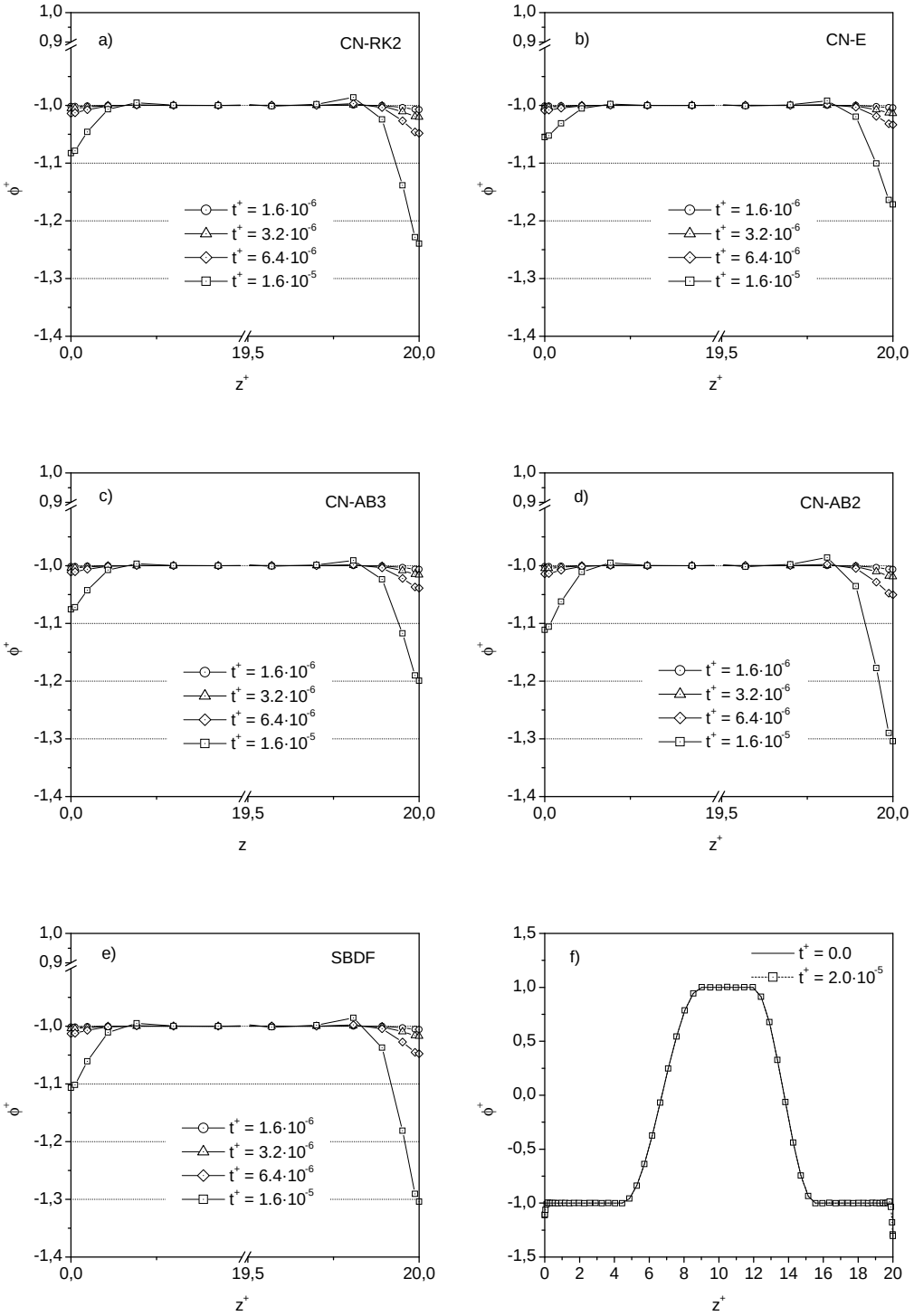


Figure 4.10: Solution of the Cahn - Hilliard equation: comparison between different numerical schemes, on $x^+ = 60$ and $y^+ = 30$ planes. Neumann boundary conditions and smoothed ribbed-like initial field. Figures from $a$ to $e$) shows only the wall zone, whereas figure $f$) shows the complete field.

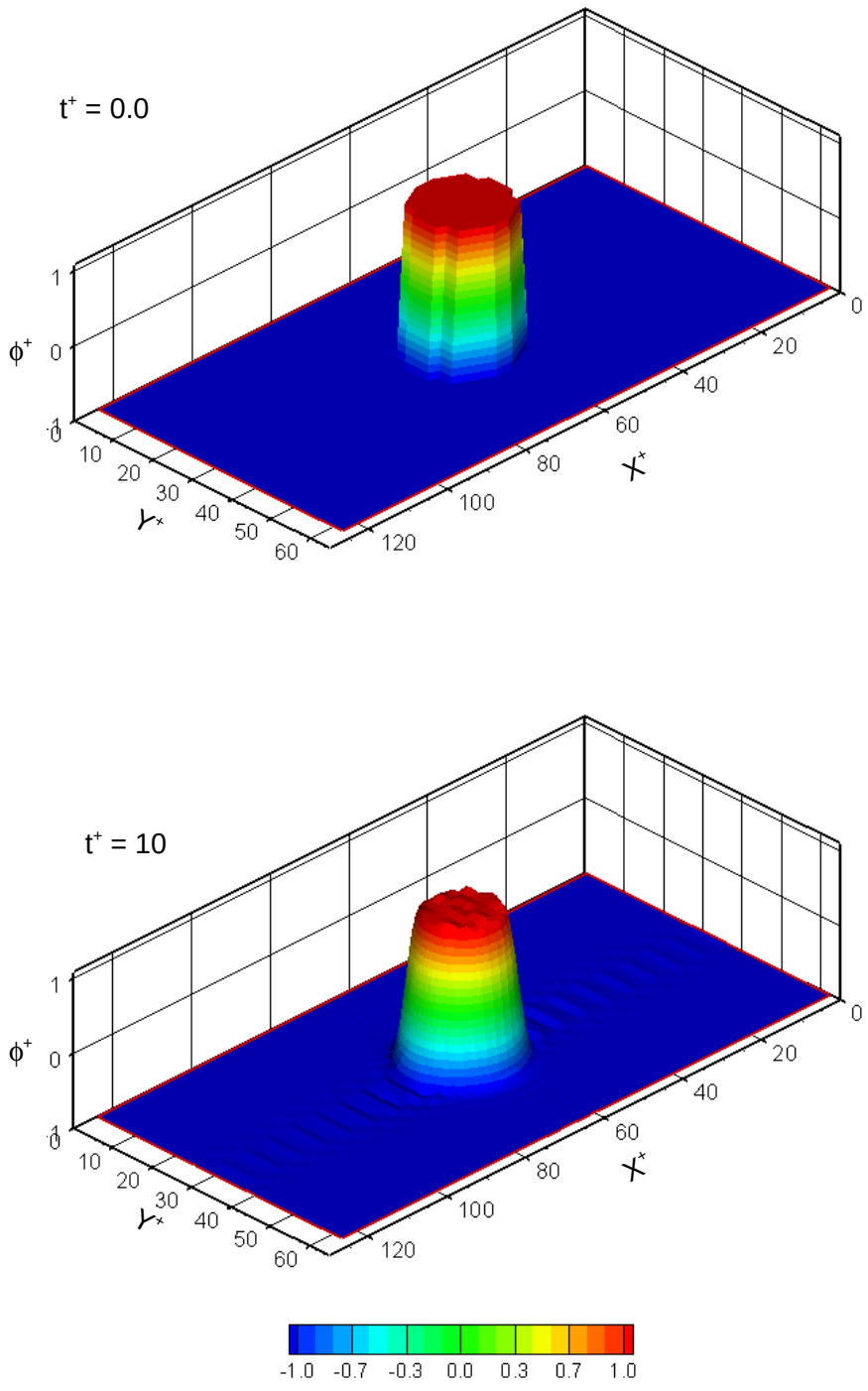


Figure 4.11: Solution of the Cahn - Hilliard equation: example of bi-dimensional interface creation on $x - y$ planes. Neumann boundary conditions and sharp two dimensional initial field.

# Chapter 5

# Numerical results

The benchmarks reported in Chapter 4, evidenced a dramatic detriment of the solution accuracy at the walls, that produces oscillations which are not damped in the next calculations, which drive the solution to diverge. For this reason the geometry has been simplified to a bi-dimensional channel, avoiding the presence of the walls. This scope has been achieved keeping the concentration field and the flow field constant along the $z$ direction, hence the Chebyshev approximation of the derivatives along this direction, is identically zero and the instabilities are not detected anymore. This simplification does not reduce the generality of the solution, in fact, following Lamorgese *et al.*[23] and Badalassi *et al.*[4], the two-dimensional results show the same behavior of the three-dimensional solution. In this chapter the results obtained from the bi-dimensional simulations are reported, particularly in Section 5.1 the pure phase separation of a binary mixture in absence of flow is reported, whereas in Section 5.1.2 the phase separation of a binary mixture has been simulated under shear flow.All the simulations reported in this section have been performed fixing $Re_\tau = 10$ which generates a domain of $0 \leq z^+ \leq 20$ in the wall direction, $0 \leq y^+ \leq 60$ and $0 \leq x^+ \leq 120$ in the spanwise and lengthwise directions respectively.

## 5.1 Phase separation

In this numerical experiment an initial homogeneous binary mixture is driven in to a meta-stable region, obtaining the separation of the two phases into ordered

structures. As shown in Chapter 1, when a multi-phase system (composed of partially miscible fluids) is driven in to a meta-stable region of its phase diagram, the mixture is forced to separate if a little perturbation is introduced in to the system. Thus, in order to obtain the phase separation, the domain has been first initialized with a constant concentration field $\phi_0$, at which the mixture is in a meta-stable condition; then a random noise, described by the following equation, has been superposed on it.

$$\phi(x,y) = \phi_0 + r(x,y) \qquad \text{where} \qquad -10^{-2} \leq z \leq 10^{-2} \tag{5.1}$$

Following Lamorgese *et al.*[23] and Badalassi *et al.*[4] the pseudo-random noise $r(x,y)$ has been chosen to be characterized by a zero mean value in space, in this way the system is not arbitrary forced to move to one, or to the other other equilibrium condition.

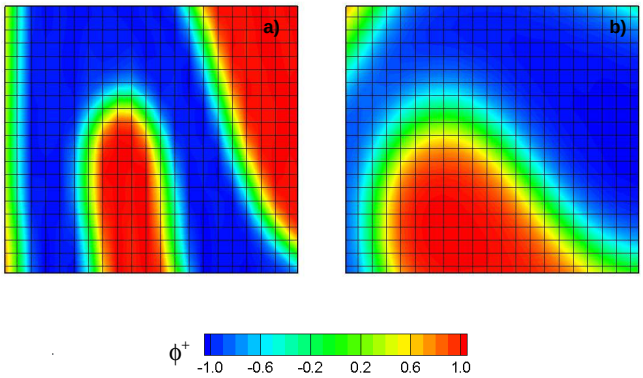


Figure 5.1: Interface thickness and grid spacing for different Cahn numbers with 64×64 mesh. Figure *a*) shows the three grid-points interface obtained for $Ch = 0.1$, whereas Figure *b*) shows the five grid-points interface obtained for $Ch = 0.2$.

To allow the code to create the interfaces, the Cahn number has been chosen in order to describe the interface with at least three mesh points [4]. Thus, considering the dimensionless interface thickness defined in Section 2.3.3, $l = 4.164ChH$ and the maximum grid spacing $\Delta x = (4\pi H)/N_x$, the Cahn number reads:

$$Ch = (n-1)\frac{4\pi H}{N_x 4.164 H} = 0.96(n-1)\frac{\pi}{N_x} \tag{5.2}$$

Where $n$ is the number of the grid-points used to described the interface. The interface thickness in relation to the mesh spacing is shown in Figure 5.1, where the mesh grid is superposed on the concentration contour for two different Cahn numbers. The time-step has been chosen using a trial-and-error approach, in fact, due to the high non-linearity of the Cahn-Hilliard equation, an analytical CFL (Courant-Friedrichs-Lewy) condition cannot be defined [23]. In the first steps of the simulations $\Delta t$ has been chosen in order to respect namely the condition suggested by Christov *et al.*[9] (see Section 4.2.2), then, when the pure phase domains shown a consistent dimension, the time-step has been increased keeping in account the value of Peclet and the Cahn number.

### 5.1.1 Pure spinoidal decomposition

To obtain the pure spinoidal decomposition, the Cahn-Hilliard equation 3.29 has been solved neglecting the convective term $\mathbf{u} \cdot \nabla \phi$ [4] and, for sake of simplicity, the mobility has been kept constant ($\gamma = 0$). Under these approximations, the CH equation reads:

$$\frac{\partial \phi}{\partial t} = +\frac{1}{Pe} \nabla \left( \nabla \phi^3 - \nabla \phi - Ch^2 \nabla \cdot \nabla^2 \phi \right) \tag{5.3}$$

Following Badalassi *et al.*[4] the numerical experiments have been performed at $Pe = 1$, which means that the diffusive time scale is of the same magnitude of the convective time scale. Because of the absence of the convective term, the convective phenomena observed in to the system are due to the concentration gradients, thus, following Lamorgese *et al.*[23] the convective time-scale has been chosen to be $T_c \propto \frac{1}{\max(\partial \phi / \partial x + \partial \phi / \partial y)}$. The simulation has been repeated at higher and lower Peclet numbers, which correspond, respectively to systems with diffusive time-scales higher and lower than the convective time scale. Furthermore the same simulations have been performed with different meshes in order to check the influence of the spatial discretization. To observe the effect of the Cahn number on the interface thickness and also on the morphology of the separated system, the numerical solution at $Pe = 1$ has been performed for $Ch = 0.1$ and $Ch = 0.2$ which corresponds respectively to an interface thickness of three and five grid-points. All the simulation parameters are collected in Table 5.1. In Figure $512 \times 512$ the preliminary results for a $512 \times 512$ mesh are

shown.

| Grid nodes | Pe | Ch |
|---|---|---|
| $64 \times 64$ | 0.1 | 0.1 |
| $64 \times 64$ | 1.0 | 0.1 |
| $64 \times 64$ | 1.0 | 0.2 |
| $64 \times 64$ | 10.0 | 0.1 |
| $128 \times 128$ | 0.1 | 0.05 |
| $128 \times 128$ | 1.0 | 0.05 |
| $128 \times 128$ | 10.0 | 0.05 |
| $256 \times 256$ | 1.0 | 0.025 |
| $512 \times 512$ | 1.0 | 0.013 |

Table 5.1: Pure spinoidal decomposition simulation parameters

To characterize the distance of the system from the local equilibrium, the *separation depth* $s$ has been introduced following Lamorgese *et al.*[23] and Vladimirova *et al.*[36]:

$$s = \left\langle \frac{\phi(\mathbf{x}) - \phi_0}{\phi(\mathbf{x})_{eq} - \phi_0} \right\rangle \qquad \text{where} \qquad \begin{cases} \phi(\mathbf{x})_{eq} = \phi_1 & \text{if} \quad \phi(\mathbf{x}) > 0 \\ \phi(\mathbf{x})_{eq} = \phi_2 & \text{if} \quad \phi(\mathbf{x}) < 0 \end{cases} \tag{5.4}$$

Where $\phi_1$ and $\phi_2$ are the two equilibrium concentrations of the binary system. The comparison of the separation depth in time for different Peclet numbers and different meshes, is reported in Figure 5.2, whereas the comparison between the evolution in time of for different meshes and $Pe = 1$, is reported in Figure 5.3.

Since no convection has been included, in this simulations the structure evolution is completely driven by the diffusion and thus, starting from the same initial conditions, the evolution should be the same [36]. Observing the results reported in Figure 5.2, the evolution curves seem to show the same behavior for every Peclet number but, the lower is $Pe$, the faster is the separation process. This result has been expected in fact, increasing the Peclet number, the diffusive time-scale decreases with respect $T_c$ and the process is slower. On the other and, decreasing $Pe$, the diffusive time-scale of the system became lower than $T_c$, thus

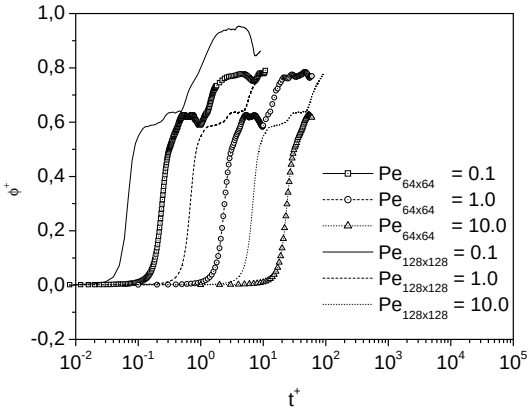


Figure 5.2: Pure spinoidal decomposition: evolution in time of the separation depth for different Peclet numbers with $64 \times 64$ and $128 \times 128$ meshes.

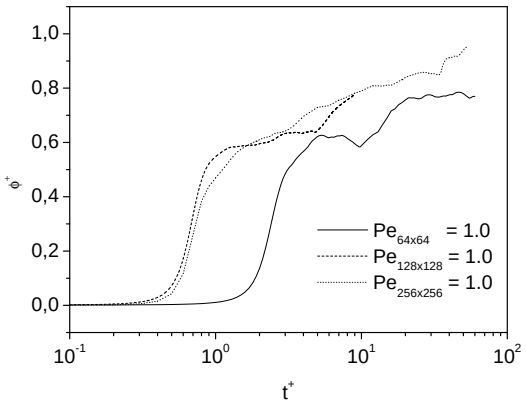


Figure 5.3: Pure spinoidal decomposition: comparison of the time evolution of the separation depth for $Pe = 1$ and different meshes.

the process is faster. The results are confirmed also for different meshes.

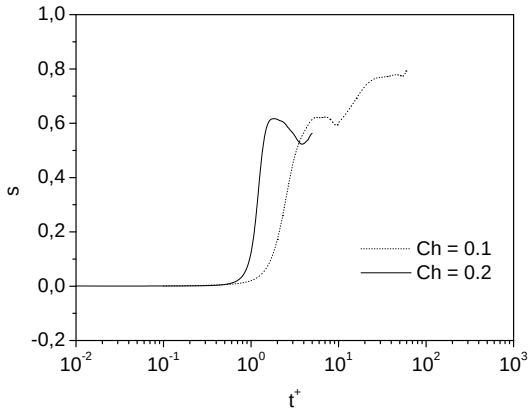


Figure 5.4: Pure spinoidal decomposition: comparison between the evolution in time of the separation depth for different Cahn numbers, $Pe = 1$ and $64 \times 64$ mesh.

The morphology evolution in time at $Pe = 1$, for a three grid-point interface thickness is reported in Figure 5.7; whereas Figure 5.8 shows the structure evolution, for a five grid-point interface thickens (both of them, calculated for a $64 \times 64$ mesh). From these figures the differences between the interface thickness can be easily detected: the interface obtained from the simulation performed at $Ch = 0.2$ is larger than the interface obtained from the calculations performed at $Ch = 0.1$. This result is consistent with the definition of Cahn number reported in Section 2.3.3 and also with the equation 5.2. Figure 5.4 reports the comparison between the separation depth obtained for these two cases, where the evolution in time of $s$ obtained for $Ch = 0.2$ shows an asymptotic value lower than the asymptotic value obtained for $Ch = 0.1$, whereas the initial evolution is almost the same. This behavior seems to be correct, in fact the thicker is the interface, the lower is the volume occupied by the pure phase and thus the lower is the asymptotic value of $s$. Comparing the separation depth reported in Figure 5.7, with the results reported by Vladimirova *et al.*[36] and Lamorgese *et al.*[23], the same behavior is obtained, even if the scaling of the equations is different from the non-dimensional system introduced in Section 2.3, in particular a good agreement is obtained from the simulations performed at $Pe = 1$ and $Pe = 0.1$ (which corresponds to $\alpha = 1$ and $\alpha = 10$ in the works above).

### 5.1.2 Phase separation under shear flow

In this case the initial homogeneous mixture is driven in to a meta-stable region under the presence of shear flow, thus the morphology of the bulk phases, and the interface as well, is influenced by the presence of the flow field. As reported in Chapter 4 the Cahn-Hilliard equation has been solved only along the two periodic directions $x$ and $y$, hence in this preliminary analysis the shear flow has been superposed to the flow field, obtaining the velocity field reported in Figure 5.5.

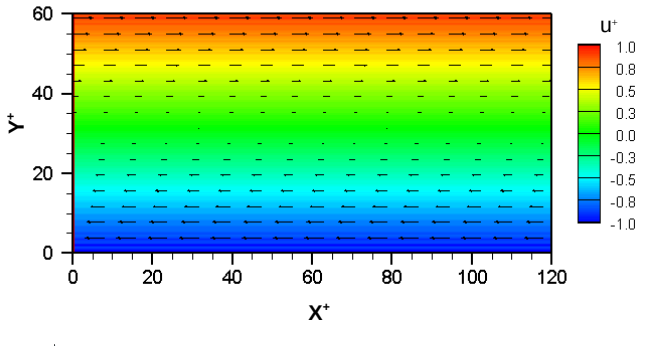


Figure 5.5: Phase separation under shear flow: shear flow field.

This simplification forced to study systems where the capillary forces are negligible with respect to the viscous forces, that are systems characterized by high Capillary numbers ($Ca >> 1$). The concentration field has been initialized following equation 5.2 and the simulation parameters are summarized in Table 5.2.

| **Grid nodes** | **Pe** | **Ch** | **Ch** |
|---|---|---|---|
| $64 \times 64$ | 10.0 | 0.1 | »1 |
| $64 \times 64$ | 100 | 0.1 | »1 |
| $128 \times 128$ | 10.0 | 0.05 | »1 |
| $128 \times 128$ | 100 | 0.05 | »1 |

Table 5.2: Phase-separation under shear flow simulation parameters

In Figure 5.12 and Figure 5.14 the time evolution of the structure obtained for $Pe = 10$ with $64 \times 64$ and $128 \times 128$ meshes respectively are reported, whereas in Figure 5.13 and 5.15 the evolution in time of the morphology obtained for $Pe = 100$ with $64 \times 64$ and $128 \times 128$ meshes are reported. In these figures the bulk phase regions show a stretched morphology along the stream-flow direction. These results are in good agreement with the numerical experiments purposed by Badalassi *et al.*[4], where the same stretched patterns can be founded. Furthermore fixed the convective scale, the higher is the Peclet number, the slower is the growing process (see Section 5.1.1), hence, for $Pe = 100$, the flow field seems to have the time to change the phase domains shape at the very beginning of the growing process. This results in to the elongated structures that are parallel to the $u$ velocity component shown in Figure 5.13. On the other hand, for $Pe = 10$, the growing process is faster and thus the flow field does not have enough time to modify the domains shape at the very beginning of the process. In fact the structures obtained for lower Peclet numbers show a non zero slope within the flow field direction, at fixed time.

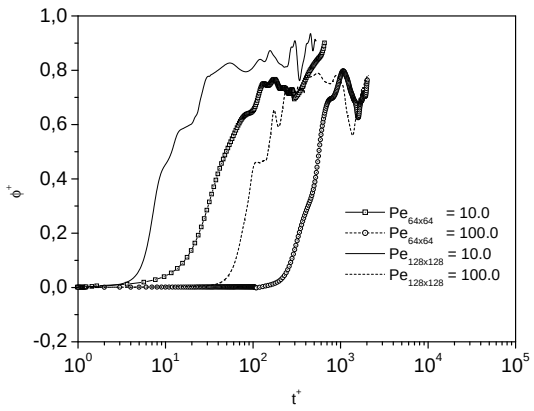


Figure 5.6: Phase separation under shear flow: comparison between the evolution in time of the separation depth for different Peclet numbers and different meshes. $Ch = 0.1$ and $Ca >> 1$.

In Figure 5.6 the comparison between the evolution in time of the separation depth at $Pe = 10$ and $Pe = 100$ for different meshes are reported. The behavior of the growing process seems to be similar to that founded for the pure spinoidal decomposition where the process is driven by the diffusion. Oscillations can be

observed when $s$ has reached its asymptotic value, this is due to the changing of the bulk phase patterns under the effect of the flow field, hence the interface changes rapidly in its shape and also its volume (which is proportional to its length), producing the changing of the separation depth value. Both the simulations obtained with different grid-spacing show the same behavior for long times, whereas at the beginning of the simulation the processes seem to be faster for more refined grids. Increasing the refinement of the mesh the behavior of the process is expected to be closer to the separation depth curve of the $128 \times 128$ mesh, as obtained for the spinoidal decomposition (Figure 5.3.

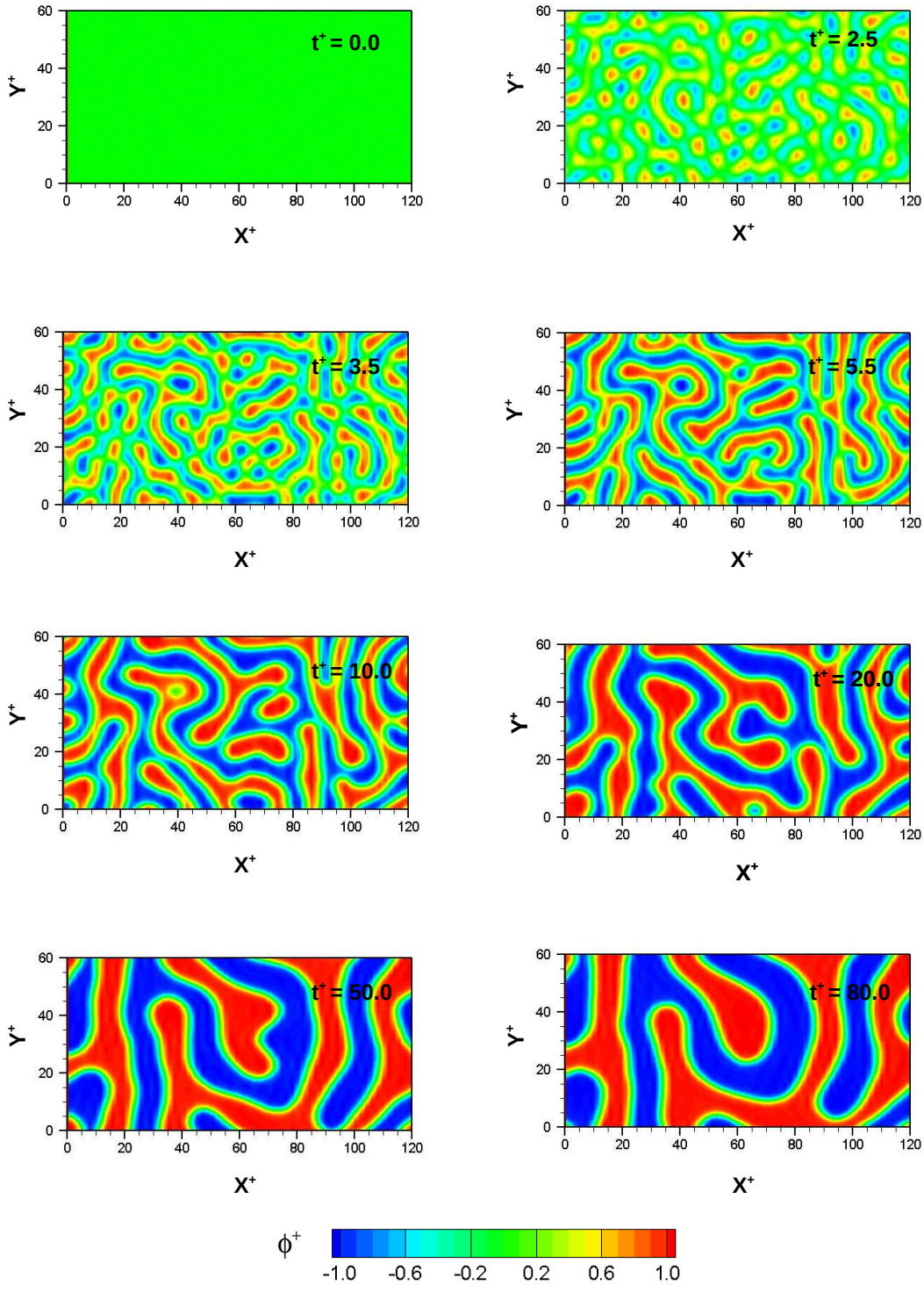


Figure 5.7: Pure diffusive phase separation: Evolution in time of the concentration profiles on the $x-y$ planes at $z^+ = 20$, with $Pe = 1$, $Ch = 0.095$ and $\gamma = 0$. Periodic conditions at the walls, random initial field and $64 \times 64$ mesh.

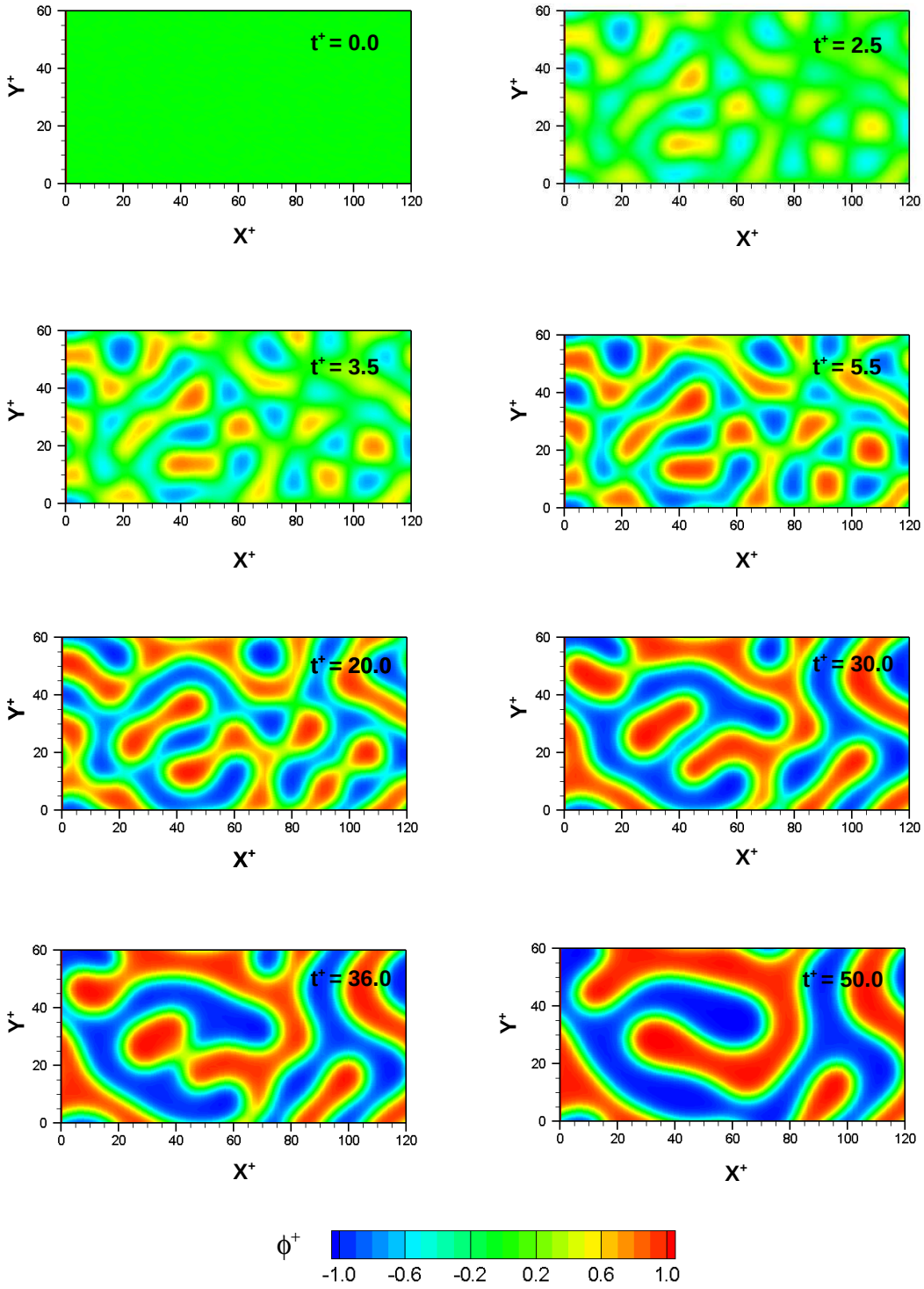


Figure 5.8: Pure diffusive phase separation: Evolution in time of the concentration profiles on the $x-y$ planes at $z^+ = 20$, with $Pe = 1$, $Ch = 0.2$ and $\gamma = 0$. Periodic conditions at the walls, random initial field and $64 \times 64$ mesh.

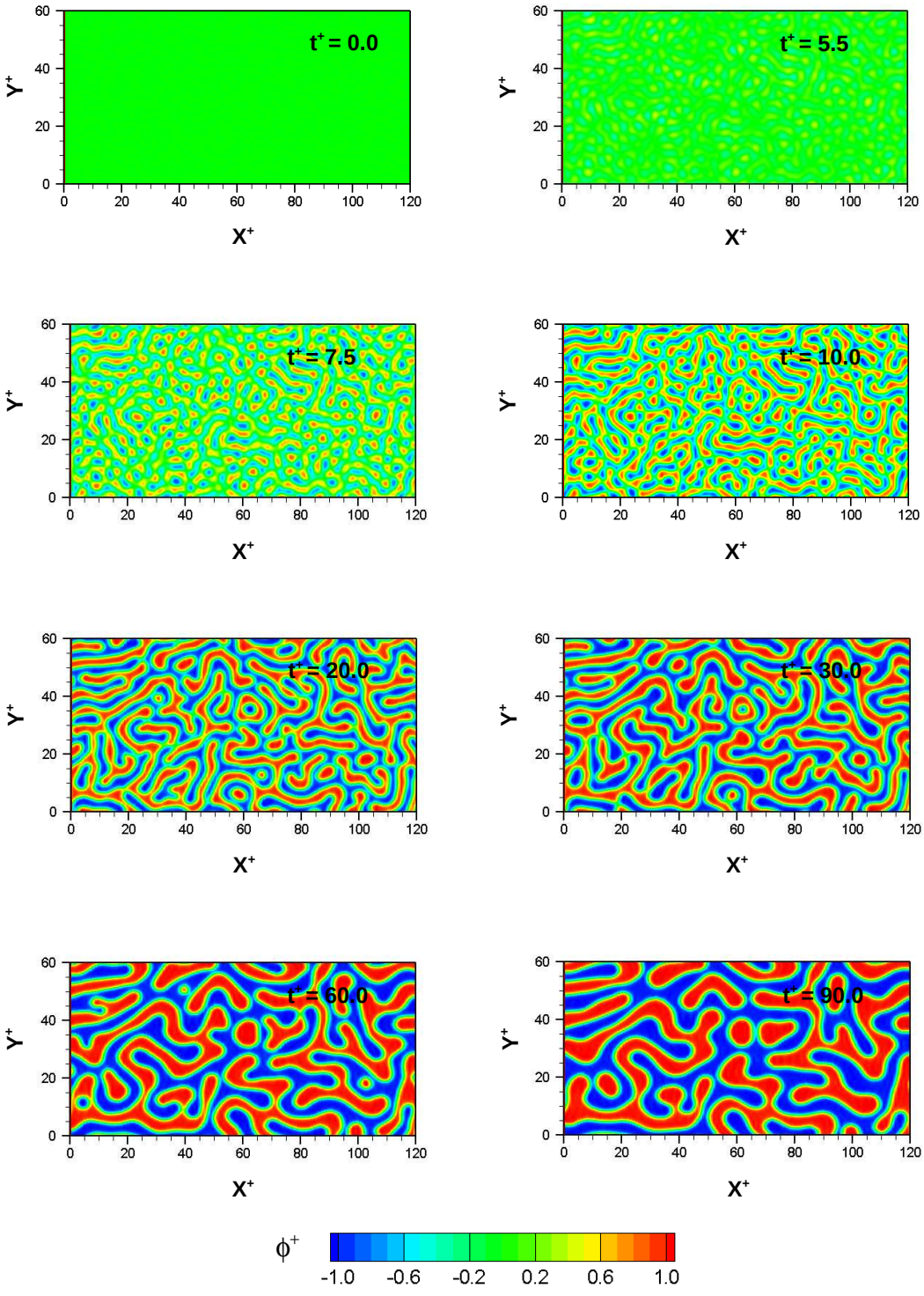


Figure 5.9: Pure diffusive phase separation: Evolution in time of the concentration profiles on the $x-y$ planes at $z^+ = 20$, with $Pe = 1$, $Ch = 0.05$ and $\gamma = 0$. Periodic conditions at the walls, random initial field and $128 \times 128$ mesh.

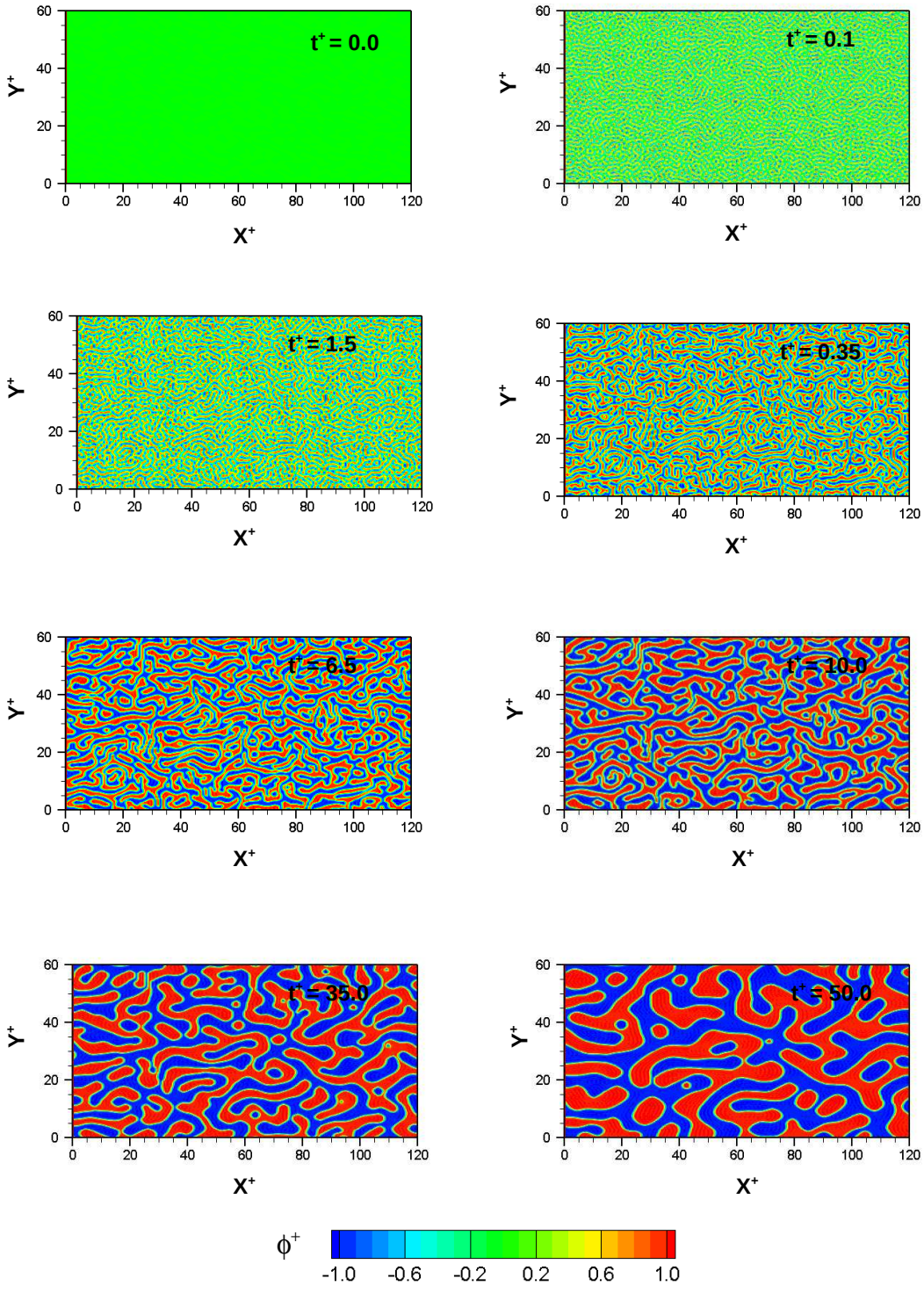


Figure 5.10: Pure diffusive phase separation: Evolution in time of the concentration profiles on the $x-y$ planes at $z^+ = 20$, with $Pe = 1$, $Ch = 0.025$ and $\gamma = 0$. Periodic conditions at the walls, random initial field and $256 \times 256$ mesh.

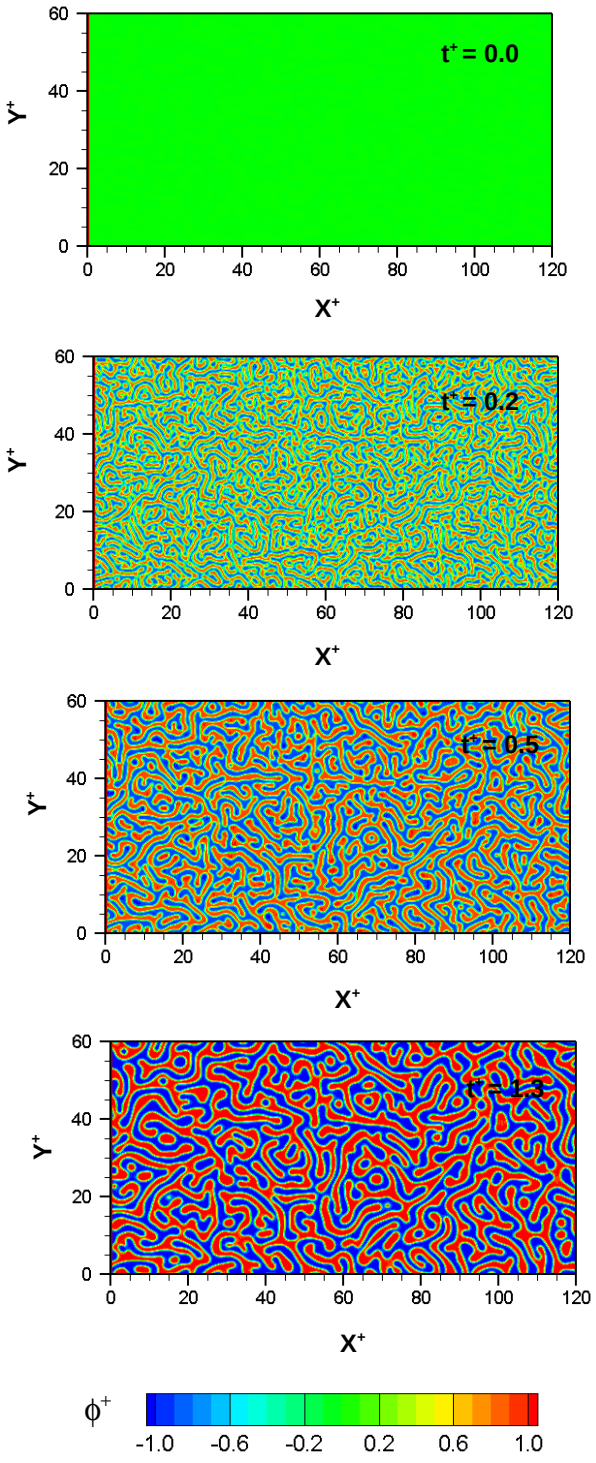


Figure 5.11: Pure diffusive phase separation: Evolution in time of the concentration profiles on the $x-y$ planes at $z^+ = 20$, with $Pe = 1$, $Ch = 0.013$ and $\gamma = 0$. Periodic conditions at the walls, random initial field and $512 \times 512$ mesh.

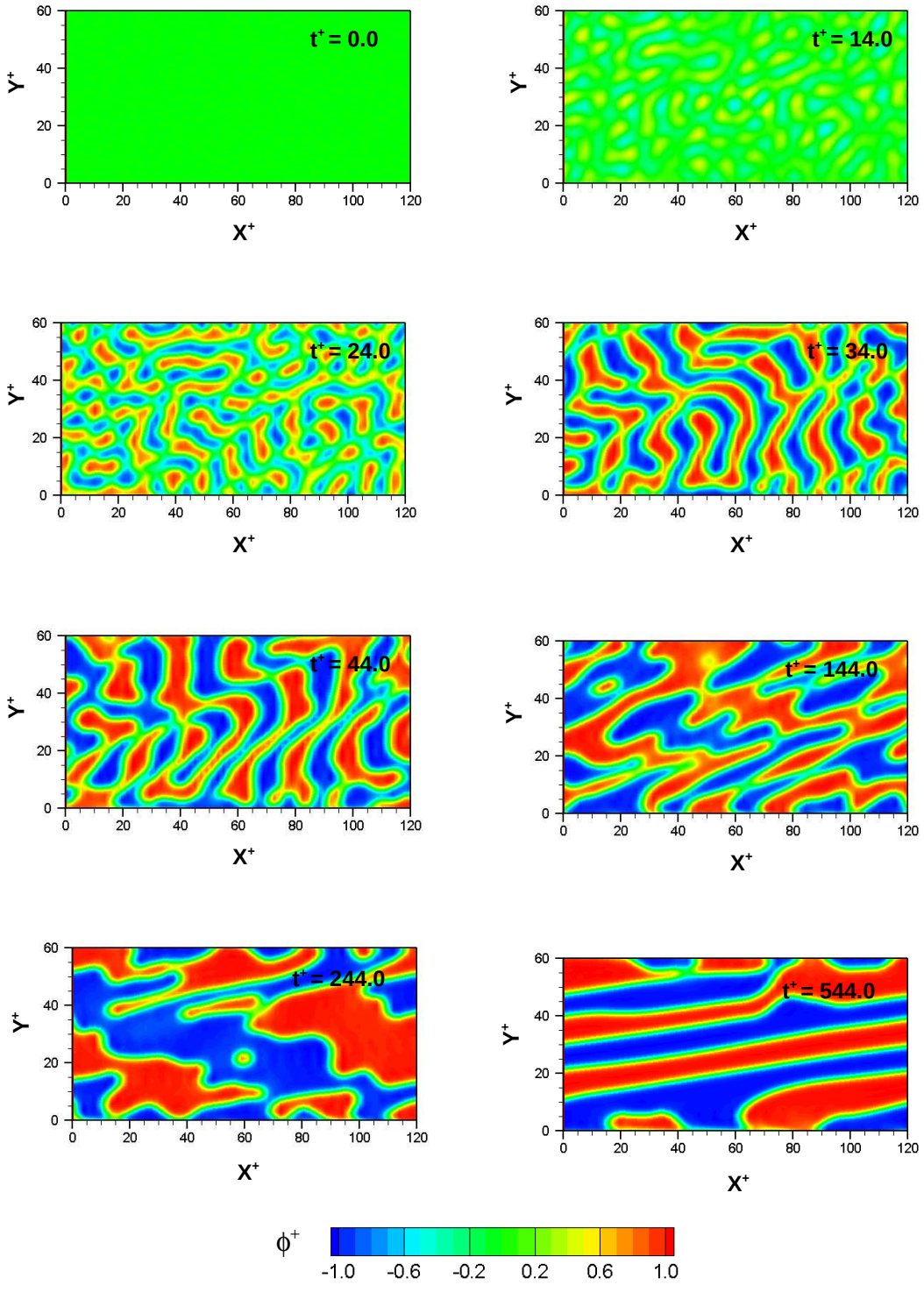


Figure 5.12: Phase separation under shear flow: Evolution in time of the concentration profiles on the $x-y$ planes at $z^+ = 20$, with $Pe = 10$, $Ch = 0.1$, $Ca >> 1$ and $\gamma = 0$. Periodic conditions at the walls, random initial field and $64 \times 64$ mesh.

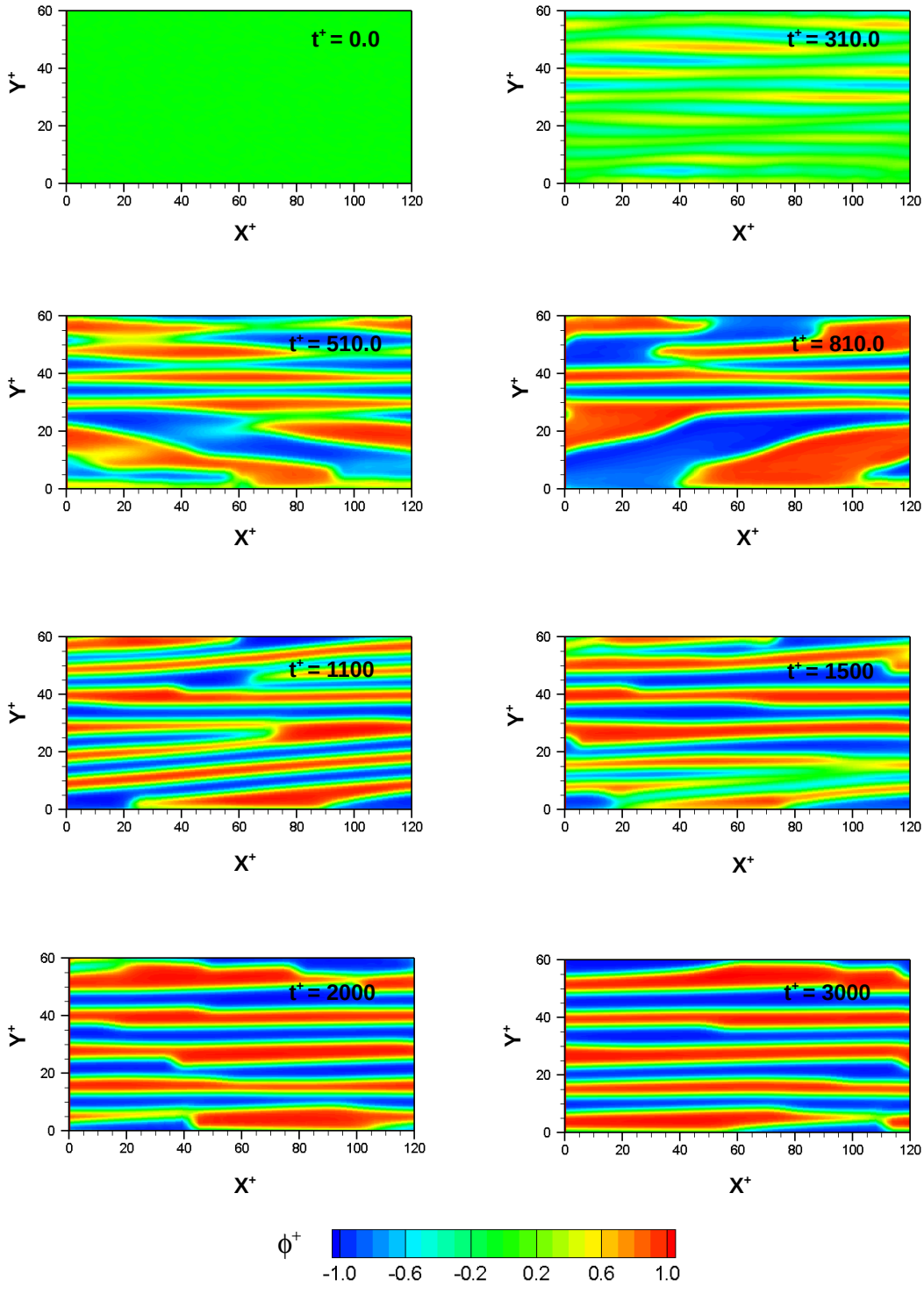


Figure 5.13: Phase separation under shear flow: Evolution in time of the concentration profiles on the $x-y$ planes at $z^+ = 20$, with $Pe = 100$, $Ch = 0.1$, $Ca >> 1$ and $\gamma = 0$. Periodic conditions at the walls, random initial field and $64 \times 64$ mesh.

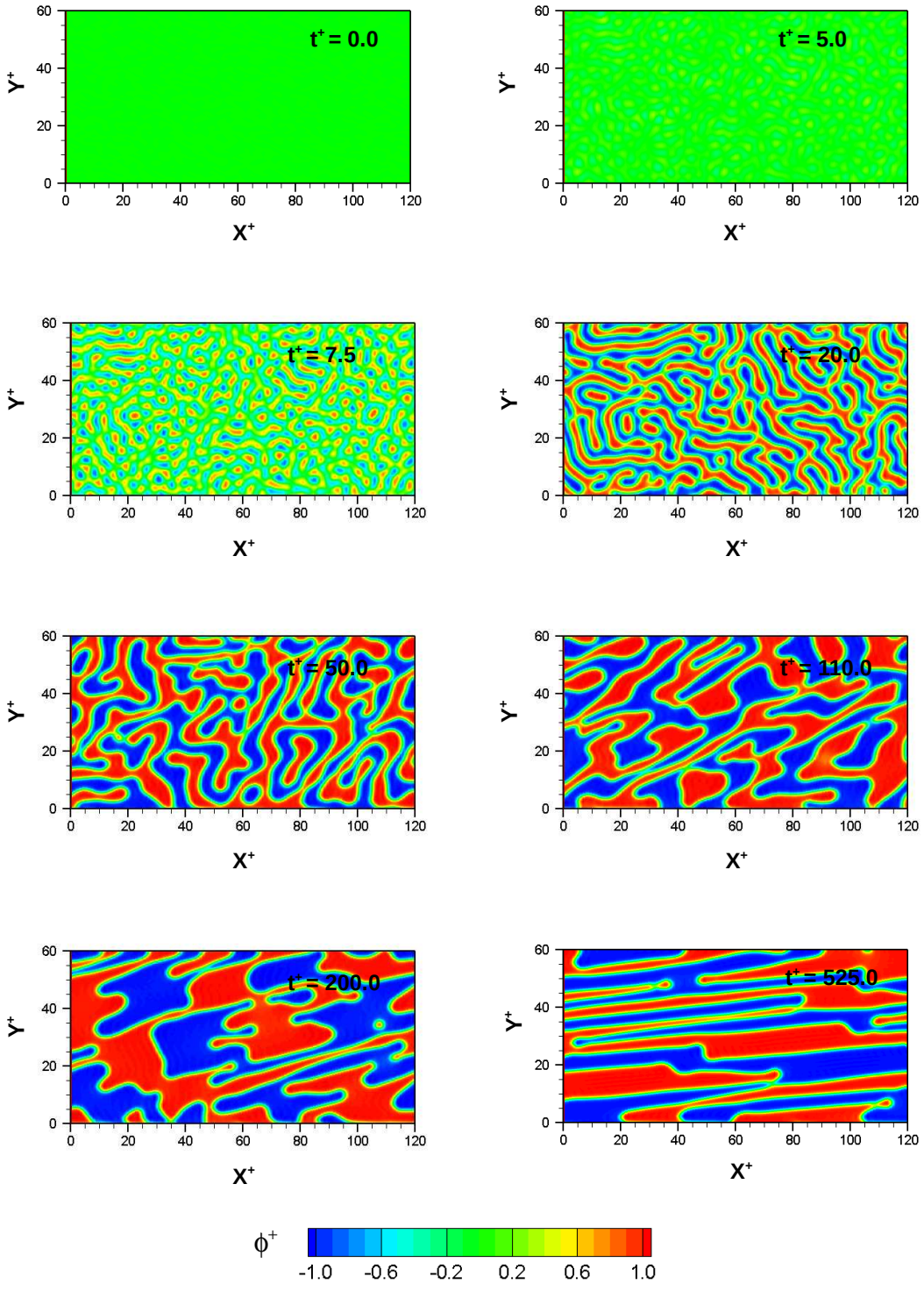


Figure 5.14: Phase separation under shear flow: Evolution in time of the concentration profiles on the $x-y$ planes at $z^+ = 20$, with $Pe = 10$, $Ch = 0.05$, $Ca >> 1$ and $\gamma = 0$. Periodic conditions at the walls, random initial field and $128 \times 128$ mesh.

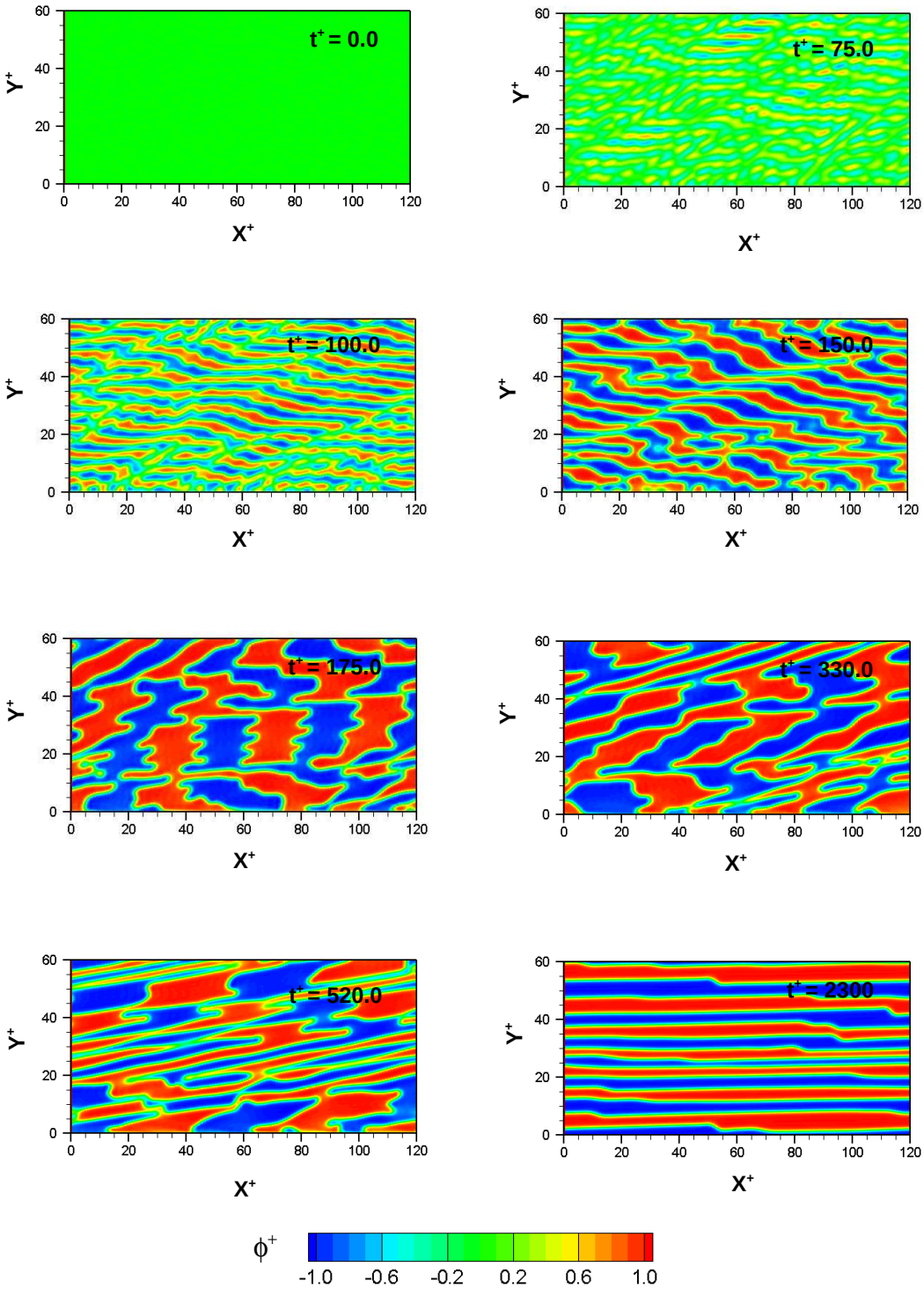


Figure 5.15: Phase separation under shear flow: Evolution in time of the concentration profiles on the $x-y$ planes at $z^+ = 20$, with $Pe = 100$, $Ch = 0.05$, $Ca >> 1$ and $\gamma = 0$. Periodic conditions at the walls, random initial field and $128 \times 128$ mesh.

# Chapter 6

# Conclusion and suggestions for further work

In the present work, the Phase Field Model equation has been implemented in an already existing Direct numerical simulation code. The numerical solution of the phase-separation of polymer blends in a channel geometry have been performed at various characteristic parameters and flow-field conditions. As shown in Chapter 5 the results obtained through this work are in good agreement with the results pointed out by several authors as Lamorgese *et al.*[23], Vladimirova *et al.*[36] and Badalassi *et al.*[4], as in the morphological structures obtained as into the separation depth function $s$. Most of this results have been obtained simulating the pure spinoidal decomposition, whereas the convective phase separation and the phase separation under shear flow, show the need of an investigation for their sensitivity to the Peclet number $Pe$, the Capillary number $Ca$ and the Reynolds number $Re$. The agreement of the results permits to define the following steps to develop the code and to formulate some suggestions for the future work.

## 6.1 Suggestions for further work

First the steps necessary to the correct developing of the code are summarized:

1. Analysis of the convective phase separation dependence on the Capillary

number;

2. simulations with non-constant mobility $\gamma \neq 0$;

3. introduction of a suitable numerical technique for the solution along the wall-normal direction, in order to simulate three-dimensional problems;

4. introduction of the shear flow along the wall-normal direction and deep analysis of the phase separation under shear flow.

At the end some suggestions for the further work are reported. These simulations could be done after the code developments summarized above and are possible thanks to the capabilities of the DNS code, which allows to study more in detail a various types of problems.

- Introduction of a Margules coefficient based thermodynamical chemical potential, in order to allow the code to simulate both mixing and demixing processes;

- introduction of the gravity effects following the scheme purposed by Badalassi *et al.*[5];

- coupling with a temperature field;

- simulation of the phase-separation/mixing in to the turbulent flow regime.

# Bibliography


[1] Anderson D. M., McFadden G. B. & Wheeler A. A. (1998) "Diffuse-interface methods in fluid mechanics", *Annu. Rev. Fluid Mech*, **30**, 139.

[2] Anderson P. D. "Computational rheology multi-component systems", *Multi-phase microfluidics - The diffuse interface model*, CISM, Udine, Italy, 15-19 June 2009.

[3] Ascher U. M., Ruuth S. J. & wetton T. R. (1995) "Implicit-explicit methods for time dependent partial differential equations", *SIAM J.Numer. Anal.*, **32**, 797.

[4] Baldalassi V. E., Ceniceros H. D. & Banajee S. (2003) "Computation of multiphase systems with phase field models", *Journal of Computational Physics*, **190**, 371-973.

[5] Baldalassi V. E., Ceniceros H. D. & Banajee S. (2004) "Gravitional effects on structure development in quenched complex fluids", *Ann. N.Y. Acad. Sci.*, **1027**, 371-382.

[6] Boyd j. P. (2000) "Chebyshev and Fourier spectral methods", Dover Publications, New York.

[7] Cahn J. W. & Hilliard J. E. (1958) "Free energy of a nonuniform sys- tem. I. Interfacial free energy", *The Journal of Chemical Physics*, **28**, 258.

[8] Canuto C., Quarteroni A., Hussaini M. Y. & Zang T. A. (2006) "Spectral methods: Fundamentals in single domains", Springer

[9] Christov C. I., Pontes J., Walgraef D. Velarde M. G. (1997) "Implicit time spliting for fourth-order paraolic equations", *Comput. Methods Appl. Mech. Engrgr*, **148**, 209-224.

[10] Comini G. (2004) "Fondamenti di termodinamica applicata", Sge editoriali, Padova.

[11] Davis H. T., & Scriven L. E. (1982) "Stress and structure in fuid inter- faces", *Adv. Chem. Phys.*, **49**, 357.

[12] DeGennes P. G. (1980). "Dynamics of fluctuations and spinodal decom- position in polymer blends", *J. Chem. Phys.*, **72**, 4756.

[13] Emmerich H. (2003) "The diffuse interface approach in material science - Thermodynamic concepts and applications of phase-field models", Springer.

[14] Fermi E. (1958) "Termodinamica", Bollati Boringhieri, Torino.

[15] Hohenberg, P.C. & Halperin, B.I. (1977) "Theory of dynamic critical phenomena", *Review of Modern Physics*, **49**, 435.

[16] Jancskar I., Sari Z., Szakonyi L. & Ivanyi A. (2008) "Diffuse interface modeling of liquid-vapor phase transition with hysteresis", *Physica B.*, **403**, 505-508.

[17] Kawasaki, K. (1970) "Kinetic equations and time correlation functions of critical fluctuations", *Annals of Physics*, **61**, 1.

[18] Keestra B. J. "Capillary and low inertia spreading of a microdroplet on a solid surface", *Phd Thesis.*, Technische Universiteit Eindhoven.

[19] Khatavkar V. V. "Capillary and low inertia spreading of a microdroplet on a solid surface", *Phd Thesis.*, Technische Universiteit Eindhoven.

[20] Khatavkar V. V., Anderson P. D. & Meijer H. E. H. (2006) "On scaling of diffuse-interface models", *Chem. Eng. Science*, **61**, 2364-2378.

[21] Kim J., Moin P. & Moser R. (1987) "Turbulence statistics in fully developed channel flow at low Reynolds numbers", *J. of Fluid Mechanics*, **177**, 133-166.

[22] Korteweg, D.J. (1901) "Sur la forme que prennent les equations du mouvement des fuides si l'ont tient compte des forces capillaires causes par des variations de densite considerables mais continues et sur la theorie de la capillarite dans l'hypothese d'une variation continue de la densite", *Archive Nűeerlandţese des Sciences Exactes de la Nature. Serie II.*, **6**, 1.

[23] Lamorgese A. G. & Mauri R. (2008) "Diffuse-interface modelling of phase segregation in liquid mixtures", *Int. Journal of Multiphase Flow*, **34**, 987-995.

[24] Lamorgese A. G. & Mauri R. (2006) "Mixing of macroscopically quiescent mixtures", *Physics of Fluids*, **18**, 044107.

[25] Lowengrub J. "Modelling and simulation of multicomponent fluid flows", *Multiphase microfluidics - The diffuse interface model*, CISM, Udine, Italy, 15-19 June 2009.

[26] Lowengrub J. & Truskinovsky L. (1997) "Quasi-incompressible Cahn-Hilliard fluids and topological transitions", *Proceedings of the Royal Society*, London, Serie A, **454**, 2617.

[27] Mauri R. (2005) "Elementi di fenomeni di trasporto", Edizioni Plus, Pisa.

[28] Molin D. "Mixing and Phase Separation of Fluid Mixtures", *Phd Thesis.*, Università degli Studi di Pisa

[29] Pismen L.M. (2001) "Nonlocal diffuse interface theory of thin films and moving contact line", *Physical Review E*, **64**, 021603.

[30] Pope S. B. (2000) "Turbulent flows", Cambridge unniversity press, Cambridge.

[31] Lord Rayleigh (1892) "On the theory of surface forces - Compressible fuids", *Philosophical Magazine*, **33**, 209.

[32] Saylor D. M., Kim C., Patwardhan D. V. & Warren J. A. (2007) "Diffuse-interface theory for structure formation and release behavior in controlled drug release systems", *Acta Biomaterialia*, **3**, 851-864.

[33] Siggia, E.D. (1979) 'Late stages of spinodal decomposition in binary mixtures", *Physical Review A*, **20**, 595.

[34] Soldati A. & Andreussi P. (1996) "Fluidodinamica di processo", Forum, Udine.

[35] Van der Waals (1893). "The thermodynamic theory of capillarity under the hypothesis of a continuous variation of density", *Journal of Statistical Physics* , **20**, 200, J.S. Rowlinson, English transl

[36] Vladimirova N., Malagoli A. & Mauri R. (1999) "Two-dimensional model of phase segregation in liquid binary mixtures", *physical review E*, **60**, 6968-6977.

[37] Wise S. M., Lowengrub J. S., Frieboes H. B. & Cristini V. (2008) "Three-dimensional multispecies nonlinear tumor growth - I. Model and numerical method", *J. Theoretical Biology.*, **253**, 524-543.

[38] Young D. L., Tsai C. C., Murugesan K., Fan C. M. & Chen C. W. (2004) "Time-dependent fundamental solutions for homogeneus diffusion problems", *Engineering analysis with boundary elements*, **28**, 1463-1473.

[39] Yue P., Feng J. J., Liu C. & Shen J. (2004) "A diffuse-interface method for simulating two-phase flows of complex fluids", *Journal of Fluid Mechanics*, **515**, 293-317.

# Appendix

# Appendix A

# Temporal discretization schemes

The numerical discretization schemes tested in to the Section 4.2.2 are following reported.

## A.1 Third order order Adams-Bashfort - Crank-Nicolson (CN-AB3)

The third order Adams-Bashfort method is used to compute explicitly the non linear terms, whereas the Crank-Nicolson scheme is used for the linear terms:

$$\frac{\phi^{n+1}-\phi^{n}}{\Delta t}=\frac{1}{12}\left(23S_c^{n}-16S_c^{n-1}+5S_c^{n-2}\right)+\frac{1}{2}\left(\psi_c^{n+1}+\psi_c^{n}\right) \tag{A.1}$$

## A.2 Backward Euler - Crank-Nicolson (CN-E)

The backward Euler method is used to compute explicitly the non linear terms, whereas the Crank-Nicolson scheme is used for the linear terms:

$$\frac{\phi^{n+1}-\phi^{n}}{\Delta t}=\left(S_c^{n}\right)+\frac{1}{2}\left(\psi_c^{n+1}+\psi_c^{n}\right) \tag{A.2}$$

## A.3 Second order Runge-Kutta - Crank-Nicolson (CN-RK2)

The second order Runge-Kutta method is used to compute explicitly the non linear terms, whereas the Crank-Nicolson scheme is used for the linear terms:

$$\frac{\phi^{n+1}-\phi^n}{\Delta t} = \frac{1}{2}\left[S_c(\phi^n, t^n) + S_c(\phi^{n+\frac{1}{2}}, t^{n+\frac{1}{2}})\right] + \frac{1}{2}\left(\psi_c^{n+1} + \psi_c^n\right) \tag{A.3}$$

Where the fractional step is calculated using the forward Euler formula:

$$\phi^{n+\frac{1}{2}} = \frac{1}{2}\left[\phi^n + \Delta t S_c(\phi^n, t^n)\right] \tag{A.4}$$

## A.4 Second order backward difference scheme (SBDF)

$$\frac{\phi^{n+1} - \frac{4}{3}\phi^n + \frac{1}{3}\phi^{n-1}}{\Delta t} = \frac{2}{3}\left(S_c^n - S_c^{n-1}\right) + \frac{2}{3}\psi_c^{n+1} \tag{A.5}$$